Airbag System for Hip-fracture Protection due to Falls – Mechanical system design and development

by

Chan Cheung Shing

A Thesis Submitted in Partial fulfillment
of the Requirement for the Degree of
Master of Philosophy
in
Department of Orthopaedics and Traumatology

Airbag System for Hip-fracture Protection due to Falls – Mechanical System Design and Development

Thesis/Assessment Committee

Professor Qin Ling (Chairman)

Professor Leung Kwok Sui (Thesis Supervisor)

Professor Li Wen Jung (Thesis Co-Supervisor)

Professor Meng Qing Hu (Committee Member)

Professor Chow Hung Kay (External Examiner)

Airbag System for Hip-fracture Protection due to Falls – Mechanical System Design and Development

submitted by

Chan Cheung Shing

for the degree of Master of Philosophy
at The Chinese University of Hong Kong

Abstract

Hip Fracture is a common fall-related fracture among the elderly. This fracture may cause the reduction of mobility or even mortality in the elderly. There are many commercially available hip protectors which are composed of a pair of hard pads and worn with a tight undergarment. However, the elderly feel uncomfortable and inconvenient to wear the protectors, leading to a poor compliance rate without achieving an expected prevention of hip fractures. This brings out the idea of developing a hip protecting system which is easy to wear and yet prevent fractures when fall. It is also the objective of this study.

The hip protecting system targeted to protect the elderly of a mean weight 51kg. Moreover, only lateral fall which causes a higher risk of hip fracture compared to forward and backward falls is considered. To predict the peak femoral impact force, a falling elderly of 51kg is modeled as a standard linear solid support model. The stiffness and the damping coefficient are set to be 71kN/m and 561N-s/m respectively for without any protection device. The hypothesis of the study is that the peak femoral impact force can be attenuated to below the hip-fracture threshold: 3100±1200N by reducing the stiffness and increasing the damping coefficient.

To build the protecting system, the idea of airbag restraining systems of automobiles is applied. The system has two modules – a sensing module (μIMU) and an inflator which connects to two nylon airbags. When the μIMU detects a fall, it will trigger the inflator which deploys the airbags within 0.5s to protect the elderly. The gas is supplied from a handy compressed gas cylinder but not the combustion of chemicals. Mathematical model is adopted to find the set of design parameters of the inflator – the pressure and the mass of gas in the compressed gas cylinder, the cross-sectional area of orifice and the length of the connecting pipes – to give the required inflation time and airbag pressure.

Moreover, an inverted pendulum is designed to find the pressure and size of airbag required. Finally, to justify the feasibility of such hip protector, the inflator and the sensing module are connected and attached to a human who mimics the lateral falling motion of an elderly.

Keywords: Airbag system, hip protection, μIMU

防止髖關節因跌倒而折斷的安全氣袋裝置

－ 機械設計及開發

陳章成

香港中文大學
矯形外科及創傷學系
哲學碩士論文

2007年5月

摘要

髖關節骨折是一種由跌倒引致的骨折，經常發生在老人家身上。這種骨折可以降低老人的活動能力，甚至導致老人死亡。市面上有很多髖關節保護器，是將一對硬墊覆蓋髖關節，並且放在緊身褲內。可是大部份老人家都覺得穿戴保護器會不舒適，而且不便穿戴，導致穿戴率低，未能達到預期的效果。這個問題引伸出一個新的構思：發展一個方便穿戴，而同時能夠有效防止骨折的髖關節保護器。這個構思亦是本課題的目的。

在發展初期，新的髖關節保護器是針對平均體重約五十一公斤的老人家，而且專門應付側向跌倒－比起向前及向後跌倒有更高的髖關節骨折的風險。爲了預測股骨的最大撞擊力，standard linear solid support模型會用來代表一個五十一公斤的老人，它的硬度及阻尼系數分別被設定爲 71kN/m及 561N-s/m。透過降低硬度及增加阻尼系數，股骨的最大撞擊力就可以減少至髖關節骨折的所需程度(3100±1200N)以下。

汽車的安全氣袋的原理被應用於製造這個保護器。保護器有兩個組件—一個微型慣性測量單元(μIMU)和一個充氣儀器。當μIMU探測老人跌倒，它便會觸發充氣儀器，接著充氣儀器會在0.5 秒內展開氣袋保護老人。而氣體是由一支輕巧的高壓汽缸供應，並不是化學物品的燃燒。數學模型被採用來找出一套設計參數，令充氣儀器能提供所需的充氣時間和氣袋的氣壓。

另外，爲了證實所需要的氣壓及氣袋大小，我們設計了一個**倒轉的**擺錘。最後，爲了證明新的保護器的可行性，充氣儀器及 μIMU 連接一起並安裝在一個人的身上，而這個人會模仿老人的側向跌倒動作。

Acknowledgements

I would like to express my first and foremost gratitude to my supervisor Professor Kwok-sui Leung and co-supervisor Professor Wen Jung Li, for their guidance in the past two years. Professor Leung gives me a lot encouragement and support in my research work. Though he is a doctor without any engineering background, he always encourages me to do more analyses and make the study more theoretical, more than mechanical design. This allows me to explore to more useful knowledge in engineering field. Professor Li is an engineer and he provides me guidance and suggestion in mechanical design.

I would like to thank to Professor Wing-Hoi Cheung Louis who is my director of study. He gives me idea of biomechanical test and arranges my study schedule.

I also want to say thank you to my partner Mr Shi Guangyi and Mr Tony To. Mr Shi is responsible for the sensor and fall detection algorithm. I have learnt to work as an engineer while working with him in the demonstration of airbag system. Tony gave me idea in mechanical design and helped doing test for prototype. Without his help, the prototype may not be finished on time.

I also am grateful to my colleagues in MAE Department, Mr Chung Chor Fung, Dr Zhang Guang Lie, Mr Chow Chun Tak, Miss Mandy Sin, Miss Kwok Sze Yin, Mr Tsang Chi Chiu, Mr Dong Zhu Xin, Mr Luo Yilun, Miss Heidi Wong, Miss Chow Wing Yin, Mr Allan Mok and Mr Phillip Lee, for their support to my research and bring me a comfortable working atmosphere.

Lastly, I have to thank my colleagues in ORT Department, Mr Patrick Tsang, Miss Debbie Ho, Mr Patrick Sze, Mr Eric Ng, Mr Tam Kam-fai and Mr Daniel Fong, for their help in the arrangement of my study schedule and support in my research.

Table of Contents

List of Figures

List of Tables

Abbreviations and Notations

A_a: the circular area of the airbag (in m^2)

A_{23}: the area of the outlet orifice of airbag (in m^2)

c: damping coefficient (Ns/m)

g: gravitational acceleration = $9.81 m/s^2$

h: the initial thickness of the airbag (in m)

k: spring constant (N/m)

K_{23}: the dimensionless derivative of N_{23}

N_{23}: a ratio of mass flow rate to choked mass flow rate

n: $n = 1$ for isothermal condition and $n = \gamma$ for adiabatic condition

P_1: the upstream pressure of orifice (in Pa)

P_2: the downstream pressure of orifice (in Pa)

P_3: the atmospheric pressure (in Pa)

R: gas constant ($R = 287$ j/kgK for air, 188.9j/kgK for CO_2)

T_2: the downstream temperature of orifice (in K)

V_2: the volume of airbag or chamber (in m^3)

W: mass flow rate (kg/s)

W_{cr}: mass flow rate under sonic flow (kg/s)

γ: the specific heat ratio ($\gamma = 1.4$ for air, 1.3 for CO_2)

Chapter 1

Introduction

1.1 Background and Objective

Definition of Hip Fracture

"A hip fracture is a break near the top of the femur. The break is usually detected at the femoral neck or intertrochanteric region of hip joint. Hip fractures occur when the elderly people falls sideways and onto the hip, side of leg, or buttocks. Falling backward reduces the risk of hip fracture." [1] Elderly people suffer most from this health problem and female are more likely to suffer hip fracture [4]. For both gender, about 56% hip fractures occurred at femoral neck while the remaining occurred at trochanter [4].

The sideways falls are the major cause of hip fractures among the other falls [2]. There are several factors which increase the risk of hip fracture such as low bone mineral density, insufficient passive energy absorption of soft tissues around the greater trochanter and disable to take protective responses while falling. [1]. The causes of hip fracture during a fall can be summarized in sequence as [4]: first elderly cannot have a protective response such as breaking fall with arms; second the impact location is closed to the hip; third the soft tissue over the greater trochanter cannot give sufficient energy absorption during impact; lastly the femoral impact force exceeds the proximal hip fracture threshold.

Loss due to Hip Fractures

Hip fractures account for most of the deaths and costs of all the fall-induced fractures. In worldwide, there are 4,000,000 hip fracture cases per year and the mortality rate is 30.8% in one year. In Hong Kong, there are 4,000 cases per year [3]. This leads to HK$150 million medical and rehabilitation expenditure.

In Canada, 49% of elderly who fall suffer fractures and 19% of the fractures are hip fractures. Though hip fracture is the third most common type of fall-induced injury, it causes the greatest number of death and the severe complications. The annual expenditure spent on hip fracture treatment is $650 million [4].

Besides a high mortality rate, hip fractures also make elderly lose independence. 24 to 40% of elderly suffered hip fractures require nursing home care. One year after hip fracture, 40% cannot walk independently; 50% need assisting device for walking; and 60% even need help in daily activities such as bathing and dressing [4].

Commercial Available Hip Protectors

There are many commercially available hip protectors which are composed of a pair of pads covering the hips and worn with a tight undergarment or attached externally by belts. They are used to attenuate the impact force enter to the hip joint and hence reduce the risk of hip fracture. They can protect elderly from direct impacts to their hips but not rotational injuries and impacts to other locations besides the hips [11]. Moreover, they cannot prevent elderly from falling.

They use two mechanisms (either one or both): energy shunting and energy absorbing. Energy shunting diverts the impact force to the tissue surrounding the femoral neck while energy absorbing uses the protector itself to absorb the impact force [1]. An example of energy shunting protectors is KPH1 protector. It has a size of 19cm long and maximum 9cm width. The outer shield is a semi-flexible material for energy shunting and the inner part is energy-absorbing material. It has a convex shape to leave a safety margin (2.0-2.5cm) from the greater trochanter. The safety margin prevents the contact between trochanter and the protector during impact [11]. This is a key feature different from the energy absorbing protectors. An example for energy absorbing protectors is *Safetypants*. Its size is 18cm long and maximum 16cm width. It consists of 20mm thick low density foam to absorb the impact energy. It hasn't any safety margin between the greater trochanter and the protector [11]. From the pendulum impact test conducted by P. Kannus in 1999 [11], the energy shunting protectors has a higher force attenuation capability than energy absorbing protectors. Under high impact force of 10,840N, KPH1 and *Safetypants* could reduce the femoral impact force to 1360N and 5770N respectively. Therefore, energy shunting mechanism has a better force attenuation capability which is as high as 87%. However, if they are not worn in proper location, their protecting capabilities will drop. Unfortunately, the high-risk users have difficulties to wear the hip protectors correctly [12].

Effectiveness of Current Protectors

A study reported that the protectors reduced hip fracture incidence by 53% [7]. Another study from Daniel K. Chan et al, 2000 [8] also showed that hip protectors could significantly reduce hip fracture cases. 71 nursing home residents participated in the 9-month study, 40 worn hip protectors (treatment group) and 31 were in the control group. The outcome was that 1 fracture occurred per every 16.8 falls in the treatment group, and 1 fracture occurred per every 63.7 falls in the control group. Other figure from Jantti et al., 1998 [9] also shown that the hip fracture occurrence per falls was lower in treatment group (1/36) compared with control group (7/36). Therefore, it is statistically true that the hip protectors can effectively reduce hip fractures.

Compliance Rate of Current Protectors

Despite of the proven effectiveness of hip protectors, the compliance rate is low recently. In Hong Kong, hot weather brings a low compliance rate of hip protectors: about 40% annually, dropping from 70% in autumn to 20% in summer [3]. Besides heat wave, the elderly also feel uncomfortable to wear the hip protectors. The visibility of the hip protector from outside also leads to shorter wearing time.

The compliance rate is not much better in foreign countries. Several researches related to compliance rate had been conducted. For example, Peter D. O' Halloran et al., 2004 [5] studied the effects of hip protector type and resident characteristics on compliance rate in Northern Ireland. At the beginning, there were 109 elderly (aged from 61 to 98) from residential homes and nursing homes wearing hip protectors. Two types of protectors, Safehip (an energy shunting type) and HipSaver (an energy absorbing type), were distributed evenly to these elderly. 43% (47/109) were still using the hip protectors at 12 weeks and there was no significant difference in percentage use at 12 weeks between the compliance rate of Safehip and HipSaver. Peter D. O' Halloran concluded that the protector type didn't affect the continuous use of protectors, and the residents who had a history of a fall and/or are physically and mentally disable were more likely to wear hip protectors.

More importantly, Halloran et al. [5] also concluded that the nursing home staff's help was also a critical factor on the compliance rate of nursing home residents as those residents were highly dependent. From the study of Jeffrey B. et al, 2003 [6], the acceptance of protectors among high risk group and staff was more obviously an importance factor on the compliance rate among the high risk groups. 56 long-term care residents from an elderly home (in Central Massachusetts) who belonged to high risk group participated in the study. In the 13-month study, the compliance rate maintained as 90%-95% after the first month of study. Heat wave didn't appear to reduce the compliance rate as like in Hong Kong. This might be because the elderly most likely stayed indoor. However, the compliance rate in community is still low.

Rising Need of Hip Protectors

The aging population is growing in Hong Kong and China. According to the International Institute for Applied Systems Analysis, there will be more than 1 billion elderly (>60 year-old) in China in 2015. While in Hong Kong, U.S. Census Bureau predicted the population of age group > 60 will increase from 14.57% in 2005 to 32.84% in 2030. Thus, the need of hip protectors is rising.

Hypothesis

As current hip protectors are proven able to reduce hip fractures but have low compliance rate, this research project has been conducted to develop a new generation of hip protector. This new protector is more convenient and comfortable to wear, leading to a higher compliance rate. Meanwhile, the protecting ability may be improved but not weakened. The new protector is designed to use airbags for protection. The airbags will be proven able to protect the elderly from hip fracture due to fall.

1.2 Contribution

The study analyzes the feasibility for using human airbag system to protect an elderly from hip fracture. A simple electrically triggered inflator was built to demonstrate that a portable airbag system deploy an airbag to protect a falling human. Simple mathematical models are used to predict two important issues: the airbag size and pressure required attenuating the impact force; requirement of the inflator to give the required airbag pressure and inflation time.

1.3 Thesis Outline

The remaining chapters of the dissertation are organized as follow: In Chapter 2, the architecture of the whole system is introduced. Chapter 3 presents the structure, mechanism and performance of the inflator. Chapter 4 describes the mathematical model to calculate the inflation time and airbag pressure. Chapter 5 describes the mathematical model to predict the femoral impact force. The estimation of requirement of airbag pressure and size are also presented in this chapter. Chapter 6 presents the suggested impact test to find the required airbag pressure and size, which is the future work. Finally, Chapter 7 presents the conclusion and proposed future improvements.

Chapter 2
System Architecture

2.1 Conceptual Design

The airbag hip protector is divided into two modules: a sensing device and a mechanical part which aims for deploying the airbags (see Figure 2-1). The mechanical part can be further divided into three modules: an inflator, a pressurized cylinder and two airbags. The pressurized cylinder used contains CO_2. The sensing device consists of a μIMU and a fall detection algorithm.

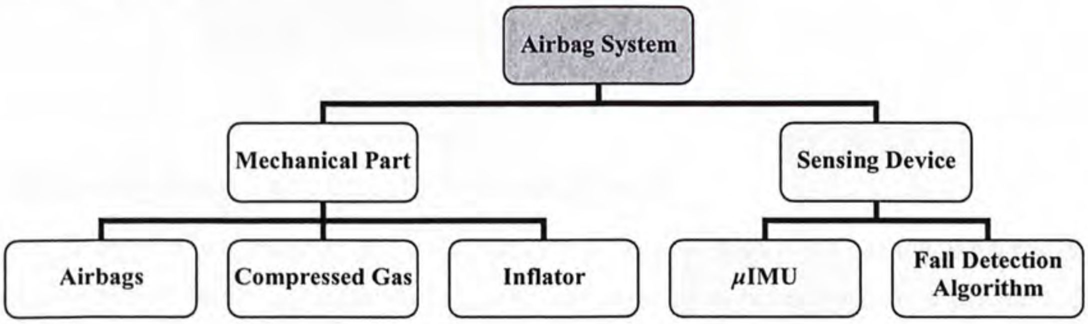

Figure 2-1) The architecture of the airbag system

Figure 2-2 shows the conceptual design of the airbag hip protector. The belt pocket shape will be looked more natural on the elderly. Moreover, the design does not require any undergarments. Thus, problems such as feeling hot and inconvenience to put off won't be found on this design.

Initially, the airbags are folded in a belt. When an elderly loses balance, the MEMS micro sensors in the belt will detect his/her disorientation and triggers the inflation of the airbags on both sides simultaneously in a few hundred milli-seconds before falling to the ground. The hip-airbags can be designed just like automobile airbags, which contain many micron-size holes for automatic deflation.

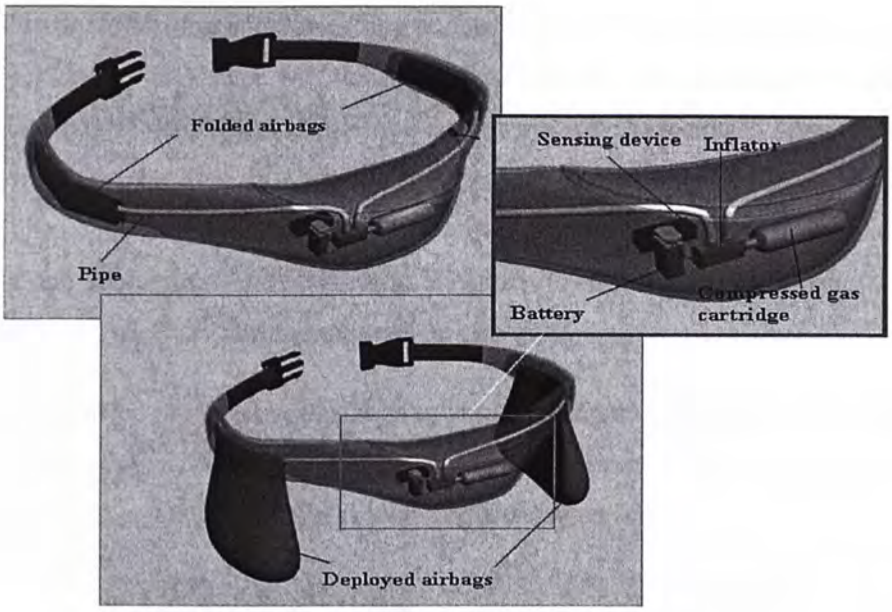

Figure 2-2) Conceptual illustration of the airbag hip protector

2.2 Sensing Device and Fall-Detection Algorithm

Since lateral falling leads to most hip fracture compared with other falling postures, the research project focus on lateral falling. The sensing device is designed to distinguish the lateral falling and other non-falling actions.

The sensing device (also called Micro Inertial Measurement Unit or μIMU in short) consists of three MEMS accelerometers (ADXL203 from Analog Devices Inc.) and three MEMS gyroscopes (muRata ENC-03 from muRata Inc.) and one Bluetooth module (v2.0 SMD Module from Sparkfun Company) (see Figure 2-3). The Bluetooth allows a wireless transmission of motion data to computer. The microcontroller used is ATMEL ATmega32. The sampling rate of the microcontroller is 200Hz which is enough for measuring human motions. The sensing module in the final system will also adopt this sampling rate. The overall size is 66mm x 20mm x 20mm. It can track the 3D motions and orientations in real time. The μIMU together with the Bluetooth can be powered by two Lithium batteries of 3.6V for 3 hours [13].

The classification of falling and non-falling actions is a binary pattern recognition. A Support Vector Machines (SVM) filter was constructed to classify these actions. To construct the filter, motion data of falling and non-falling actions were first collected. Then SVM training is used to produce the filter in a computer [13]. The motion data collected including 100 lateral fallings and 100 other non-fallings motions including walking, running, sitting, walking up and down stairs and walking in elevators. The SVM filter obtained succeeds to classify the falling and non-falling motions into two groups.

Regarding an aborted fall (the user manage to hold on something during falling), it is treated as a non-falling motion. The SVM filter will add the training data of this kind of motion. Eventually, the airbags won't be triggered during an aborted fall.

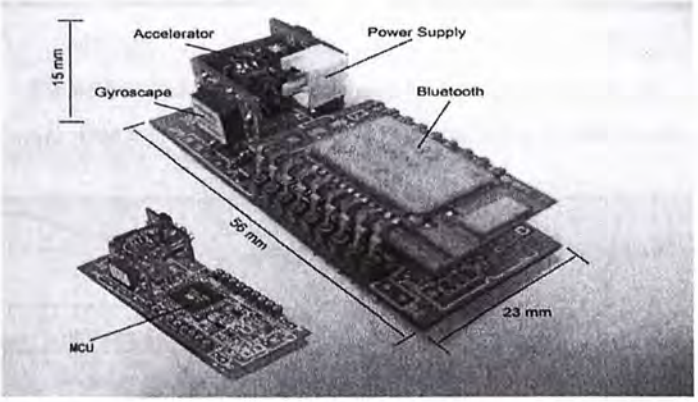

Figure 2-3) The Micro Inertial Measurement Unit

In order to analyze the μIMU signal output, a high speed camera was used to record the falling motion of a dummy of 45kg while the μIMU was also operating. The model of the camera is PCO 1200hs High Speed Cam with a maximum resolution of 1280 x 1025 pixels. The film rate used was 200Hz. The camera was placed 5m away and orthogonal to the falling direction. Two measurements were taken. Figure 2-4 shows the falling motions captured by the high speed camera. By measuring the inclined angle of the trunk (θ_i) in the films between known time intervals, the change of inclined angle with respect to time can be obtained. The angle-time relationship can be fitted with a cubic curve. The instantaneous angular velocity of the hip can be measured by differentiating this cubic curve. Figure 2-5(a) shows the angle-time relationship can be fitted with a cubic curve. Moreover, when compared to one of the gyro output (the rotational velocity of trunk) of the μIMU, the signal corresponding to impact can be justified. This also helps to determine when the airbag should be deployed. Figure 2-5(b) shows that the gyro output is consistent with the high speed camera result.

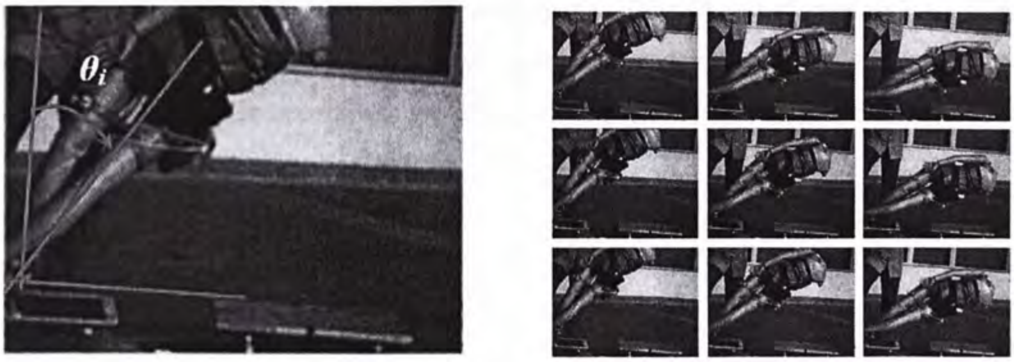

(a) (b)

Figure 2-4) Falling motions captured by the high speed camera:
(a) One frame of falling angle; (b) Films at different time intervals

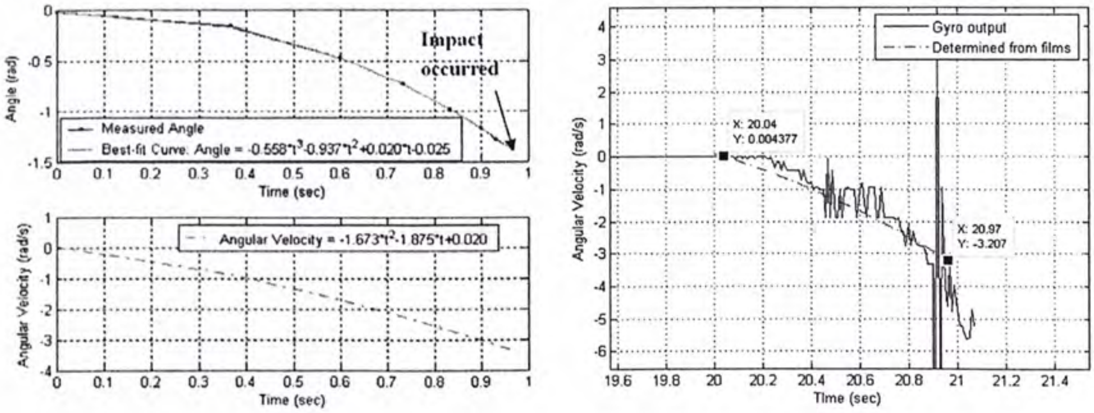

(a) (b)

Figure 2-5) (a) The fall angle and angular rate determined from films; (b) Comparison of high speed camera result and the gyro sensor output

2.3 Mechanical Part

The detail design is presented in Chapter 3. Here only introduce the connection of actuator in mechanical part and the sensing device. The two modules are powered by two individual batteries. The actuator is powered by a 9V battery. The 9V voltage is stepped down to 5V by a voltage regulator L7805CV from ST Microelectronic. The IO port (port B pin 3) of the microcontroller is directly connected to the signal wire of the actuator to transmit a control signal. The sensing device is common grounded with the actuator.

Chapter 3

Mechanical Design

3.1 Similar Products

There are mainly two similar products that use airbags to protect occupants from shocks. They are airbag restraining systems in automobiles, and airbag jacket for motorcycle and horse riders. Some design features of them are adopted in the airbag hip protector.

3.1.1 Airbag Restraining Systems in Automobiles

The airbag hip protector is not exactly the same as the airbag restraining system in automobiles. Both of them deploy airbags when their sensors are triggered, but how they inflate the airbags are different. For the systems in automobiles, the airbag is inflated by large amount of nitrogen gas produced by the combustion of sodium azide and an oxidizer. The airbag is fully inflated for only one-tenth of a second [14]. This process is an exothermic chemical reaction. The airbag volume varies from 35 to 70 liters for the driver side airbag [15].

The airbag restraining system uses energy absorbing mechanism to reduce the impact force exerting on the occupants. In automobile, airbag is deployed into the space between the occupant and the vehicle interior. It has to be deep enough and have sufficient pressure inside so as to prevent severe collision of the occupant [16]. "It provides a passive restraint force which depends on the pressure and the contact area with the occupant. Unlike the belt restraint system in a vehicle, the airbag does not compensate for the weight and size of the occupant in production of restraining force. Thus, a large and heavy occupant may not receive enough restraining force." [16]

"When an airbag restrains the body, the body exerts an equal and opposite force on the airbag. Unlike the immovable steering wheel, the airbag is deflated slowly. This deflation can occur because of the presence of vents in the bag. The force exerted by the body pushes the gas through the vents and thus deflates the bag. Because the gas can only leave at a certain rate (recall the kinetic theory of gases), the bag deflates slowly, and therefore Δt increases." [17] This passage explains why it is necessary to have vents in the airbags of automobiles.

Though the amount of chemical can be reduced for personalized airbag system, it is still dangerous for the elderly to handle such explosive. Therefore, a safer compress gas source - pressurized cylinder is used. Nonetheless, the airbags hip protector also use energy absorbing mechanism and a passive restraining force. The present of vent is adopted in airbag hip protector due to the reason presented.

3.1.2 Airbag Jackets for Motorcycle and House Riders

There are few commercial human-carrying airbag products. One of them is the airbag jackets for motorbike riders and horse riders [19]. These products also use cartridge to inflate the airbags which are used to absorb shocks. The triggering mechanisms are mechanical. They need a wire connecting a key at the inflator and the motorbike or horse. Once the rider falls away from the motorbike or horse (it is a must), the key will be pulled out and the inflator will be sequentially triggered. They will lose function if the key cannot be pulled out.

The mechanism to punch the cartridge for airbag jackets is modified to become electrically triggered. Besides, its ways to install cartridge and compress spring are applicable for airbag hip protectors.

3.2 Mechanism adopted

3.2.1 Time Requirement of Inflator

From the measurements with high speed camera in Section 2.2, we got the falling times and angular velocity profiles of the lateral falling dummy. The falling times range from 0.74s to 0.88s. One of the criteria for a fall is angular velocity larger than about 1.7rad/s. When angular velocity is above this value in a lateral falling, the truck already rotates about the feet for about 30 degrees which is hard for the occupant to retain balance. This is an apparent feature to distinguish lateral falling from other motions such as walking and running. From the velocity angular profiles, the μ IMU gave triggering signal at 0.42s and 0.56s respectively. The time left for airbag deployment is only 0.32s, including the response time of actuator.

3.2.2 Mechanism and Design

The key issue of the mechanical part is how to open the cylinder and deploy the airbag rapidly. The inflator's mechanism (see Figure 3-1) is punching the cartridge only when a falling is detected. It includes a punch mounted on a launcher which consists of a spring and a locking switch. The spring is compressed by screwing. When the locking switch is pressed by the actuator (servo), the compressed spring extends and the punch accelerates towards the pressurized cylinder. The compressed CO_2 flows through the punched hole, passage of biopsy punch and then to the airbag.

Other features like a hole at the end of screw and present of end cap are for easier installation of spring. A long pin can be inserted to the hole of the screw to generate a larger torque; the end cap allows easier pointing screw to the spring chamber in case of hand shaking. Refer to Appendix C for all the dimensions of the inflator and punches.

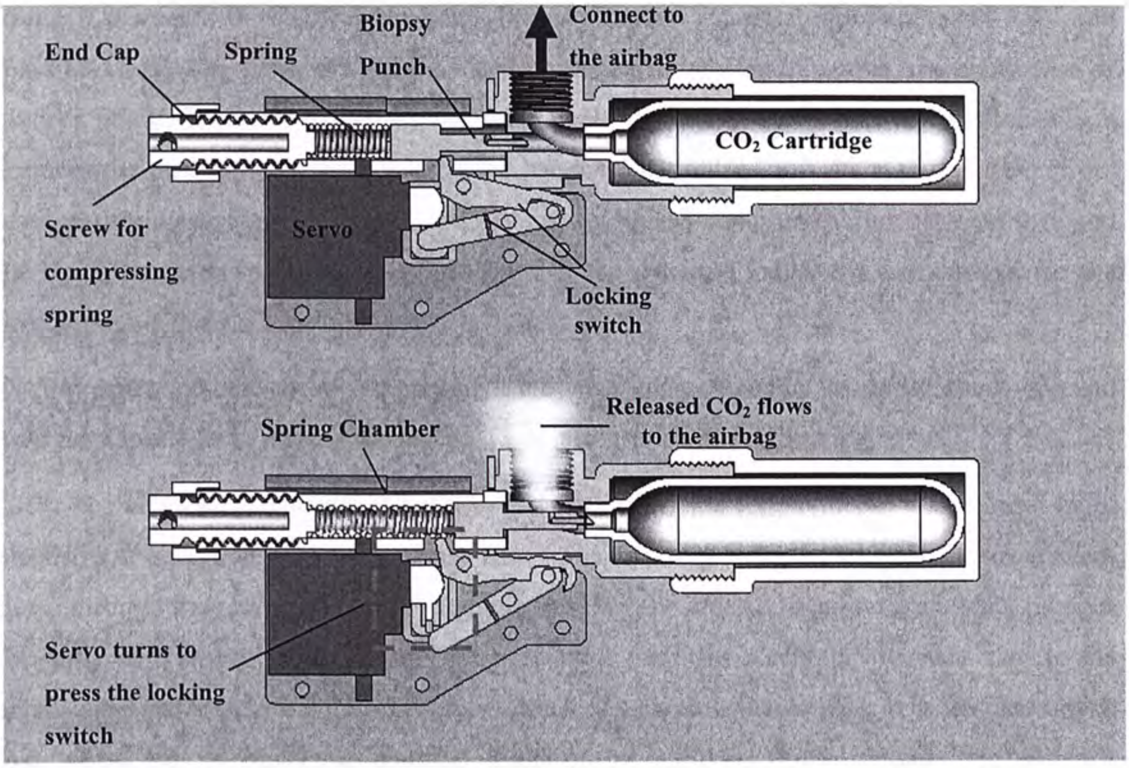

Figure 3-1) The final design of the prototype: (upper) before triggering; (lower) after triggered

3.2.3 Actuator

In order to minimize the mass of electrical actuator, two levers are added to the triggering mechanism (see Figure 3-2). With the configuration, the maximum spring force can be 137.11N. By the balance of moments, the maximum actuation force required is 44.19N.

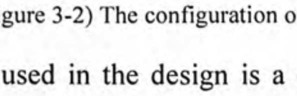

$$F_e > F_s\left(\frac{a}{b}\right)\left(\frac{c}{d}\right)\left(\frac{1}{\cos\beta}\right)$$

$$\text{where } a/b = 0.5,$$

$$\max(c/d) = 0.66,$$

$$\beta = 10^\circ$$

Figure 3-2) The configuration of the triggering mechanism

The electrical actuator used in the design is a commercial available servo BMS-380MAX (from Blue Bird Company) with a maximum torque of 4.1kg-cm (0.402Nm), arm length of

9mm (it increases from 0.5mm to 9mm during actuation), voltage requirement of 4.8V and mass of 17.4g. The servo is selected based on the consideration of torque, mass and ease of control. It can be easily driven by the microcontroller with pulse-width modulation which controls the position of servo angle by the length of the pulse form. Its response time (from servo receiving a signal to compressed gas just releasing) consistently lies between 0.1s and 0.133s. Though its response time is 8 times of the solenoid valve, it's fast enough for the prototype to deploy a 2.5L airbag within 0.3s.

During operation, the servo is commanded by the microcontroller to rotate about 40° and hold for about 0.2s to release the punch. Then it returns to its original angle.

Other actuators were considered but they did not satisfy the requirements – small and light, electrical triggered and short response time. The first one is solenoid [20]. When current flows through the solenoid coils, a magnetic field will be created to attract a movable plunger forwards until impact with a stop. The maximum force for solenoid with size near to the servo is typically below 20N. The other actuator is piezo-actuator [21]. It is designed such that when the piezoelectric material expands by applying high voltage, the actuator compresses in the orthogonal axis. Its block force can be as high as 150N and response time is as short as a few milli-seconds. However, its displacement is very small, just a few hundred microns. Moreover, if the piezo-actuator is used to lock the spring directly, more than one piezo-actuator is needed to stack together to get enough displacement (at least 1mm). And the size will be 6 times as the servo.

3.2.4 Punch

Punching a cartridge cap (about 0.3mm stainless steel) is a problem of high-speed plate penetration dynamics. However, the focus of the mechanical design is to demonstrate the portable airbag system. Thus, there isn't any deep study on penetration dynamics in this project. Only basic knowledge is known: the depth and the size of punctured hole depend on the stiffness, mass and velocity of the punch, and also the stiffness of the cap [22]. In addition, the stress acting on the cap will be higher and more destructive if a punch of smaller contact area is used [23]. Unfortunately, it is not just a problem to make a large hole. It is because the punch itself will block the hole and reduce flow of CO_2. Special design is required to solve the blocking problem. For instance, a click-pen structure allows the cartridge to be pushed back by jet after impact.

Without any simulation or calculation, a spring (with spring constant of 1513.89N/m) disarmed from an air-gun was first used to puncture the cartridge together with an iron nail. Pyramidal shape, U-shape, star-shape and hollow shape had been tried (see Figure 3-3). The first three punches were manually modified from steel screws.

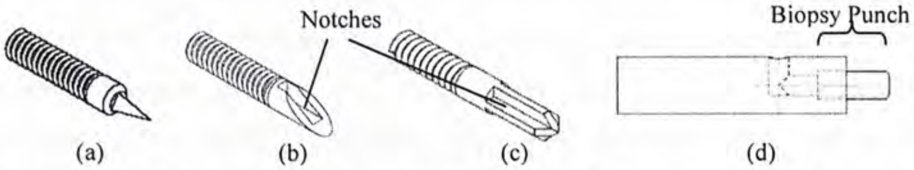

Figure 3-3) Punch head of: (a) pyramidal shape; (b) U-shape; (c) star-shape; and (d) hollow shape

The threads at the end of punches are for adjusting the initial separation of the punches and cartridge. Pyramidal shape fully blocks the hole. U-shape and star-shape punches block the hole but there is some gap at the notches. Star-shape results larger flow because of more notches. With star-shape punch, the inflator can deploy an airbag of 2.06L within 0.6s.

Hollow shape is obtained by attaching a section of biopsy punch (inner diameter of 1.45mm, wall thickness of 0.3mm) at an aluminum rod with L-shape passage inside. The biopsy punch also has blocking if the head is a flat circle. It was observed that if the head was flat, the chopped cap was blown inside the passage of punch, leading to blocking. To solve the problem, its head is filed with about 45 degrees. This shape gave the shortest inflation time and consistent punctures. (The inflation time is measured from the film captured by a digital camera (film rate of 30Hz). It is defined as from the time when the inflator is given a signal to the time the airbag is fully expanded. The maximum error of using this method is 0.03s.) Thus, it replaced the star punch in the prototype.

Regarding the initial separation of punch and cartridge, two approaches had been tested. The first approach is to convert all the elastic potential energy of the nail into the kinetic energy, and the nail alone accelerated towards the cap. Another one is to accelerate the nail for a short distance and then the spring pressed the nail to the cap. The mass and punch angle of the nail were 1.31g and 19° respectively; a spring of spring constant of 1513.89N/m was used; the initial compression of spring is 5.35cm; the final compression of spring for 1st approach is 3.06cm (the long extension of the setup); the final compression of spring for 2nd approach is 4.1cm.

Using the first approach, the cap was intact after the impact with the nail. By Newton's second law, $F = ma = m\, dv/dt$. The impact time is given by $\sqrt{m/K}$, where K is the stiffness of the nail. This gives $F = \sqrt{mK}dv$. From this simple relation, it can see that a larger velocity or mass is required to increase the impact force for penetration. A larger velocity requires a longer spring of same stiffness or a stiffer spring. For the second approach, the spring elongated for shorter length 1.25cm but penetrated the cap. From this simple test, it determined that the second approach is more effective under the same of spring length and strength.

After decided to use the 2nd approach, several measurements were conducted to determine the relation between initial spring compression and dimensions of holes, also the initial separation and dimensions of holes. Under the same initial separation between punch and cartridge, the dimensions of holes increase with the initial spring compression (see Figure 3-4(a)). Regarding the initial separation, a shorter distance creates smaller hole and even cannot penetrate (see Figure 3-4(b)). As mention before, the punch needs certain velocity in order to penetrate the cap. A short distance doesn't allow enough time for the punch to accelerate. However, allowing the punch to accelerate for full length won't penetrate the cap too. Therefore, it has to take balance between the velocity and the remaining spring force during impact, i.e. the initial separation.

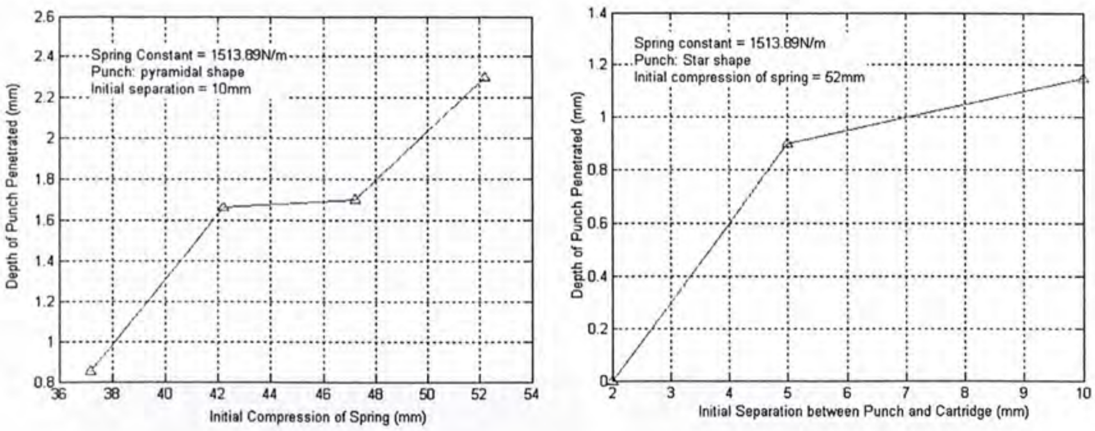

(a) (b)

Figure 3-4) (a) The depth of punch penetrated vs. initial compression of spring; (b) The depth of punch penetrated vs. initial separation between punch and cartridge

In the above test, the spring used has a spring constant of 1513.89N/m and free length of 85mm. In order to minimize the size of inflator, it is replaced by a musical spring with spring constant of 8.09N/mm, working length of 16.3mm and free length of 35mm. The full compression of the smaller spring is used to give the required velocity and spring force during impact.

3.2.5 Airbags

The material used in airbag restraining system of automobile is nylon fabric. Some Talcum powder or corn starch is coated on the airbag to prevent fabric from sticking together [18]. The material is thick and hard to fold well for hiding in belt. PVC material (PVC ball) was tried in the trial models. It was frozen by the cold CO_2 released from cartridge and became very brittle. The PVC ball burst eventually. Finally, a material of nylon coated with PVC on one side was used to make the airbags for the following inflator model because of easy available and durable for impacts. However, the folding of airbag was not considered at the early stage.

Urethane film is used to make the air cushions of airbag jackets for motorcycle riders [19]. With this material, the air cushions can be folded and hidden well in the jackets. The manufacturer also performed drop test to prove the protectiveness of such cushions. If the development of the system is mature, the current material can be replaced with urethane film for easier hiding in the belt.

The airbags of the prototype are cylindrical (see Figure 3-5) because of easy manufacturing and analysis. They are sewed with nylon wires. Each has one inlet connected to the inflator through a pipe and one outlet orifice. Nuts are stuck at the inlet and outlet for installation of fittings.

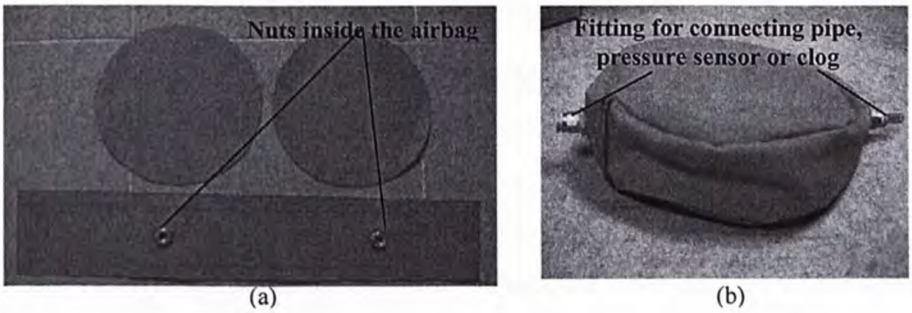

(a) (b)

Figure 3-5) (a) The segments of airbag with two nuts stuck inside; (b) the cylindrical airbag

3.2.6 Other Mechanisms Tried

Solenoid Valve

The first trial mechanism consists of a solenoid valve (SLG5404-04 from E-MC Company) which has response time as short as 15ms, a mechanical inflator and two fittings. The gas source is a Zefal's 12g threaded CO_2 cartridge which contains 12g compressed CO_2 at a pressure of about 70bars. The mechanical inflator punctures the cartridge and the valve traps the released CO_2 before inflating the airbag. The setup of the trial model is shown in Figure 3-6.

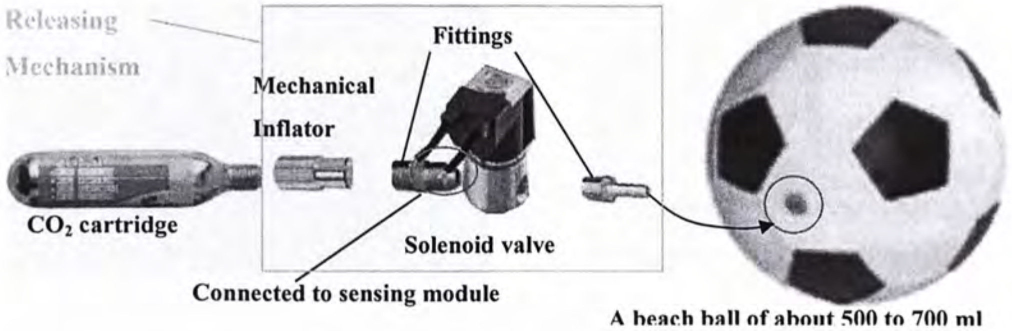

Figure 3-6) The setup of the trial model

The inflation time of the first trial was about 2.7s which was nearly triple to our limit (1s). It was because there was observable, serious leakage at the junction between the cartridge and the mechanical inflator during the installation of the cartridge. This was due to poor fitting. Moreover, even refine the fitting between the cartridge and the mechanical inflator, the orifice of the valve is not perfectly closed to trap all the released CO_2. Cartridge has to be replaced after somedays though the user does not fall. Therefore, the mechanism was abondoned.

Scratching Mechanism

Besides directly punching method, scratching mechanism had also been tried but failed. Figure 3-7(a) and (b) show the prototype and the internal structure of the scratching mechanism respectively. This mechanism was tried to solve the problem of blocking. The idea is to use the spring to push one end of the hook which is made of the same material of nail. Then the sharp end of the hook scratches on the cap of the cartridge. The different length ratio aims to increase the torque of scratching; meanwhile, the rate of loading (angular velocity) is kept the same. However, the hook cannot produce a larger and unblocked hole, and it is even blunted. The reason behind is that the material has enough strength to penetrate the cap vertically but not enough shear strength to scratch the cap.

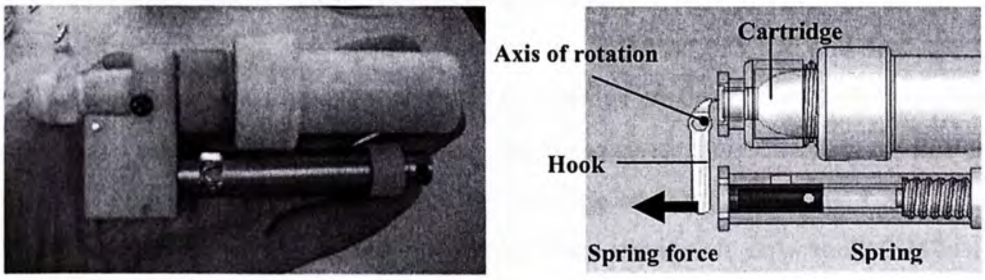

(a) (b)

Figure 3-7) (a) Prototype of the scratching mechanism; (b) Internal structure

3.3 Prototype

3.3.1 Implementation

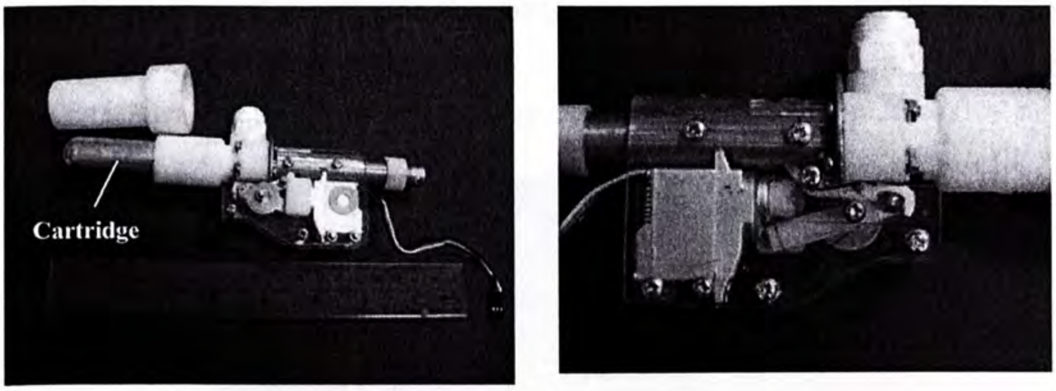

Figure 3-8) The prototype of the inflator

The prototype has a total length of 19cm, and weight (including 42.5g cartridge) of 253.42g. Except the cartridge (from Gamo Company), servo and spring (from RS Components Ltd.), the other parts are self-design and self-manufacture.

The final airbag system consists of two airbags. Thus, it is important to know if the inflator can deploy two airbags at the same time. To check this, the inflator was connected to two ~2550ml airbags with two 24cm long pipes (see Figure 3-9). The total length of pipes was about half of the mean waist circumstance of 69 elderly (information provided by the Department of Orthopaedics and Traumatology of CUHK). The airbag pressures were measured by pressure sensors. Two additional pressure sensors were connected at the teefitting to detect the start of flow. The inflator is triggered with a RC controller. A digital camera of film rate 60Hz was used to capture the inflation process and find the time to maximum volume. It was found that a 12g CO_2 cartridge needs at least 0.367s (excluding the response time actuator 0.133s) to expand the airbags to their 70-80% of full volume. Therefore, it was replaced with a larger CO_2 cartridge of 38g (12cm long x 3cm diameter). The larger cartridge was far enough to deploy two airbags. It only took 0.217s to fully expand the airbags. The pressure profiles of two different sizes of cartridges are plotted in Figure 3-10. Both cartridges have an initial pressure of 70bars. The same rate of pressure rise in Figure 3-10 for both cartridges indicates that the initial mass flow rates from both cartridges are equal. However, the mass flow rate of 38g cartridge drops in a slower rate. Thus, 38g cartridge has a faster inflation.

To make the airbag system work, the 12g cartridge is not feasible while the 38g cartridge is excessive if the orifice size at cartridge cap remains unchanged. Moreover, the experiment shows that it's feasible to inflate two airbags about 0.3s by increasing the mass of CO_2.

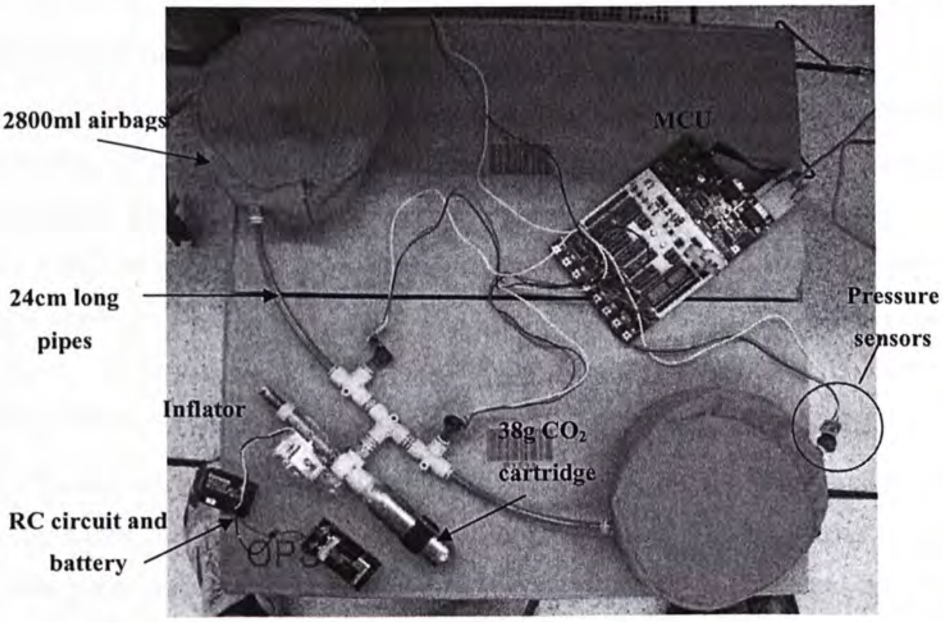

Figure 3-9) The connection of inflator with 38g CO_2 cartridge and two ~2550ml airbags

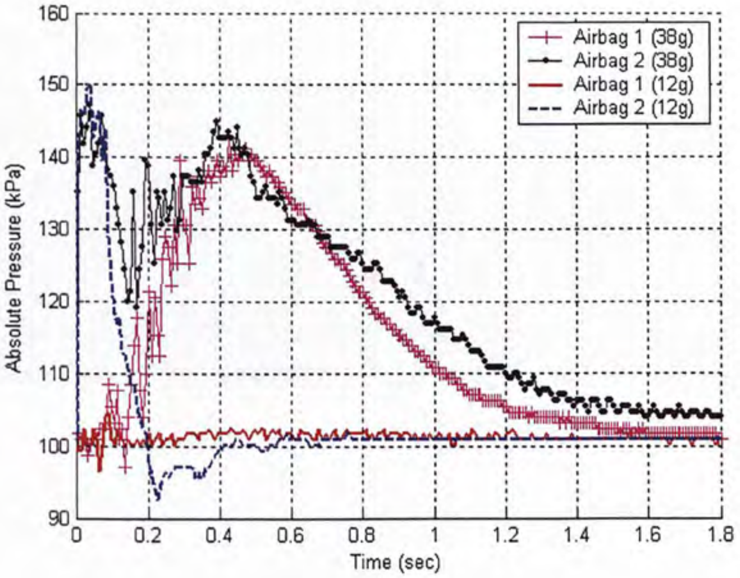

Figure 3-10) The pressure profiles of two different sizes of cartridges. The pressure of airbag 1 rises up less rapidly because of larger leakage hole.

3.3.2 Demonstration

The prototype was integrated with the μIMU in a demonstration. The integrated system was attached to the human with a belt. The volume of the airbag was 2.5L and the cartridge used is 12g package. The human walked in front of a mattress and then fell laterally onto it. Different from impact experiment, the demonstration needed not to measure the impact force entering to the hip joint. Therefore, protecting prosecution of adding mattress was acceptable. Furthermore, the subject was confirmed to fall onto the mattress without any injuries before the demonstration.

When the human fell about 30 degrees (at 0.53s), the μIMU detected falling and triggered the inflator. One-tenth second later, the airbag was half inflated. The airbag was fully inflated before hitting the mattress. The human repeated the action three times and the airbag was successfully deployed in each trials.

The demonstration shows that under free falling, the inflator can response fast enough to deploy an airbag for protection.

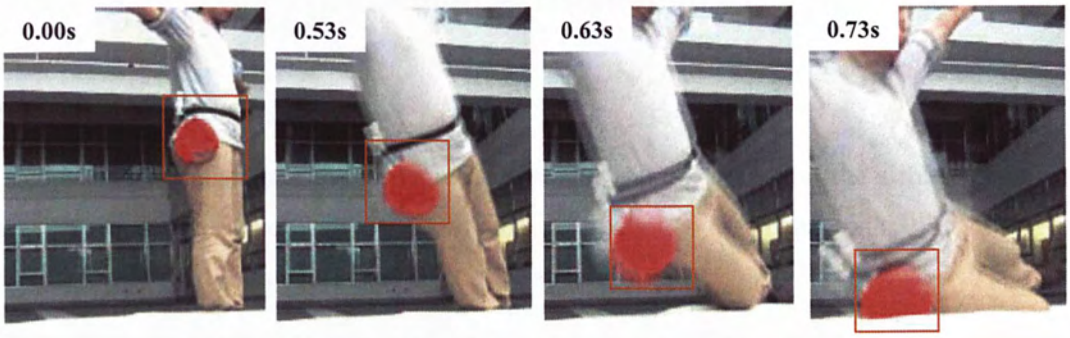

Figure 3-11) Airbag demo with independent μIMU and airbag system

Chapter 4

Inflation Estimation

4.1 Theory and Model

This part aims to estimate the pressure change and volume change of the airbag (diaphragm) over the inflation period, also the inflation time when the airbag attains the volume and pressure required to attenuate the impact force.

Finite Element Method is not used because of its complexity and time-consumption. Its accuracy depends on boundary conditions, material properties, geometry of object, adherence of parts and meshing. Experiments may be needed to find the material properties and check the FEM model. The simulation of out-of-position airbag deployment in automobile is multi-physic and dynamic problem. It involves the airbag deployment (interaction between airbag membrane and gas flow) and the collision between airbag and occupant simultaneously [38][39][40]. To attain a high accuracy, the mesh size and time step have to be small which increases the computational time, especially for the simulation of impact between two objects. To simplify the problem, the simulation used here is divided into two parts, the airbag deployment by inflator and the impact of occupant with a deployed airbag, which involve simple differential equations.

The simulation model of the inflator is shown in Figure 4-1. It includes the compressed gas cylinder, pipes and airbags which have some leakage hole. To make it simpler, the cylinder is only connected to only one airbag through a pipe. The cylinder is modeled as a chamber of fixed volume while the airbag is a diaphragm with variable volume, and it has a pipe as the inlet and an orifice as the outlet (representing the leakage hole). The pressures and temperatures are assumed to be constant throughout the volumes. It is a lumped-parameter assumption. The sizes of airbags are found to be small enough for the lumped-parameter assumption to hold in the experiments.

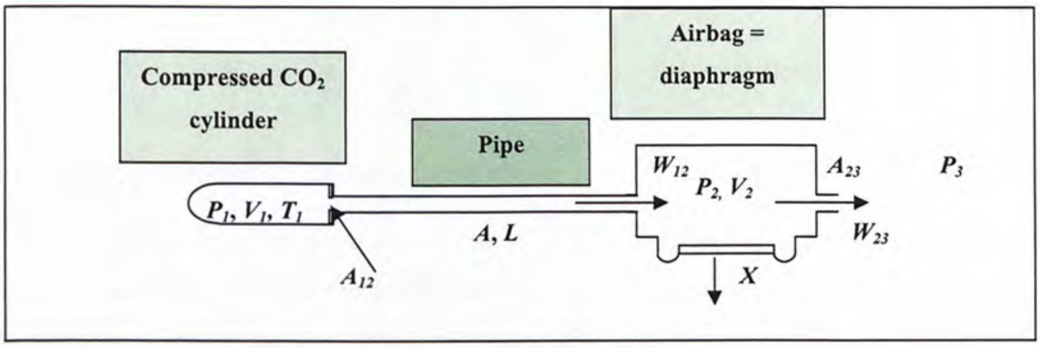

Figure 4-1) The simulation model of the inflator

The main idea of the model is considering the net mass flow rate into the diaphragm. At the same time, the pressure inside the cylinder which affects the inlet mass flow rate is updated. However, the simulation model does not involve the interaction between gas and the airbag membrane. In fact, the gas is thought to be under free expansion inside the airbag. Hence, the work needed to overcome the atmospheric pressure and airbag material tension is not simulated.

The equations describing the model are:

Case i) Before the airbag is fully inflated, the airbag pressure is assumed to maintain atmospheric pressure:

$$\frac{dP_2}{dt} = 0 \Rightarrow \frac{P_2}{RT_2}\frac{dV_2}{dt} = W_{12} - W_{23} \qquad \text{(B.2.1)}$$

Case ii) After the airbag is fully inflated, the airbag pressure starts to increase from atmospheric pressure and hence the mass flow rate W_{23} is non-zero:

$$\frac{dV_2}{dt} = 0 \Rightarrow \frac{V_2}{nRT_2}\frac{dP_2}{dt} = W_{12} - W_{23} \qquad \text{(B.2.2)}$$

The term W_{12} can be evaluated from:

$$W_{12} = \frac{A_{12}P_1}{\sqrt{T_1}}\left\{\frac{2\gamma}{R(\gamma-1)}\left[\left(\frac{P_2}{P_1}\right)^{2/\gamma} - \left(\frac{P_2}{P_1}\right)^{\gamma+1/\gamma}\right]\right\}^{1/2} \quad \text{for subsonic flow;}$$

$$W_{12} = \frac{A_{12}P_1}{\sqrt{T_1}}\left\{\frac{\gamma}{R}\left[\left(\frac{2}{\gamma+1}\right)^{(\gamma+1)/(\gamma-1)}\right]\right\}^{1/2} \text{ for sonic flow.}$$

The term W_{23} is donated by the same forms above.

The gas inside the chamber is assumed to be ideal. Hence the mass of gas is simply related to pressure inside the chamber by ideal gas law. Eventually the following equation can be derived to describe the pressure drop inside the chamber during discharge:

$$\frac{dP_1}{P_1} = -n\sqrt{\frac{T_1}{T_0}}N_{12}d\left(\frac{KR\sqrt{T_0}A_{12}}{V_1}t\right) \tag{B.3.1}$$

where

$$N_{12} = \frac{W_{12}}{W_{cr}} = \left[\frac{\left(\frac{P_2}{P_1}\right)^{2/\gamma} - \left(\frac{P_2}{P_1}\right)^{(\gamma+1)/\gamma}}{\frac{\gamma-1}{2}\left(\frac{2}{\gamma+1}\right)^{(\gamma+1)/(\gamma-1)}}\right]^{1/2} \tag{B.1.1}$$

$$K = \left[\frac{\gamma}{R}\left(\frac{2}{\gamma+1}\right)^{(\gamma+1)/(\gamma-1)}\right]^{1/2} \tag{B.1.2}$$

For easier understand and how the equations are derived, please refer to Appendix A, B and C.

4.2 Validation of Model

The approach of validating the model is step by step as the follow: first check the applicability of basic equations such as mass flow rate equations; second adjust some important parameters such as discharge coefficient from experimental data to compensate the errors in the experimental setups; third validate the equation describing the pressure change during charging at constant volume. It is performed by discharging gas from one chamber to another one; fourth use experimental data to find the equivalent sizes of leakage holes of airbags; fifth validate the equation describing both the pressure and volume change during charging. It is performed by discharging gas from a chamber to an airbag. The pressure change part is validated in step three; finally check the effect of the length of pipe, to see whether it is necessary to include time delay due to addition of pipe.

All the measurements were repeated three times and the data obtained were consistent.

4.2.1 Testing Equipment

Two chambers from the SMC Company [29] are used to represent the cartridge (the smaller one) and the airbag (the larger one). The dimensions of the smaller chamber are 6.3cm diameter and 16.1cm long (~500ml), and those of the larger one are 8cm diameter and 20cm long (~1000ml). The solenoid valve VX2320-03 and other speed controlling valves, AS2001F and AS1001F, from the same company is used to give orifices of about 6mm^2, 3.5 mm^2 and 1.5 mm^2 respectively.

The pressure sensors used to measure the static pressure is model MPX5700AS (from Freescale Semiconductor Inc.). It can measure the absolute pressure from 15kPa up to 700kPa with an accuracy of ±2.5%. The pressure of compressed air used in the experiment is limited to the maximum measurable pressure of the sensor.

4.2.2 Preprocessing of Pressure Sensor Outputs

Since the pressures measured from sensors have oscillation (see Figure 4-2(a)), the time derivatives of these signals will have enlarged oscillation (see Figure 4-2(b)). Therefore, the signals are smoothed before analysis. The smoothing method used is to approximate every 20 sequent points by a quadratic curve, and the end points of the sequent curves are concurrent. Figure 4-2(c) shows the time derivatives of smoothed pressures.

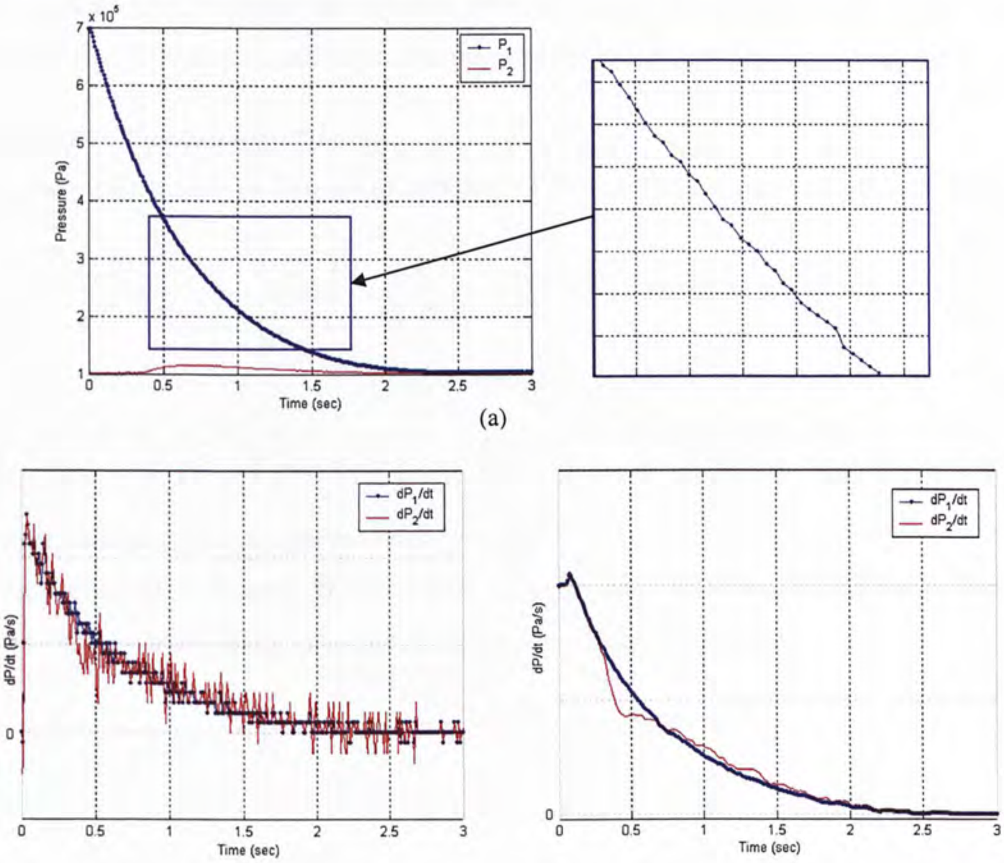

(a)

(b)

(c)

Figure 4-2) (a) The unsmoothed pressure outputs; (b) the time derivatives of unsmoothed pressures; (c) the time derivatives of smoothed pressures

4.2.3 Validation for Basic Equations

There are two types of basic equations which calculate the mass flow rate through an orifice and pressure change inside a fixed volume chamber respectively. During the experiment, the temperatures inside the chambers were measured by a thermocouple. The flow with compressed air at the pressure ≤ 0.8MPa is found to be isothermal: temperature drop during discharge is within 3°C. Thus, the value of γ is set to be 1 for compressed air in the following simulations.

Regarding the static pressure inside the chamber measured by sensor can be approximated as the total pressure. It is because the chamber inner cross-sectional area is much larger than that of the orifice (500 times), and hence the velocity of flow in the chamber is very slow.

i) ***Mass flow rate through an orifice***

The mass flow rate equations through an orifice (B.1.9) and (B.1.12) are recalled here for air,

$$W_{12} = \frac{A_{12}P_1}{\sqrt{T_1}}\left\{\frac{2\gamma}{R(\gamma-1)}\left[\left(\frac{P_2}{P_1}\right)^{2/\gamma} - \left(\frac{P_2}{P_1}\right)^{\gamma+1/\gamma}\right]\right\}^{1/2} \quad \text{for subsonic flow } \left(\frac{P_2}{P_1} > 0.528\right);$$

$$W_{12} = \frac{A_{12}P_1}{\sqrt{T_1}}\left\{\frac{\gamma}{R}\left[\left(\frac{2}{\gamma+1}\right)^{(\gamma+1)/(\gamma-1)}\right]\right\}^{1/2} \quad \text{for sonic flow } \left(\frac{P_2}{P_1} \le 0.528\right).$$

ii) ***Pressure change of the compressed gas cylinder***

Recall Equations (B.3.7) and (B.3.8) which describe the instantaneous pressure in the compressed gas cylinder under subsonic flow and sonic flow respectively:

$$\frac{dP_1}{P_1} = -N_{12}d\left(\frac{KR\sqrt{T_0}A_{12}}{V_1}t\right) = -N_{12}d\tau \qquad \text{(B.3.7)}$$

$$P_1 = P_0e^{-\tau} \qquad \text{(B.3.8)}$$

where $\tau = \dfrac{KR\sqrt{T_0}A_{12}}{V_1}t$

For subsonic flow, N_{12} will vary with the pressure ratio and the differential equation is solved by Matlab Simulink.

Experimental Setup

Figure 4-3(a) shows the experimental setup for measuring the mass flow rate across an orifice from the 500ml chamber. The solenoid valve was connected to one exit of the chamber to give the orifice of the chamber. (For other smaller orifice, additional speed controlling valve is connected to the outlet of the solenoid valve.) Three pressure sensors were connected to measure: the instantaneous total pressure inside the chamber (Sensor 1), the instantaneous static pressure just upstream of the orifice (Sensor 2) and the instantaneous static pressure downstream of the orifice (Sensor 3). A thermocouple was also inserted to measure the temperature inside the chamber. The chamber was first filled with compressed air at about 250kPa, 400kPa and 550kPa. The measurements were repeated three times for each pressure. The air was allowed to drop to initial chamber temperature before discharge. The pressure sensors were connected to ATMEL ATmega16L MCU for digitalize the output signals and then transmitted to computer.

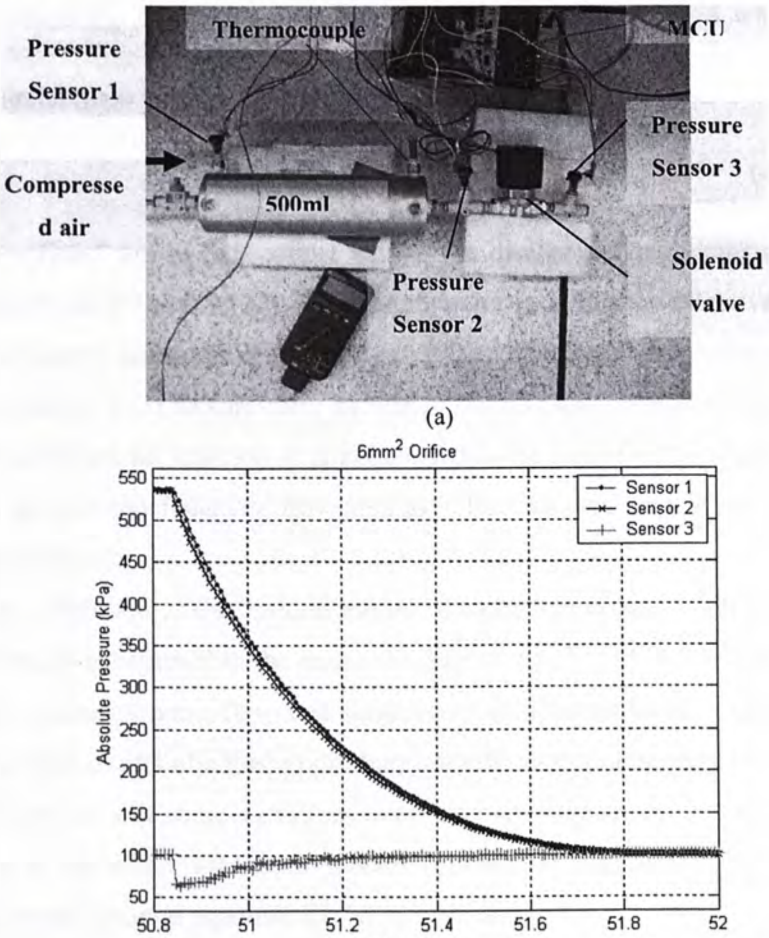

(a)

(b)

Figure 4-3) (a) Experimental setup; (b) the pressure sensor output

Figure 4-3(b) shows the pressure sensor outputs. The drop of downstream static pressure from Sensor 3 is due to the air flow. The pressure from Sensor 1 is higher than that from Sensor 2. It is because the flow velocity just upstream of the orifice is hundred times higher than that inside the chamber. Therefore, the pressure from Sensor 1 is regarded as the upstream total pressure.

Direct Substitution Results

The mass flow is determined experimentally by using the relation of mass and pressure: $M_1 = \frac{P_1 V_1}{RT_1}$ where V_1, T_1 and R are constants. By taking differentiation with respect to time, the experimental mass flow rate is obtained:

$$W_{12} = -\frac{dM_1}{dt} = -\frac{V_1}{RT_1}\frac{dP_1}{dt} \qquad (4.2\text{-}1)$$

Since the "orifices" are in fact poppet valves, the discharge coefficients of them vary with pressure ratio from 0.7 to 0.9 [27]. The manufacturer specifies the effective area at a specific condition: constant upstream pressure of 0.6MPa (absolute) and downstream pressure of 0.1MPa (absolute), i.e. pressure ratio of 0.167. Besides, the manufacturer does not mention about the coefficient of velocity. It is believed that the manufacturer combines the velocity coefficient and the coefficient of flow area as "effective area", but it should be actually the discharge coefficient.

To check the validation of the basic equations, the pressure sensors' outputs (pressure against time) are directly substituted to the equations. Figure 4-4, Figure 4-5 and Figure 4-6 show the substitution results of mass flow rate equations for different initial chamber pressures and orifice sizes. The results of adjusted discharge coefficients match more with the experimental data. But there are still some variations even after the adjustment of discharge coefficients. This is due to the shock loss from sudden contraction. Figure 4-7 shows the substitution results of pressure change equation for 6mm^2 orifice.

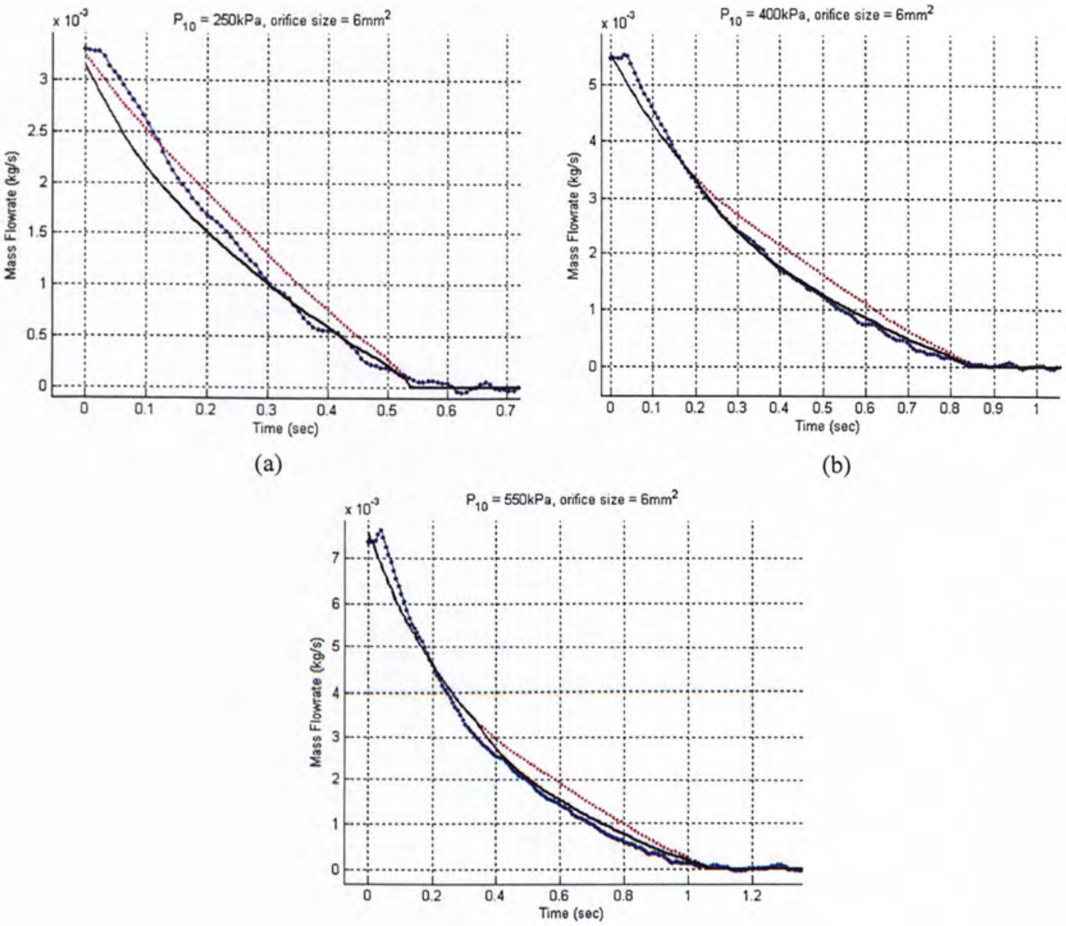

(a) (b)

(c)

Figure 4-4) Substitution of sensors' outputs to the mass flow rate equations (for orifice size of 6mm^2; different initial chamber pressures: (a) 250kPa, (b) 400kPa and (c) 550kPa). The dotted solid line (blue) is the pressure sensor outputs; the dark solid line (black) is the mass flow rate equation of fixed orifice size; the light solid (red) is the mass flow rate equation of adjusted orifice size.

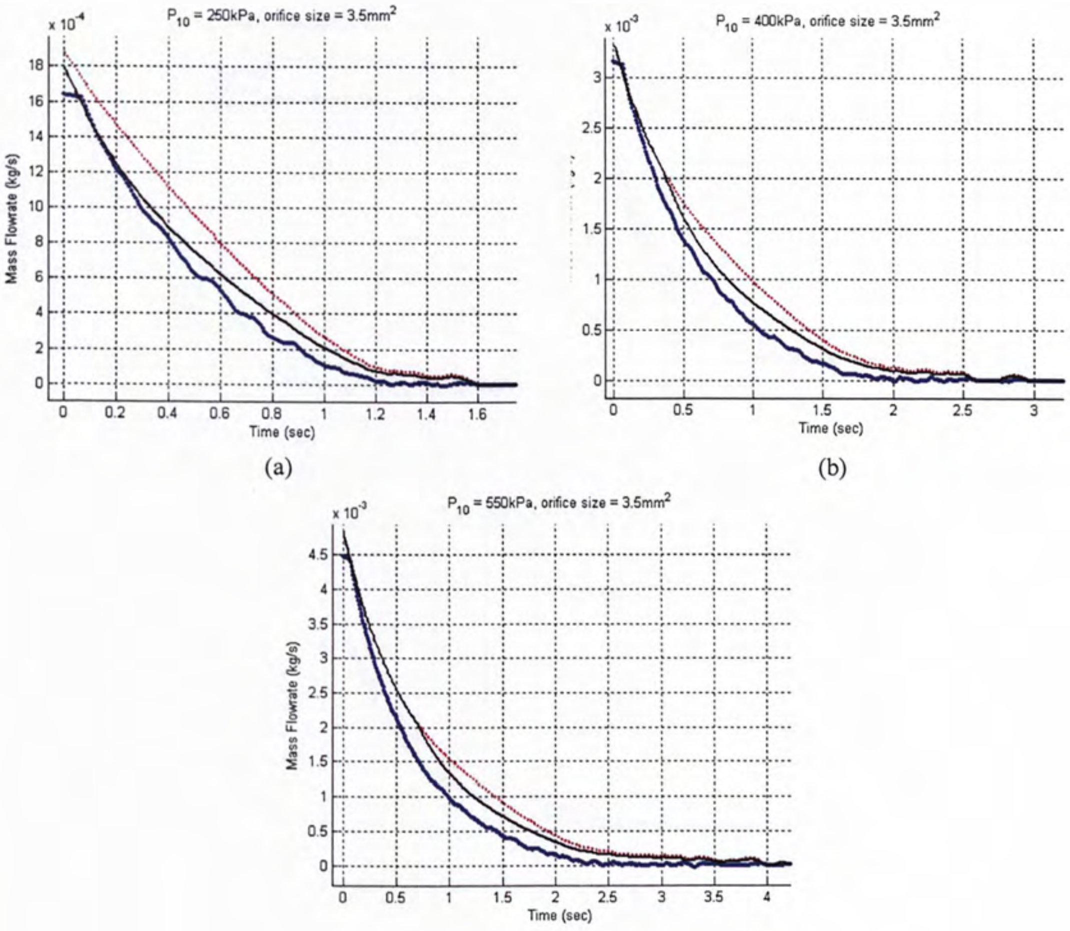

(a) (b)

(c)

Figure 4-5) Substitution of sensors' outputs to the mass flow rate equations (for orifice size of 3.5mm^2; different initial chamber pressures: (a) 250kPa, (b) 400kPa and (c) 550kPa).

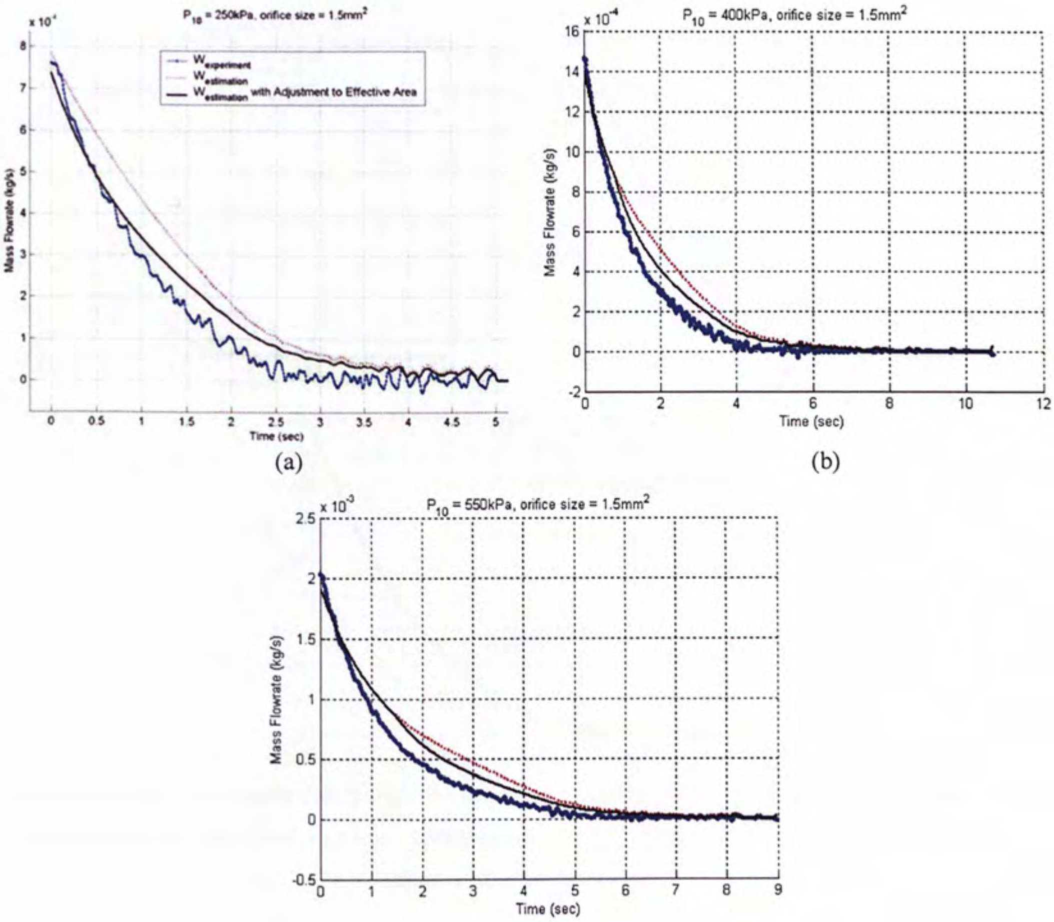

(a) (b)

(c)

Figure 4-6) Substitution of sensors' outputs to the mass flow rate equations (for orifice size of 1.5mm^2; different initial chamber pressures: (a) 250kPa, (b) 400kPa and (c) 550kPa).

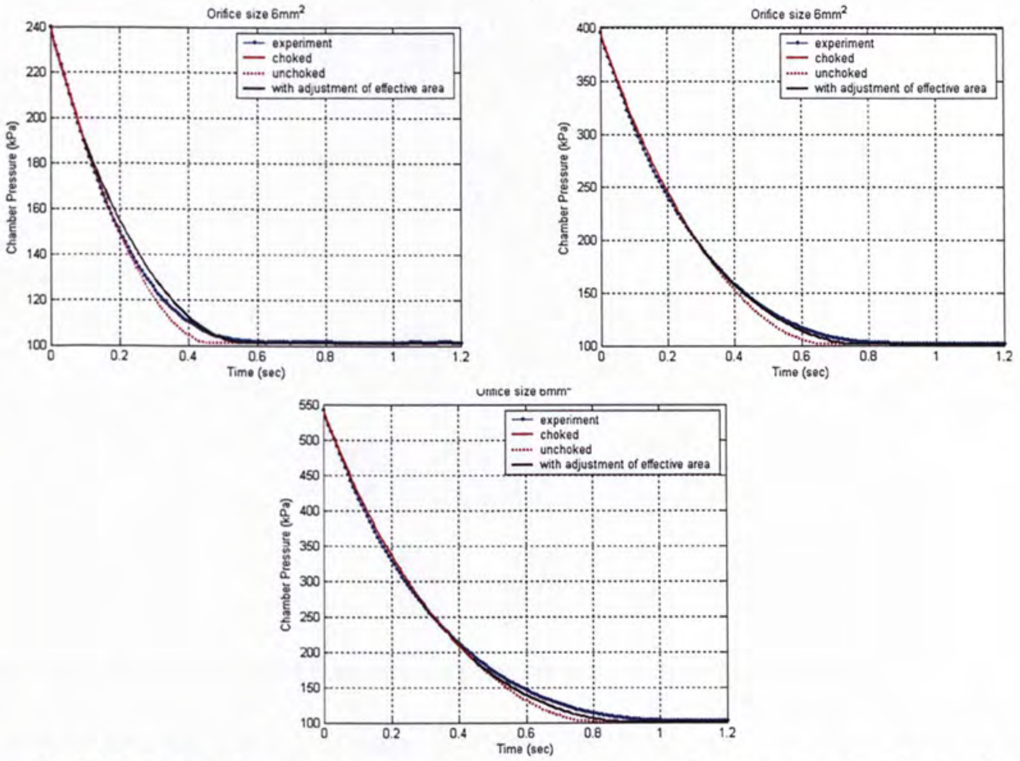

Figure 4-7) Substitution of sensors' outputs to the pressure change equation (P_1 against time) for 6mm^2 orifice. (Blue line: Experimental data; Red line: Approximation by Equations; Black line: Approximation with adjustment of orifice size)

4.2.4 Adjustment of Discharge Coefficients

There are only three variables, P_1, P_2 and A_{12}, in the mass flow rate equation. (The temperature is constant as the flow process is isothermal, and the specific heat ratio is also constant as the compressed air is calorically perfect at room temperature.) The difference between the equations and the experimental results should be due to either one of the variables. Consider the partial derivative of the mass flow rate among these variables:

For sonic flow:

$$\frac{\partial W_{12}}{\partial A_{12}} = \frac{P_1}{\sqrt{T_1}}\left\{\frac{\gamma}{R}\left[\left(\frac{2}{\gamma+1}\right)^{(\gamma+1)/(\gamma-1)}\right]\right\}^{1/2}$$

$$\frac{\partial W_{12}}{\partial P_1} = \frac{A_{12}}{\sqrt{T_1}} \left\{ \frac{\gamma}{R} \left[\left(\frac{2}{\gamma + 1} \right)^{(\gamma+1)/(\gamma-1)} \right] \right\}^{1/2}$$

$$\frac{\partial W_{12}}{\partial P_2} = 0$$

For subsonic flow:

$$\frac{\partial W_{12}}{\partial A_{12}} = \frac{P_1}{\sqrt{T_1}} f\left(\frac{P_2}{P_1} \right)$$

$$\frac{\partial W_{12}}{\partial P_1} = \frac{A_{12}}{\sqrt{T_1}} \left[f\left(\frac{P_2}{P_1} \right) + g\left(\frac{P_2}{P_1} \right) \right]$$

$$\frac{\partial W_{12}}{\partial P_2} = -\frac{A_{12} P_1}{\sqrt{T_1} P_2} g\left(\frac{P_2}{P_1} \right)$$

where $f(P_2/P_1)$ and $g(P_2/P_1)$ are two different functions of pressure ratio P_2/P_1.

For sonic flow, the change of mass flow rate due to change in A_{12} is largest and it is independent of P_2. Since the magnitude order of P_1 is 10^5 and A_{12} is 10^{-6}, $\frac{\partial W_{12}}{\partial A_{12}}$ is much larger than $\frac{\partial W_{12}}{\partial P_1}$. Therefore, A_{12} dominates for sonic flow.

For subsonic flow, the change of mass flow rate due to change in A_{12} is also largest. Again, A_{12} dominates for subsonic flow. Therefore, assuming the velocity coefficient equal to 1, the discharge coefficient is the main factor causing variation.

To reduce variation from measurement of the simulations behind, the discharge coefficients are adjusted to be the experimental mass flow rate divided by the values of mass flow rate equation with a constant physical orifice area. However, as seen from Figure 4-8, with different initial chamber pressures, the pressures drop in different rate. The higher the chamber pressures, the lower the pressure dropping rate. For instance, when the pressure of initial value 700kPa drops to 550kPa, its dropping rate is lower than that of initial value of

550kPa. But the downstream pressures are the same. The reason behind is that the chamber used here are cylinder shape with sudden contraction, but the air flows in a nozzle shape. The stream is separated from the chamber wall and some air is trapped between the wall and the stream. When pressure drops, the trapped air flows back to the stream, reducing the chamber pressure dropping rate but increasing the chamber pressure measured by the sensors. Therefore, the discharge coefficient is taken from the lower initial chamber for the pressure ratios less than 0.4, and the curve joining the initial values at different initial chamber pressures for the remaining ratios (see Figure 4-9).

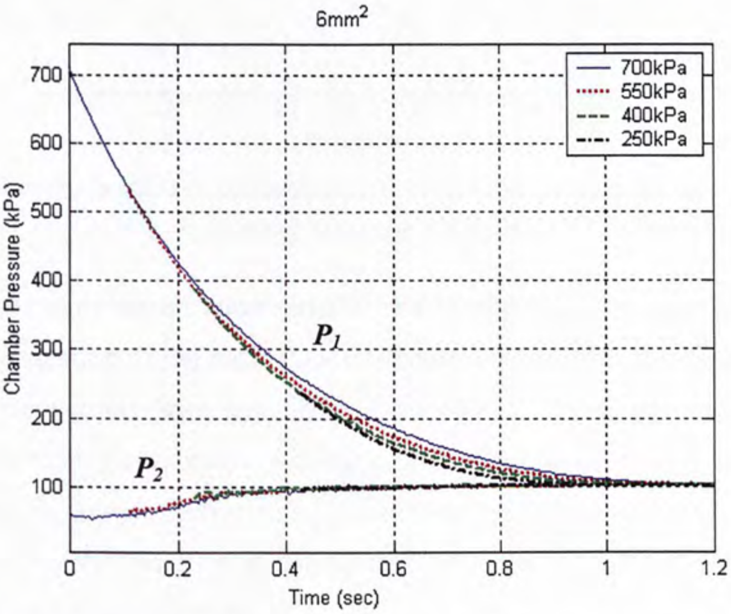

Figure 4-8) The chamber pressures (P_1) of different initial values; the bottom curves are the corresponding downstream pressures (P_2)

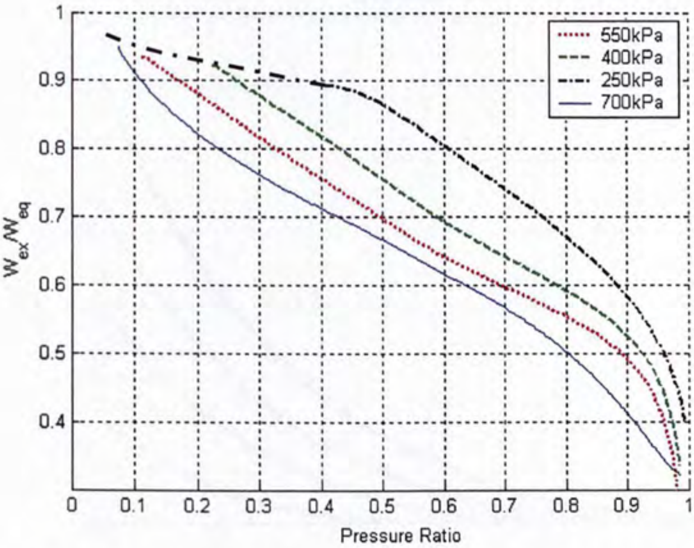

Figure 4-9) The discharge coefficients evaluated for different chamber pressures; the dark -. line is taken as the discharge coefficient in simulation

Besides the errors in the above three variables, the invalidation of isentropic assumption also contribute the derivation of the mass flow rate equations from the experimental values. The mass flow rate equations have assumed that the flow is isentropic which requires both adiabatic and reversible conditions. Adiabatic process means no heat is added to or taken from away from the system; Reversible process means no dissipation such as frictional loss in the system. However, the flow of compressed air in the experiment is almost isothermal which violate the adiabatic assumption.

Simulation

The inputs to the program estimating the chamber pressure are the initial chamber pressure (P_{10}) and the downstream (atmospheric) pressure (P_2), both are constants. With the discharge coefficient obtained from last part, the result is shown in Figure 4-10.

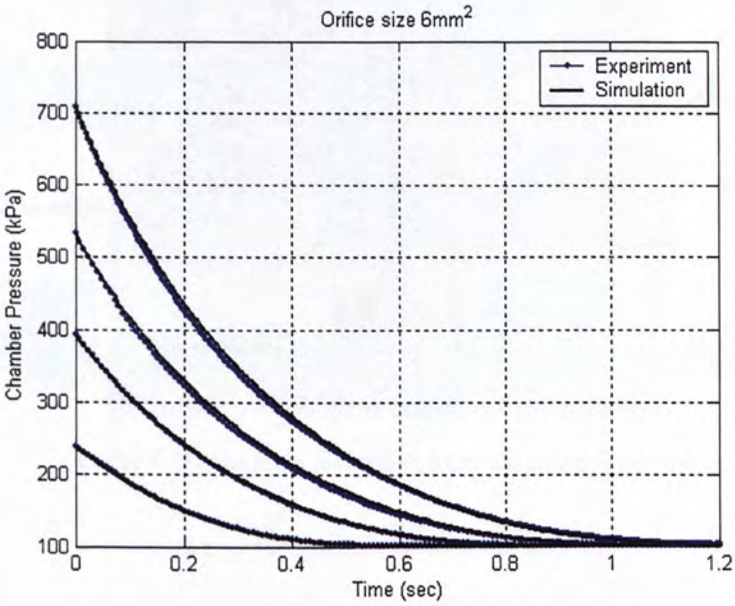

Figure 4-10) Simulation results for estimating the chamber pressure

4.2.5 Validation for Discharging to a Fixed Volume

This part aims to validate Equation (B.2.9).

Experimental Setup

Figure 4-11 shows the experimental setup. The smaller chamber initially trapped air at certain pressure and then discharged to the larger chamber with different outlet orifices. The outlet orifices were SMC fittings KQH04-02S (effective area of 6.38mm^2) and KQH06-03S (effective area of 15.21mm^2). Both of them can be treated as square-edged orifices. Since the effective area does not vary a lot with the pressure ratio [27], the effective areas of them are treated as constants in computation. Figure 4-12 shows the pressure sensor outputs for different outlet orifice at the larger chamber.

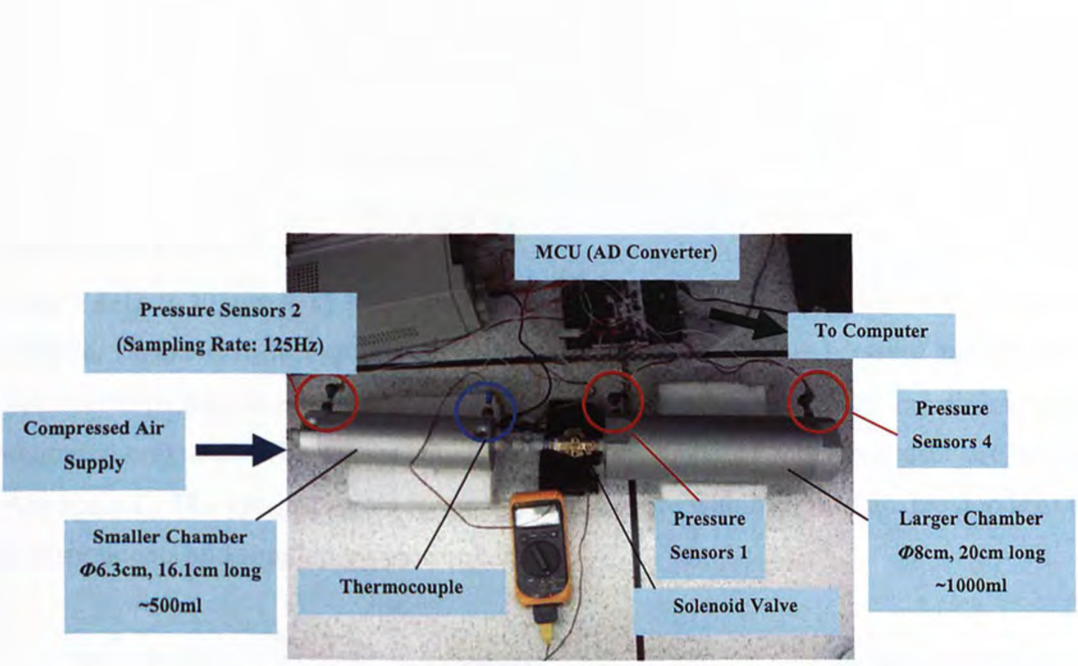

Figure 4-11) The setup for obtaining data for charging process

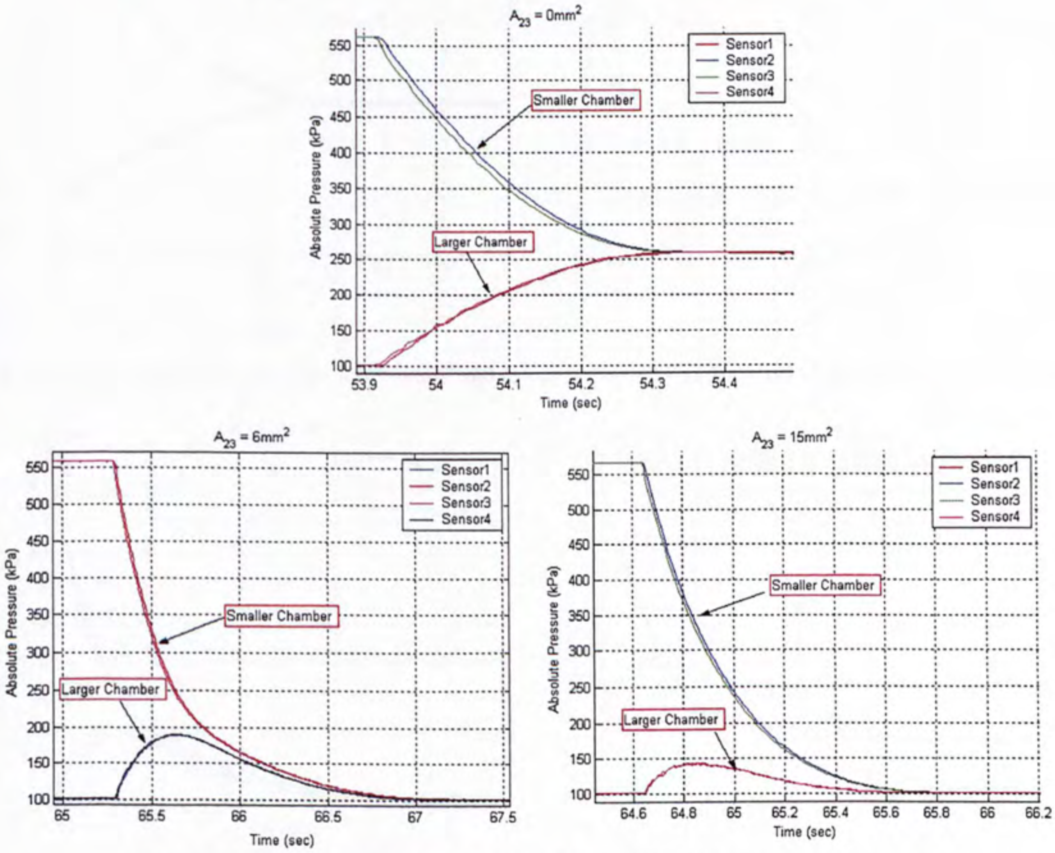

Figure 4-12) Pressure sensor outputs for different leakage hole at larger chamber

Simulation Result

Figure 4-13 to Figure 4-15 show the results for different outlet orifices at initial pressure of 550kPa. Figure 4-16 to Figure 4-18 compare the peak of chamber pressure and the time to peak between measurements and simulations for different outlet orifices and different initial chamber pressures. The means and standard derivations of measured data are listed in Appendix D. The greatest errors for both parameters are within 10%. Also, the trends of both measurements and simulations are similar.

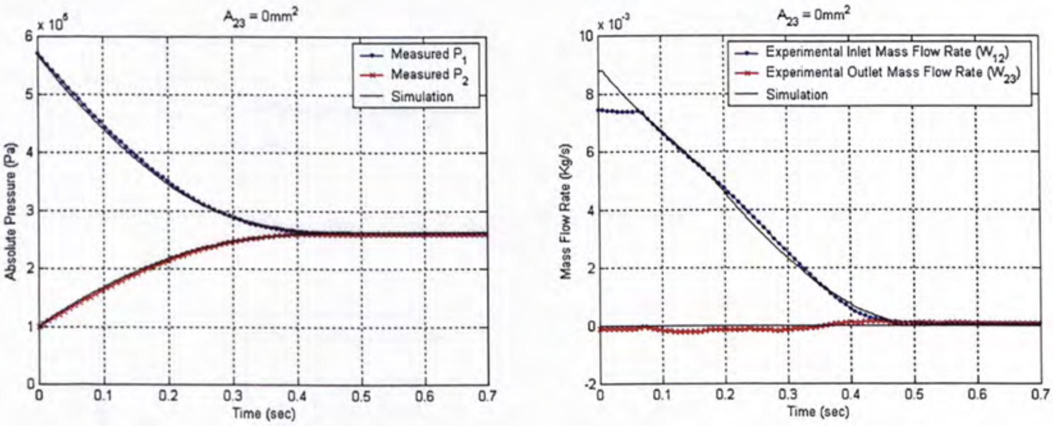

(a) (b)

Figure 4-13) Simulation results for A_{23} = 0mm^2 and initial pressure of 550kPa: (a) pressures; (b) mass flow rates

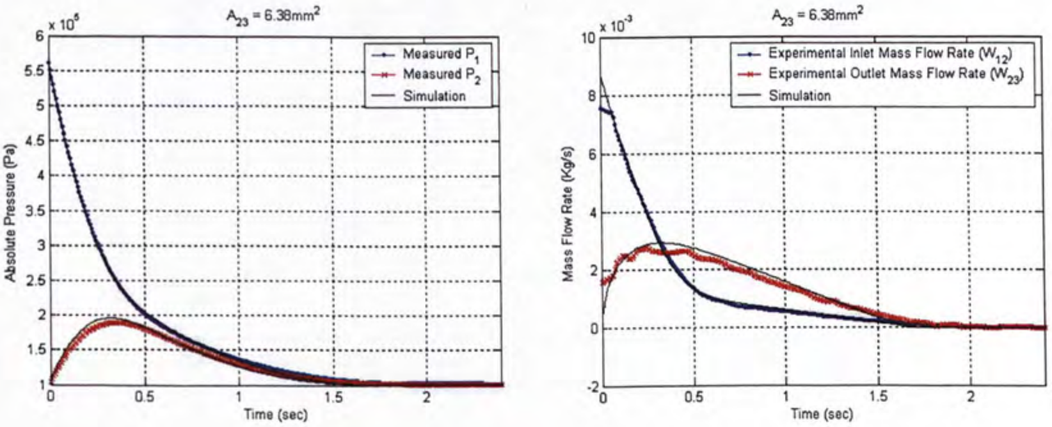

(a) (b)

Figure 4-14) Simulation results for $A_{23} = 6.38mm^2$ and initial pressure of 550kPa: (a) pressures; (b) mass flow rates

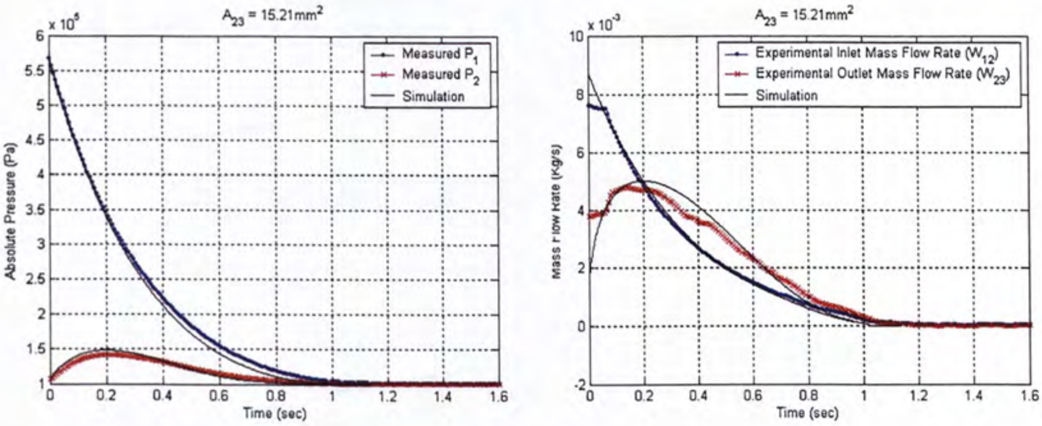

(a) (b)

Figure 4-15) Simulation results for $A_{23} = 15.21mm^2$ and initial pressure of 550kPa: (a) pressures; (b) mass flow rates

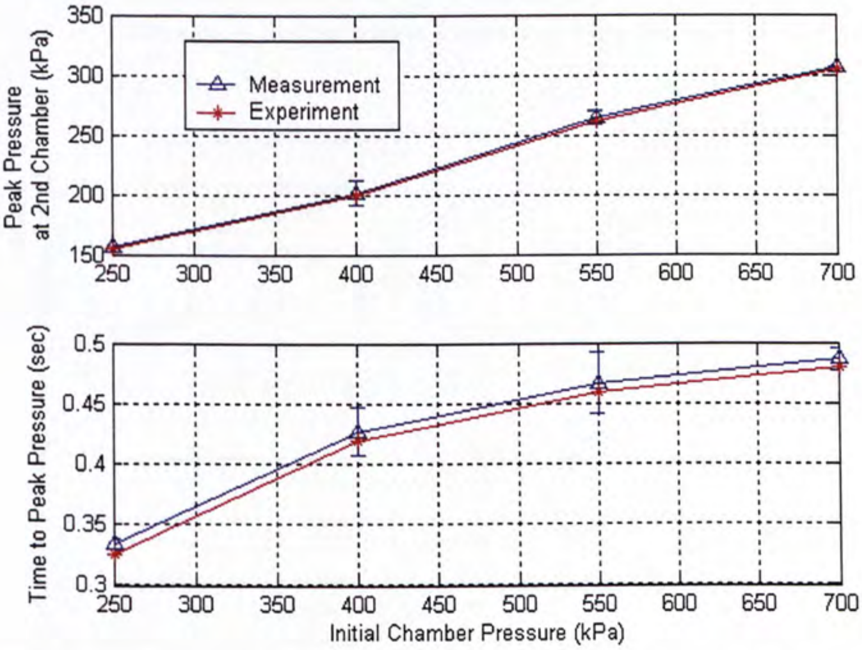

Figure 4-16) The comparison of experimental values and simulation results for $A_{23} = 0mm^2$

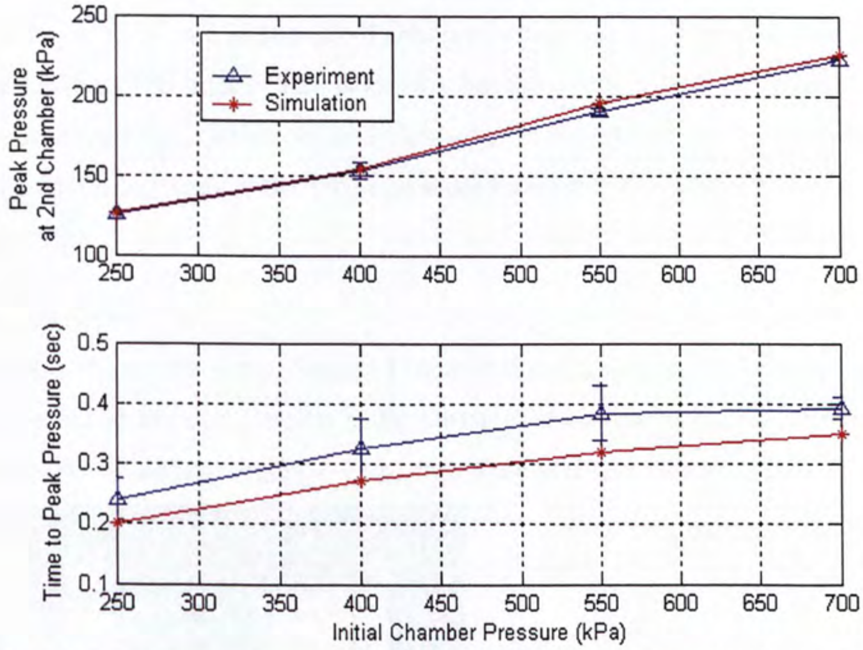

Figure 4-17) The comparison of experimental values and simulation results for $A_{23} = 6.38\text{mm}^2$

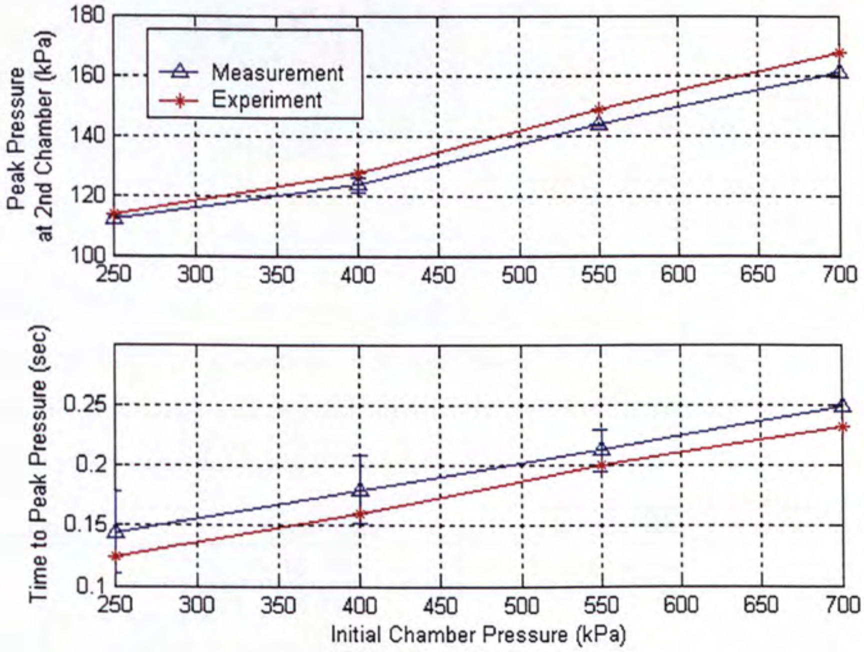

Figure 4-18) The comparison of experimental values and simulation results for $A_{23} = 15.21\text{mm}^2$

4.2.6 Estimation of the Size of Airbag's Leakage Hole

The airbag is modeled as a pneumatic diaphragm which has a variable volume and one inlet and outlet orifices. The inlet orifice is known, but the outlet orifice which has an equivalent size to the leakage hole is unknown and varies during expansion. The leakage mainly occurs at the seam which becomes wider when pressure increases. This part aims to find the size of the outlet orifice.

Experimental Setup

Figure 4-19(a) shows the setup. Sensor 1 measured the upstream total pressure of chamber, Sensor 3 measured the downstream static pressure of chamber and Sensor 4 measured the total pressure of the airbag. Figure 4-19(b) shows the pressure sensor outputs.

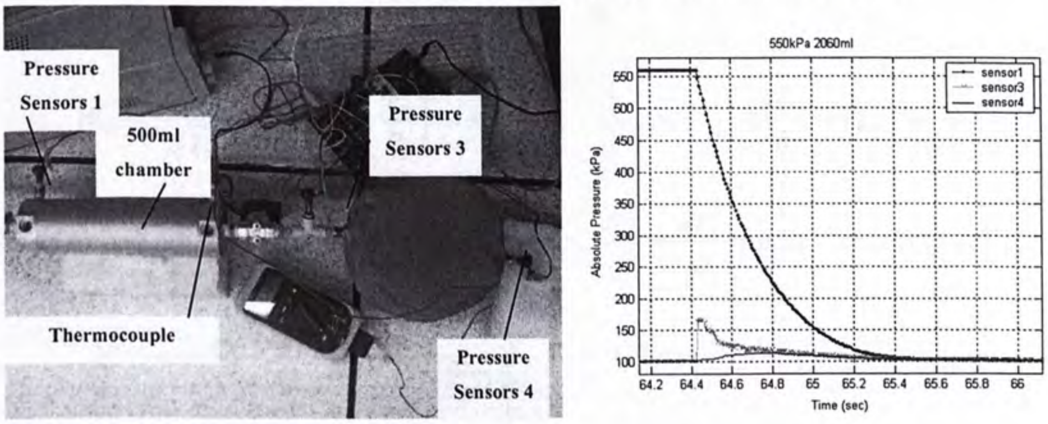

(a) (b)

Figure 4-19) (a) Setup for obtaining data to find the size of airbag leakage hole; (b) sensors' outputs

Three airbags of different volumes are used (see Table 1). The airbags were initial be inflated to nearly 80-90% of its maximum size and the pressure inside was kept as atmospheric pressure before discharging. The pressure sensors' outputs are substituted into the equation to solve out the value of outlet orifice area (A_{23}).

Airbag	Diameter	Thickness	Volume
1	18.7cm	7.5cm	2059.8ml
2	18.5cm	9.5cm	2553.6ml
3	18.5cm	12cm	3225.6ml

Table 1) The dimensions of airbags

Since the airbags were not initially at its maximum volume, they continued to expand during discharge of chamber. This leads to overestimation of W_{23} and hence the value of A_{23}. In the contrast, the airbags started to deflate after the maximum pressure was reached. This leads to underestimation of value of A_{23}. However, the seam was widest at the airbag pressure was maximum due to largest tensile force. There was no effect of volume change at this point. Thus, the exact maximum value of A_{23} can be found at here. It is assumed that the value of A_{23} depends on airbag pressure. The maximum value of A_{23} is plotted against the different maximum airbag pressure to get the A_{23} - P_2 relationship.

Recall the airbag volume-pressure relationship, Equation (B.2.6):

$$\frac{V_2}{nRT_2}\frac{dP_2}{dt} = -\frac{P_2}{RT_2}\frac{dV_2}{dt} + W_{12} - W_{23}$$

$$W_{23} = \frac{A_{23}P_2}{\sqrt{T_2}}\left\{\frac{2\gamma}{R(\gamma-1)}\left[\left(\frac{P_3}{P_2}\right)^{2/\gamma} - \left(\frac{P_3}{P_2}\right)^{\gamma+1/\gamma}\right]\right\}^{1/2} = -\frac{P_2}{RT_2}\frac{dV_2}{dt} + W_{12} - \frac{V_2}{nRT_2}\frac{dP_2}{dt}$$

When airbag pressure attains its maximum value, $\frac{dP_2}{dt} = \frac{dV_2}{dt} = 0$ and hence $W_{23} = W_{12}$.

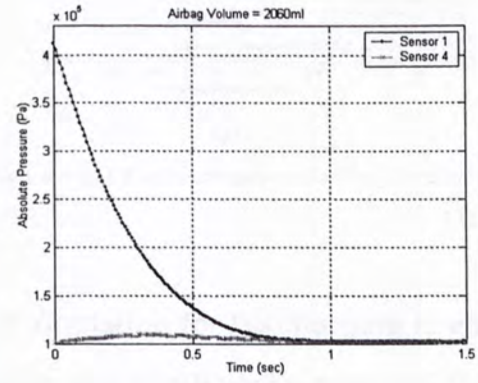

(a)

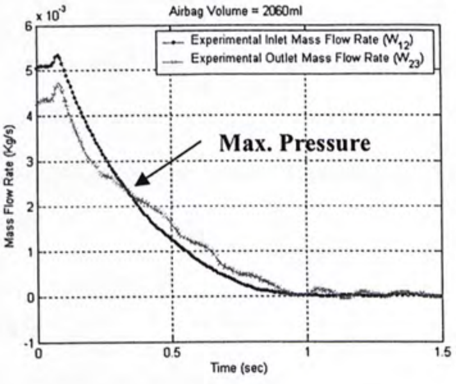

(b)

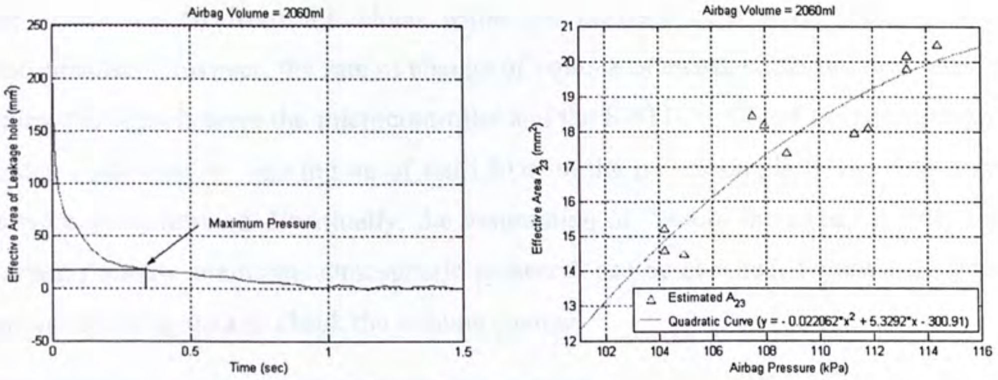

(c) (d)

Figure 4-20) (a) The pressure data for initial chamber pressure of ~400kPa and 2060ml airbag; (b) The mass flow rates determined from the pressure data; (c) the maximum value A_{23} determined at maximum airbag pressure; (d) The maximum value of A_{23} against maximum airbag pressure

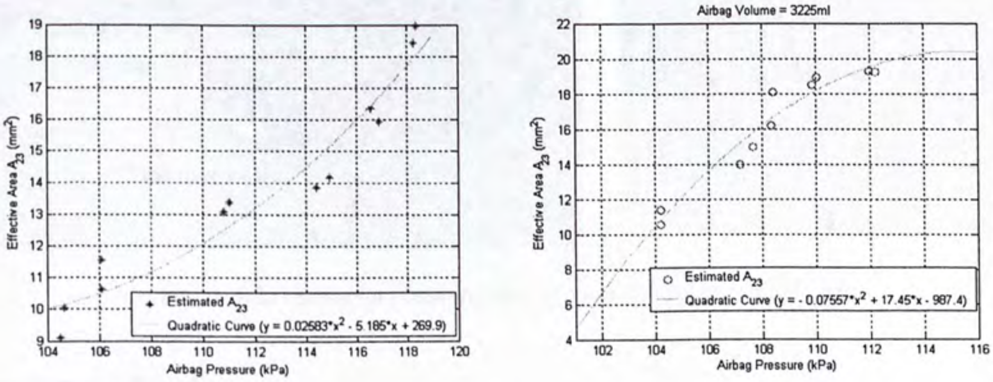

(a) (b)

Figure 4-21) The maximum value of A_{23} against maximum airbag pressure: (a) for 2553ml airbag; (b) for 3225ml airbag.

4.2.7 Validation for Discharging to an Airbag

This part aims to validate Equation (B.2.8) together with Equation (B.2.9).

Experimental Setup

Besides the pressure sensors, a signal from power supplier was also connected to the microcontroller to indicate the switch on of the power supplier. A digital camera (frame rate of about 30Hz) was used to capture the inflation process. The time taken for expanding the airbag was obtained from the video while the pressure data were obtained from the microcontroller. However, the rate of change of volume of airbag could not be evaluated. By checking the signals from the microcontroller and the SWITCH-ON of the power supplier in the video (indicated by lighting up of red LEDs on the power supplier), the data from both sides were synchronized. Eventually, the assumption of "before the airbag is fully inflated, the airbag pressure maintains atmospheric pressure" can be checked. Figure 4-22 shows the setup for obtaining data to check the volume change.

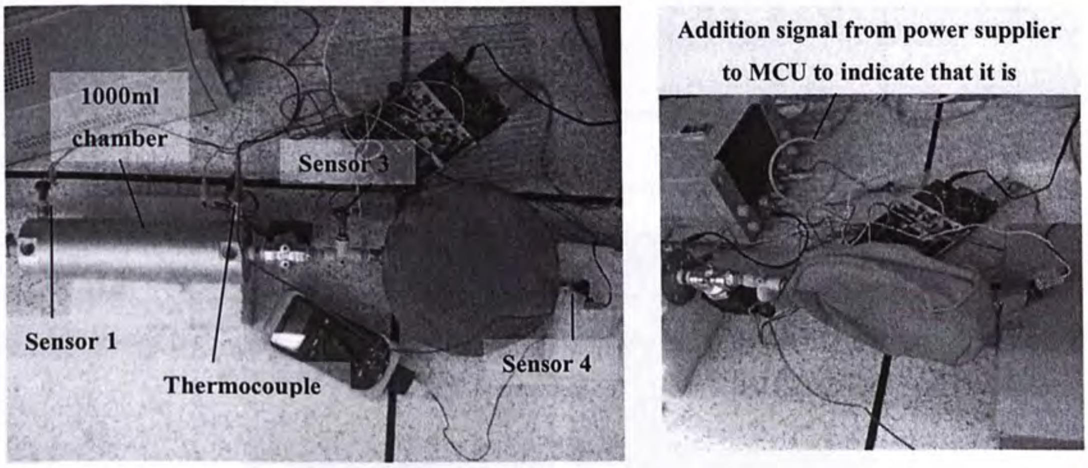

Figure 4-22) Setup for obtaining data to check the volume change part

Experimental Result

The volume of airbag is measured at its maximum size. Figure 4-23 shows the pressure sensor outputs for initial chamber pressure of ~400kPa and airbag volume of 2060ml. The events occurred at time moments on the pressure data in Figure 4-23 match with the corresponding images shown as Figure 4-24: (a) 36.42s (0s)→ switch on power supplier; (b) 36.608s (0.188s)→ sensors detect the flow; (c) 37.04s (0.62s)→ airbag pressure starts to expand; (d) 37.65s (1.23s)→ airbag pressure attains maximum. From the results below, the airbag pressure starts to rise up at the volume attaining about 80-90% of its maximum size. This is due to the tension of airbag membrane.

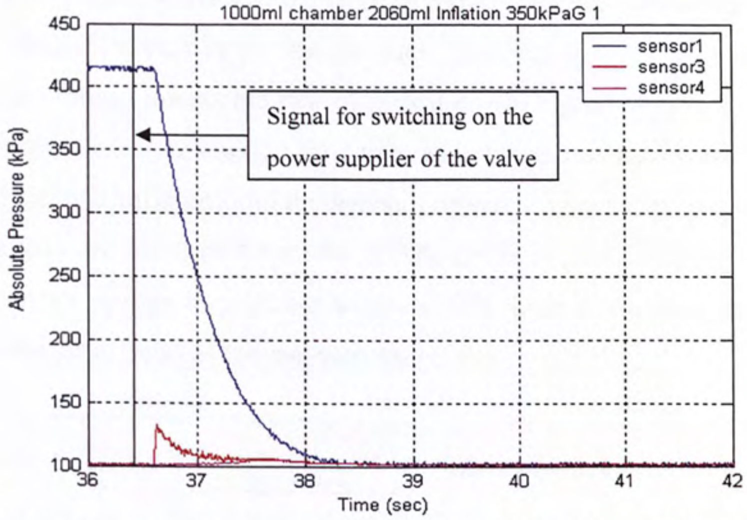

Figure 4-23) Sensors' outputs for initial chamber pressure of ~400kPa and airbag volume of 2060ml

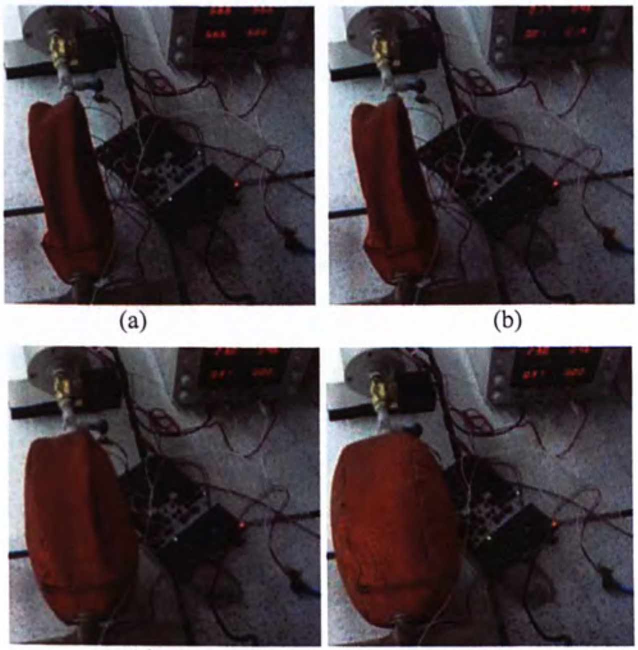

Figure 4-24) The images captured from video corresponding to the specified time moments

Simulation

Assuming the airbag is fully expanded before airbag pressure starts to rise up. The simulated airbag pressure will almost start to rise later but reach its peak earlier, and the peak is higher than the measured one. Moreover, the slope of airbag pressure corresponding to rising region is larger in simulation than in the measurement (see Figure 4-25). It is because in real case the expanding volume lowers the rate of pressure rise. Figure 4-26 to Figure 4-28 compare the peak of airbag pressure and the time to peak between measurements and simulations for different airbags and different initial chamber pressures. The means and standard derivations of measured data are listed in Appendix D. The errors in peak of airbag pressure are within 5% and the errors in time to peak are within 13.7%. Despite of some errors, the simulation results have the same trend as the measurements.

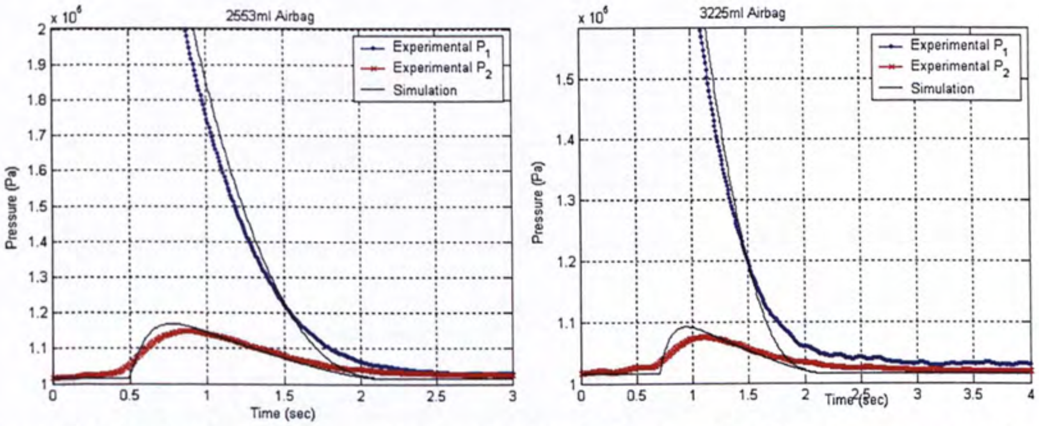

Figure 4-25) Simulated results for assuming that the airbag is fully expanded before pressure starts to rise up

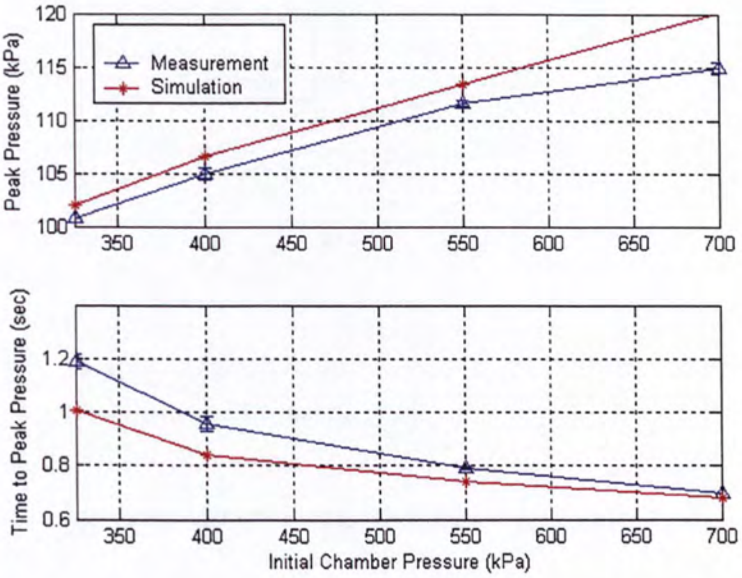

Figure 4-26) The comparison of experimental values and simulation results for 2060ml airbag

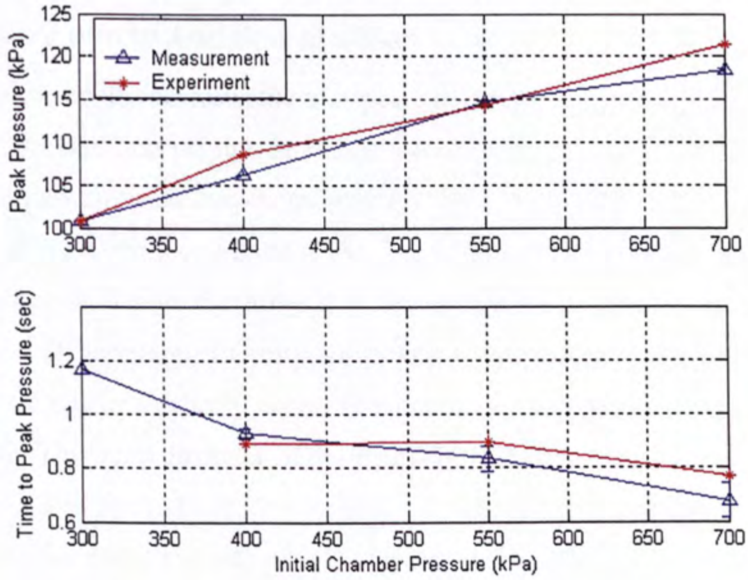

Figure 4-27) The comparison of experimental values and simulation results for 2553ml airbag. (The value for simulation at initial chamber pressure of 300kPa is undetermined as there is no peak in the simulated airbag pressure)

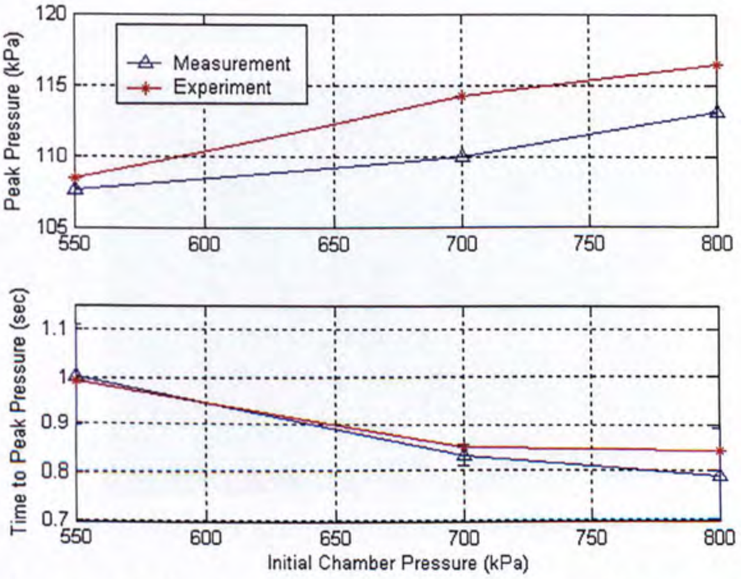

Figure 4-28) The comparison of experimental values and simulation results for 3225ml airbag. (The initial chamber pressure below 550kPa cannot fully inflate the airbag)

4.2.8 Time Delay due to Addition of a Pipe

The length of pipe length increases the transport time of gas from compressed cylinder to the airbag. In case the addition of pipe increases the inflation time and reduces pressure of the airbag, pipes of two different lengths (85mm and 340mm) were used to connect the inflator and the airbag of ~2550ml (see Figure 4-29). The length of 340mm pipe was long enough to connect the airbag at hip to the inflator at the stomach (of 35-inch waistline). From the statistical data of Department of Orthopaedics and Traumatology of CUHK, the mean waist circumstance of 69 elderly is only about 34 inches. Two measurements were conducted for each pipe length. The inner diameter of the pipe was 5mm. The pressure change first detected by sensor 1 indicated the start of flow as it is the closest to the orifice on the cylinder (see Figure 4-30(a)). The sampling rate of sensors was 250Hz. The airbag pressures (maximum value and time to peak) for these two pipe lengths are found to be almost the same (shown in Figure 4-30(b)). Therefore, it can be concluded that the flow velocity of gas from compressed cylinder is high enough to compensate the increment in the pipe length. Moreover, the pipe can be ignored in the following estimations.

Figure 4-29) The setup for measuring the airbag pressure inflated by the inflator

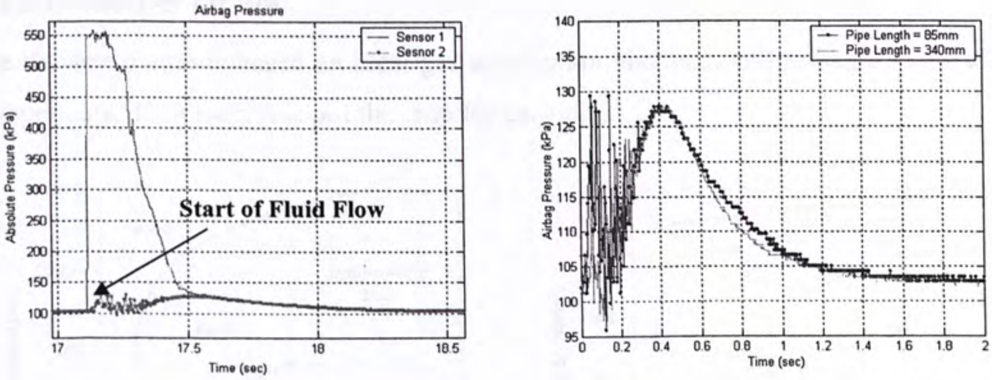

(a) (b)

Figure 4-30) (a) The pressures measured by the sensors. The pressure change first detected by sensor 1 indicates the start of flow as it is the closest to the orifice on the cylinder; (b) The comparison of airbag pressures with different pipe length

4.3 Summary of Experiments

Since the chambers have cylindrical shape, there are sudden changes in diameters from chambers to orifices. As a result, the actual bottle neck of the flow derivated from the physical dimension of orifice and there were vortices at the each of chamber. To have orifice sizes of 1.5mm^2 and 3.5mm^2, additional controlling valve was connected to the outlet of the solenoid valve. This further reduced the effective area (or the discharge coefficient). The mass flow rate equations required an adjustment (discharge coefficient) in orifice sizes in order to match the measurements. Moreover, the "orifices" of the valves are actually poppet valves which have discharge coefficients depending on pressure ratio; however, the orifices on the cartridges are square-edged which has a nearly constant discharge coefficient.

Besides, the discharge of CO_2 from cartridge is an adiabatic process. But due to the limitation of equipment, compressed air was used instead of CO_2 and the maximum pressure attained in experiments was about 850kPa. The resulted flows in experiments were isothermal. Thus, the experiments could only show that the equations could describe the isothermal flow for air.

4.4 Limitation of Model

Since the simulation is based on ideal gas assumption, the mass and pressure in the chamber are dependent. However, it is not the case for cartridge.

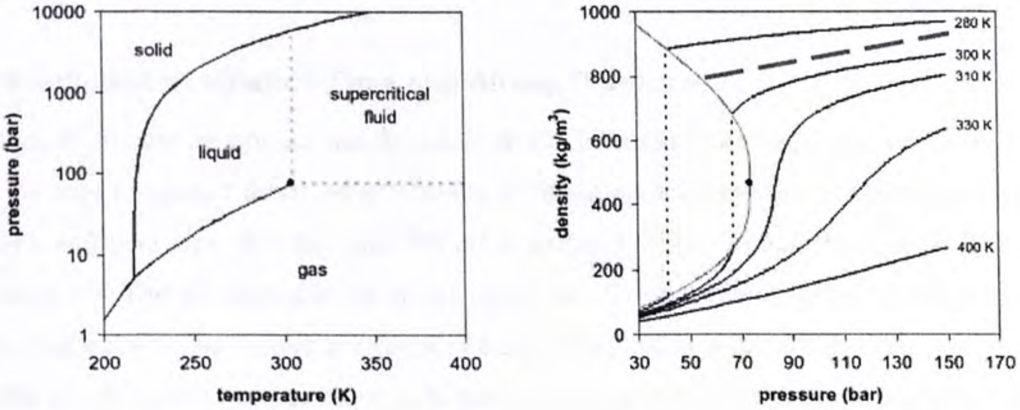

(a) (b)

Figure 4-31) (a) Carbon dioxide pressure-temperature phase diagram; (b) Carbon dioxide density-pressure phase diagram. (Extracted from [28])

The manufacturer of the cartridge claimed that the pressure inside is about 70bars. The temperature of the gas inside is at ambient temperature (about 20°C or 293K) before discharge. From the CO_2 pressure-temperature phase diagram (Figure 4-31(a)), there is a mixture of gas and liquid CO_2 inside the cylinder. From the CO_2 density-pressure phase diagram (Figure 4-31(b)), the density of the CO_2 liquid is around 750kg/m^3 (as indicated by the long dashed line) at 70bars and 293K. This density value gives a mass of liquid CO_2 of 11.25g in the volume of the compressed gas cylinder, $15x10^{-6}m^3$. The mass of liquid CO_2 matches the mass of CO_2 inside the cylinder claimed by the manufacturer. Therefore, it's possible that all the CO_2 is liquid.

To determine whether the CO_2 is compressed liquid or saturated mixture, we can also consider the saturation temperature at the given pressure 70bars. The saturation temperature at this pressure is about 29°C which is larger the initial storing temperature of the cylinder of 20°C. Therefore, the CO_2 is compressed liquid.

Even though the CO_2 immediately vaporizes and discharges as saturated gas from the cartridge, it has a larger variation from ideal gas law because of high pressure and low temperature. Thus, another mass flow rate equation is required to describe the flow of saturated CO_2. Besides, the pressure inside the cartridge during discharge cannot be related to mass by ideal gas law.

4.5 Prediction of Inflation Time and Airbag Pressure

Though the model cannot accurately represent the inflation of airbag by the cartridge, it can still be used to predict the trend of varying different parameters such as orifice size, airbag volume and vent size. But this time the air is replaced with CO_2 and the specific heat ratio becomes 1.3. The inflation process is considered as adiabatic. Knowing the inflation time and airbag pressure by the current prototype, we can determine how large the orifice and the ratio of vent size to orifice size are required to obtain the required airbag pressure and volume.

4.5.1 Effects of Orifice Size and Vent Size on Airbag Pressure and Volume

The peak pressure and the time to fully expand airbag depend on the pressure inside the cartridge. However, the cartridge pressure is unknown. Thus, the possible values of 850kPa and 7MPa are respectively taken to be the lower and upper limit of the pressure inside the cartridge. These values give the range of change in time to expand airbag resulted from the change of orifice size, airbag volume and vent size.

Figure 4-32 shows the increment of time to fully expand the airbag due to the increment of airbag volume, at orifice diameter of 1.4mm and vent size of 19mm^2. Figure 4-33 shows the decrement of time required to fully expand the airbag due to the increment of orifice size.

From the prediction in Section 5.4.2, a minimum pressure equal to atmospheric pressure and a volume of 1881.62ml are required for one airbag. Since two airbags are deployed, the total volume of 3763.24ml is needed. The vent size is double (38mm^2). From Figure 4-30(b), the maximum airbag pressure is 125kPa for volume of ~2550ml if 12g CO_2 cartridge is used and orifice diameter is 1.4mm. Consider the lower limit of cartridge pressure first. If volume increased by 1.48 times to 3763.24ml and vent size is double, the time to fully expand the airbag increase to 0.2sx2.24 = 0.448s (0.581s if response time of actuator is included). From Figure 4-33, the orifice size needs to be increased twice in order to have a total inflation time of 0.357s. Then consider the upper limit of cartridge pressure. If volume increased by 1.48 times and vent size is double, the time to fully expand the airbag increase to 0.2sx1.5 = 0.3s. And the orifice size needs to be increased by 1.5 times to have a total inflation time of 0.331s. With this increment of orifice size (1.5-2 times), the inflator theoretically can inflate two airbags, each of 1881.62ml to above atmospheric pressure around 0.32s.

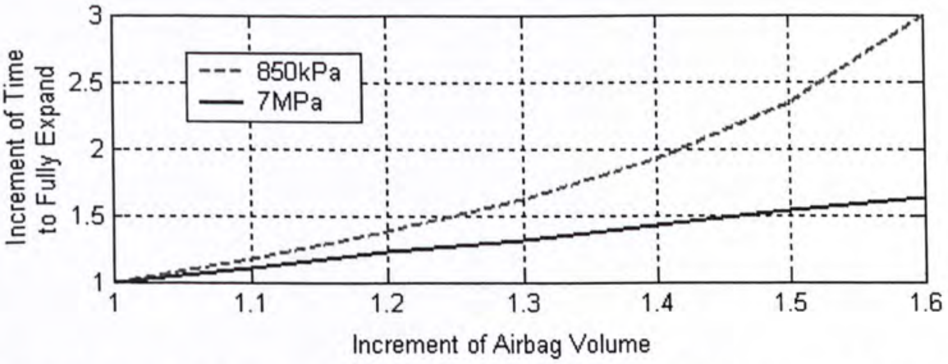

Figure 4-32) A plot of the Increment of time to fully expand the airbag vs. the increment of airbag volume, at constant orifice and vent sizes

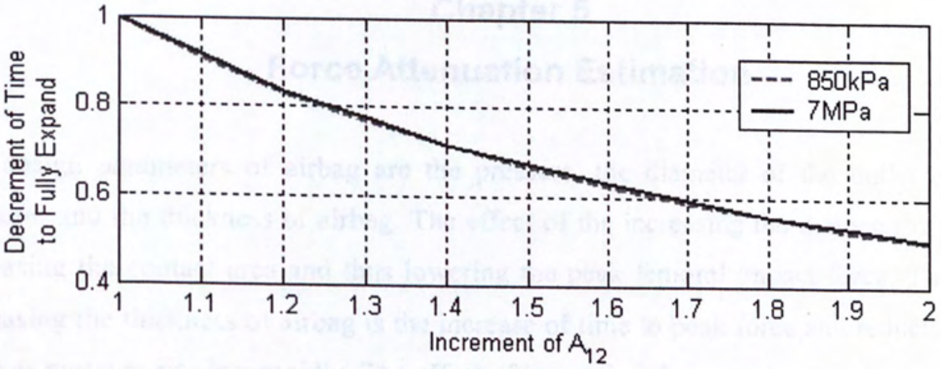

Figure 4-33) A plot of the decrement of time required to fully expand the airbag vs. the increment of orifice size

Chapter 5
Force Attenuation Estimation

The design parameters of airbag are the pressure, the diameter of the outlet orifice, the diameter and the thickness of airbag. The effect of the increasing the diameter of airbag are increasing the contact area and thus lowering the peak femoral impact force. The effect of increasing the thickness of airbag is the increase of time to peak force and reduction of peak force as pressure rise less rapidly. The effect of increasing the vent size is reducing the rate of pressure rise due to collapse of airbag. If it is too large, the airbag pressure will drop too rapidly and there will not be enough 'braking force' acting on the mass.

A simple damped spring mass model is used to predict the values of these parameters that are possible to attenuate the femoral impact force below the hip fracture threshold (3100±1200N) [11]. The threshold is a force value that is dependent on the bone density and the size of the hip joints. However, the moment at femur shaft that causes fracture cannot be evaluated. To make the airbag as robust as possible, the airbag is designed to keep hip impact below the lower quartile 1900N. The targeted users are the elderly of total mass about 51kg which is the mean value of the high risk group in Hong Kong. Simulation shows that a human of an effective mass of 25.5kg (one half of the total mass [30], [31]) with an impact velocity of 3.6m/s (which is the maximum estimated impact velocity of lateral fall from [30]) gives a peak impact force of 4.14 kN.

5.1 Theory and Model

The impact of hip joint is a step response [31][32]. The hip joint is considered as a mass attaching a layer of soft tissue. The mass is the effective moving mass around the hip joint and the soft tissue is represented by spring and dashpot. The spring stores part of the impact energy while the dashpot dissipates part of the impact energy. The remaining force acting on the effective mass is the femoral impact force. There are different arrangements of spring and dashpot. Robinovitch et al. [31] compared the accuracy of four different spring-mass models:

undamped mass-spring model; Kelvin-Voigt model; Maxwell support; and standard linear solid support model. All models underestimate the times to peak force. Kelvin-Voigt model and standard linear solid support model are tried to predict the impact forces (see Figure 5-1). The mean errors in peak force for these two models are -10.2±13.3% and 3.2±14% respectively [31]; the mean errors in time to peak force are -31.2±6.5% and -20.6±7.5% respectively [31]. Both characteristics are important in comparison with experimental data as there may be more than one combination of magnitudes of spring constant and damping coefficient that give the same peak force.

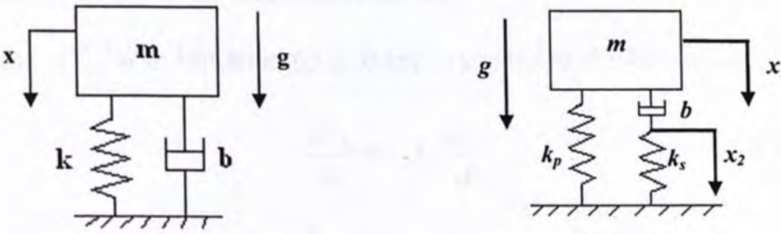

(a) (b)

Figure 5-1) (a) Kelvin-Voigt model; (b) Standard linear solid support model

5.1.1 Kelvin-Voigt Model

There are a spring and a dashpot in parallel in the Kelvin-Voigt model. The shortcoming of this model is that if the system is subjected to an initial velocity, the force is instantaneously transmitted to the mass due to the dashpot. This characteristic does not happen in reality [36].

5.1.2 Standard Linear Solid Support Model

An additional spring in series to the dashpot forms the standard linear solid support model. The model does not have the problem of instantaneously force due to initial velocity. However, its closed form solution is more complicated [31]. With the use of Matlab Simulink, the model replaces the use of previous model.

The airbag is considered as a spring of variable stiffness depending on the pressure inside and the stiffness of the airbag material. It is connected at the bottom of the standard linear solid support model (see Figure 5-2). Meanwhile, the pressure inside the airbag is evaluated simultaneously with the pressure change equation (B.2.6). The pressure is assumed to be constant over the volume. The equations of motion are the following:

$$m\ddot{x}_1 + c(\dot{x}_1 - \dot{x}_2) + k_p(x_1 - x_3) = mg \qquad (5.1\text{-}1)$$

$$c(\dot{x}_2 - \dot{x}_1) + k_s(x_2 - x_3) = 0 \qquad (5.1\text{-}2)$$

$$k_p(x_1 - x_3) + k_s(x_2 - x_3) = P_a A_{contact} \qquad (5.1\text{-}3)$$

where P_a is the gage pressure inside the airbag (in Pa) and $A_{contact}$ is the contact area (in m^2) which is taken as 1cm times the diameter of airbag.

The terms V_2 and dV_2/dt in Equation (B.2.6) are evaluated as the following:

$$\frac{dV_2}{dt} = -A_a \frac{dx_3}{dt} \qquad (5.1\text{-}4)$$

$$V_2 = (h - x_3)A_a \qquad (5.1\text{-}5)$$

where h is the initial thickness of airbag (in m) and A_a is the airbag upper surface area (in m^2).

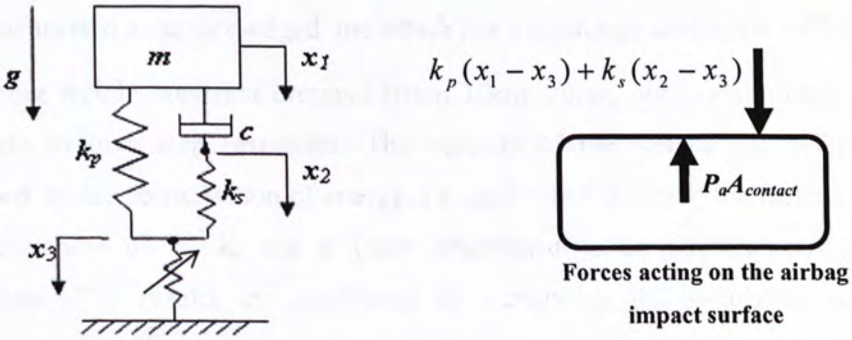

Figure 5-2) The model to simulate the femoral impact force with airbag consists of a standard linear solid support model and a variable spring constant

The hip fracture threshold is a point force acting on the center of hip. The term $P_aA_{contact}$, which is proportional to the impact force, is the resultant pressure force acting at the center of the contact area. The model here will give a higher peak impact force (*Peak'*) as the contact area is larger than the hip region. Assume that the airbag pressure acts evenly on the contact area. The 'actual' peak impact force acting on the hip equals:

$$Peak_{actual} = Peak^{'} A_{hip} / A_{contact} \qquad (5.1\text{-}6)$$

where A_{hip} is the area of hip region, taken as $\pi/4 \times 11^2$=95.03cm^2.This region corresponds to the stiffest region at hip [34]. The stiffness at the circumference is less than one half of the center (the femoral head).

5.2 Simple Testing for Validation

To check the correctness of the model, a training weight fell freely from a known height to produce loading on a cylindrical airbag. A Kistler force plate (model 9285) was placed under the airbag to measure the impact force. The dimensions of the airbag were 18.5cm diameter and 10cm thickness. In other words, the training weight had an initial velocity before impact with the airbag. The training weight was represented by the standard linear solid support. The parameters of the training weight were: 1) mass of 5.018kg; 2) (flat) impact surface area of 12x15cm^2; 3) main outlet orifice of 12.7mm diameter. The impact surface area of the training weight was closed to that of the airbag to produce an even loading on the airbag. The outlet orifice was treated as square-edged one which has a discharge coefficient of 0.82.

The training weight was first dropped (from 10cm, 20cm, 40cm and 60cm) directly to the force plate to give step responses. The velocity of the weight just before impact was determined by the conservation of energy, i.e. $mgh = mv^2/2$. Using the method introduced by [19], the values of k_p, k_s and c were determined to be 60.5kN/m, 406.98kN/m and 791.51Ns/m. The results are confirmed by comparing the simulation results and the measurements (see Figure 5-3 and Figure 5-4). The errors are within -15% and 2%.

Then the airbag was supplied with compressed air continuously and placed on the force plate. The pressure inside the airbag was measured and three absolute pressure levels: 102.11kPa, 102.93kPa and 104.15kPa. The weight was dropped at the distances, 10cm, 20cm and 40cm, from the airbag sequentially. It was dropped for three times under the same condition. The step responses with the airbag are obtained and compared with the simulation results (see

Figure 5-5). The times to peak force are underestimated in simulations. Figure 5-6 compares all the measurements and the simulation results at different airbag pressures. The errors are due to the changing contact area in reality and the omission of the resistant force from airbag membrane. However, the contact area is treated as a constant in simulations. The means and standard derivations of measured data are listed in Appendix D. The errors observed range from -3.23% to 13.67%, which are within one standard derivation of error provided from another study [31].

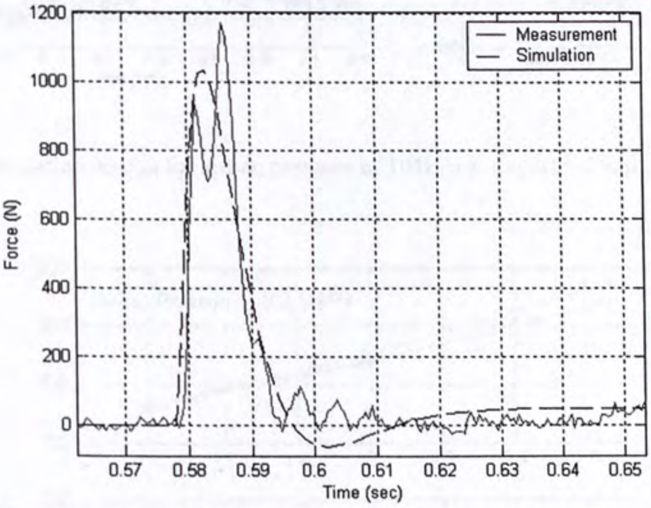

Figure 5-3) The simulation result of the Simulink model for standard linear solid support: the dropping height is 10cm and the impact velocity is 1.4m/s. The simulation result is differenced from the measurement by -10.5%.

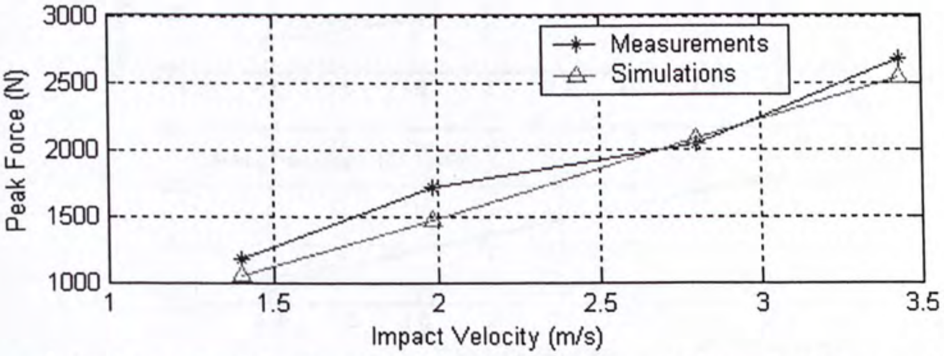

Figure 5-4) Other results of the Simulink model for standard linear solid support: the impact velocities are 1.4m/s, 1.98m/s, 2.80m/s and 3.43m/s (dropping from 10cm, 20cm, 40cm and 60cm respectively). The simulation results are differenced from the measurements by -10.51%, -14.32%, and 1.78% and -5.27% respectively.

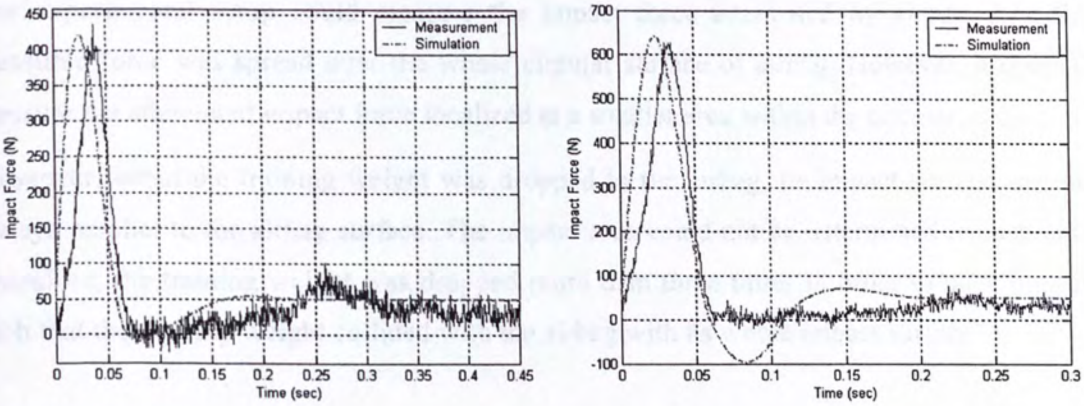

(a) (b)

Figure 5-5) Simulation results for airbag pressure of 104kPa at impact velocities: (a) 1.98m/s; (b) 2.80m/s

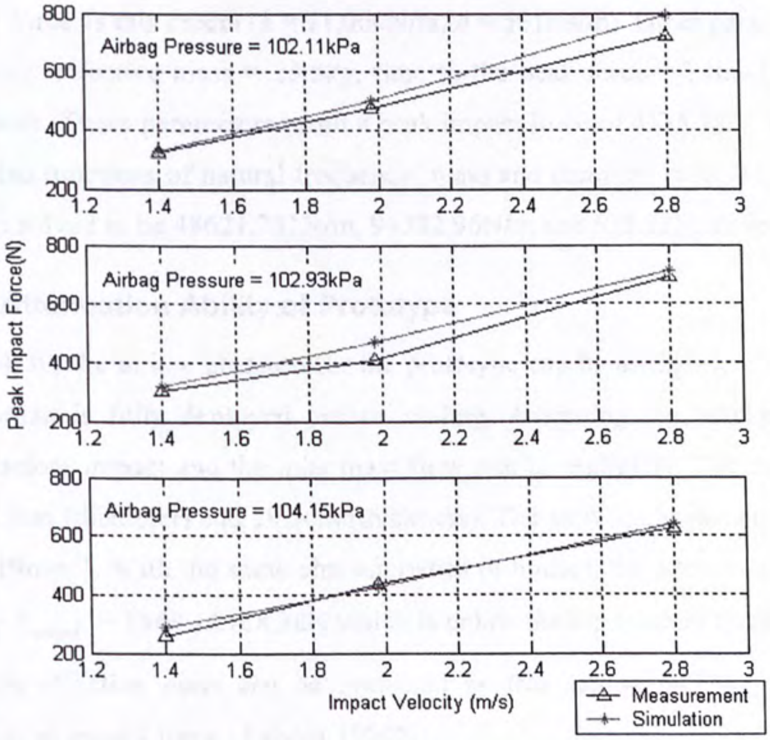

Figure 5-6) Comparison of simulation results with measurements at different airbag pressures

5.3 Summary of Experiment

The experimental setup could measure the impact force attenuated by airbag. And this measured force was spread over the whole circular surface of airbag. However, it couldn't measure the attenuated impact force localized at a smaller area within the circular surface.

Moreover, when the training weight was dropped to the airbag, its impact surface was not always parallel to the airbag surface. The impact area could not be determined in such case. Therefore, the training weight was dropped more than three times in order to have impacts such that the training weight collided with the airbag with its whole impact surface.

5.4 Estimation

Since Robinovitch [32] used Kelvin-Voigt model to describe the stiffness and damping factor at hip region of young women, it is necessary to find a set of k_p, k_s and c such that they give the same peak force as this model ($k = 71{,}060$N/m, $b = 561$Ns/m). Other parameters are taken as the following: effective mass = 25.5kg, time to the peak force = 21ms [32] and impact velocity = 3.6m/s. These parameters result a peak impact force of 4135.78N. The values of k_p, k_s and c are also functions of natural frequency, mass and damping ratio [31]. The values of k_p, k_s and c are solved to be 48621.701N/m, 96392.96N/m and 625.22Ns/m respectively.

5.4.1 Force Attenuation Ability of Prototype

From Figure 4-30, the airbag pressure for the prototype can be as high as 125kPa. From the figure, the airbag is fully deployed before landing. Assuming the maximum pressure is attained just before impact and the inlet mass flow rate is negligible. The dimensions of the airbag are 18.5cm (diameter) and 10.5cm (thickness). The vent size is just equal to the size of seam (about 19mm^2). With the same characteristics of human, the attenuated impact force is 3103Nx $A_{hip}/A_{contact}$ = 1449.1±188.38N which is below the hip fracture threshold.

The maximum effective mass can be protected by this setting is 39kg, which gives an estimated femoral impact force of about 1900N.

5.4.2 Minimum Airbag Volume and Pressure Required to Reduce the Force

Keeping the diameter of 18.5cm, the ratio $A_{hip}/A_{contact}$ is 0.467. The airbag at any gage pressure above zero can halve the femoral impact force provided that the thickness is large enough and the vent size is small enough. With the minimum pressure of 101.9kPa, the minimum thickness of 7cm and the vent size kept about 19mm^2, the peak femoral impact force is 3517.5N x $A_{hip}/A_{contact}$ =1642.67±224.5N. Therefore, with a vent size of 19mm^2, the minimum gage pressure required is the atmospheric pressure, and the minimum dimensions of airbag are 18.5cm diameter and 7cm thickness.

Chapter 6

Future Work

6.1 Impact Test for Airbag System

Due to humanity problem, human subject cannot be used to do any impact experiment. In biomechanical study, mechanical setups are used to mimic the hip joints of old women, e.g. P. Kannus [11] used a pendulum setup to compare the force attenuation ability of commercial hip protectors. Previously, a dummy was used in the impact test of this project. However, since the dummy has too many degrees of freedom, the impacts due to uncovered region made it impossible to determine the force attenuation ability of airbags. Therefore, the designs of impact pendulums from the projects are referred and introduced for this project. Some settings can be directly applied to our setup which reflects lateral falls.

The previous designs of impact pendulums surrogate both hip joint and pelvis [11][31]. Two load cells are installed at the impact face of pendulum and below the surrogate femur. The load cell at the pendulum measures the impact force exerted by the pendulum and another one measures the force transmitted to the femoral neck. The stiffness and damping of the pelvis is simulated with springs (P. Kannus [11] used four steel springs of stiffness 18.8kN/m each). The femur is made by steel [33] instead of wood because of its robustness. Since steel can transmit force better than wood, there is a lower opportunity that the peak force measured is lower than reality. The dimensions of femur set by Siegfried Derler [33] are: femoral head of diameter 4.5cm, shaft diameter of 2.7cm, neck-shaft angle of 127° and angle between shaft and horizontal line of 10°. As the contact area is an important factor of force attenuation for airbags, the surrogate femur is covered with a layer of polyethylene form which has the shape of the thigh. The layer of form also mimics stiffness and damping of the trochanteric soft tissue. S.N. Robinovitch [34] showed that the form can give a peak force and time to peak force nearly the same as cadaveric tissue. The thickness of the layer required is determined from experiments: dropping the pendulum with known impact velocity and determining the damping ratio and natural frequency from the step response; then evaluate the stiffness and damping coefficient with the Kelvin-Voigt model; repeat the steps until the required stiffness and damping coefficient are obtained.

The effective mass of pendulum is set to be 25.5kg; the impact velocity is adjusted to be 3.6m/s; and the stiffness and damping coefficient at hip is set to be 71kN/m and 561N-s/m respectively (refer to Kelvin-Voigt model) [31]. The whole surrogate hip joint is installed on the pendulum. The airbag is attached on the surrogate hip and is connected to a constant compressed gas supply. A force plate is placed at the same level of the impact location to measure the impact force before entering the femoral head. The whole setup is shown in Figure 6-1.

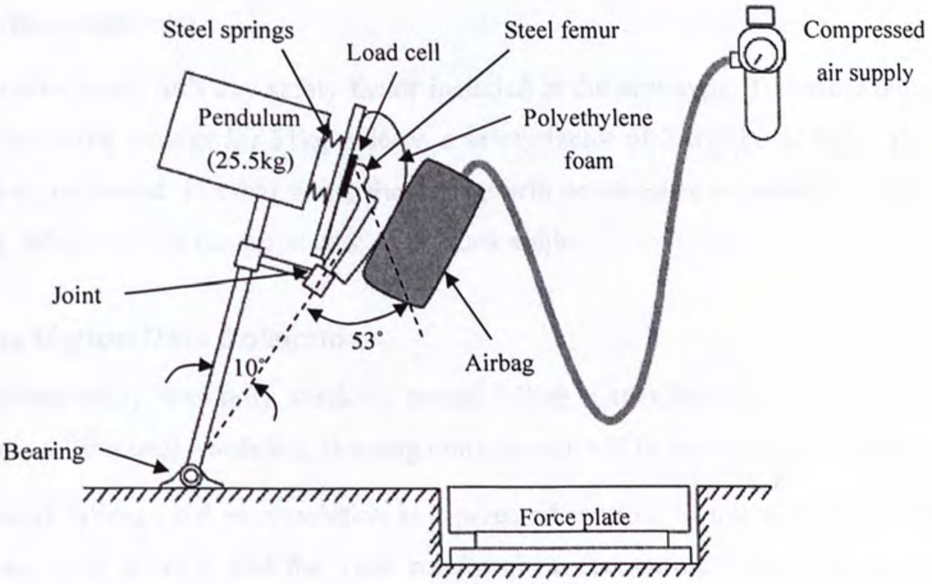

Figure 6-1) The inverted pendulum used to find the pressure and size of airbag required to attenuate the peak impact force to below the hip fracture threshold of 3100±1200N

6.2 The Effective Mass of the Target User

The current prototype pinpoints to the lateral fall of 51kg old lady without bending of trunk. However, according to Kroonenberg (1995) [35], when the trunk angle decreases, the effective mass and hip impact velocity increases in opposite, hence a larger impact force will be resulted. (The trunk angle is defined as the angle between the normal to the ground and the axis of trunk just before impact. For example, if the trunk is vertical to the ground during impact, the angle is 0°; if the trunk is parallel to the ground during impact, the angle is 90°.) In the falling test conducted by [30], all the subjects did not fall with a straight trunk. Their trunk angles instead had a mean of 21.7° and could be as low as 1.3°. Therefore, to make the airbag system more robust, a lower trunk angle should also be considered. Take the lowest trunk angle to be 0° as it results the largest effective mass. According to Zatsiorsky and Seluyanov [37], the mass distribution of body segments for a 51kg human is: head – 3.54kg; trunk together with hands – 27.2kg; thighs – 14.44kg; and shanks with feet – 5.82kg. When the old lady falls with 0° trunk angle, the thighs and other segments above the thighs contribute the effective mass. The maximum value of this effective mass equals 45.18kg (the sum of these segments).

Furthermore, there isn't any safety factor included in the prototype. To ensure the protecting capability of the airbags for 51kg elderly, a safety factor of 2 will be added to the effective mass to be protected. In other word, the airbags will be designed to protect an effective mass of 51kg, which covers the worst case of 0° trunk angle.

6.3 The Motion Data Collection

The current study was only stuck to lateral falling. Other falling motion such as falling forwards, falling backwards and sleeping onto ground will be studied in the future.

The lateral falling used in simulation is a prepared motion. In this motion, the shanks and thighs are kept straight, and the trunk rotates about feet before impact; on the other hand, sleeping onto ground is an unprepared fall. The shanks and thighs may bend during falling. As a result, the hip may land to the ground in a shorter time. The comparison of the actual falling times of these two motions hasn't been documented. Thus, the same subject needs to perform both falling motions to compare the falling times. It is important because the falling time restricts the period of inflation of airbags.

The motion data was collected from one person only throughout the study. However, the gaits of different persons are different. It is impossible for this SVM filter to accurately classify all the falling and non-falling motions of different elderly. To make the filter work for different elderly, motion data from different elderly are necessary and the sample size has to be as large as possible.

6.4 Modification in the Inflator

One modification is to add a mechanism to prevent false-triggering of inflator during replacement of cartridge. The idea is to add an extra lock at the spring chamber. The lock is attached with restoring springs (see Figure 6-2). When the screw for compressing spring is not completely installed, the lock will be pulled down by the restoring springs. In addition to the levers, the front end of the lock blocks the punch from launch. In the contrast, when the screw is completely installed, the end of the screw will push the rear end of the lock upwards. Meanwhile, the front end will also be lifted up and the punch is ready for launch.

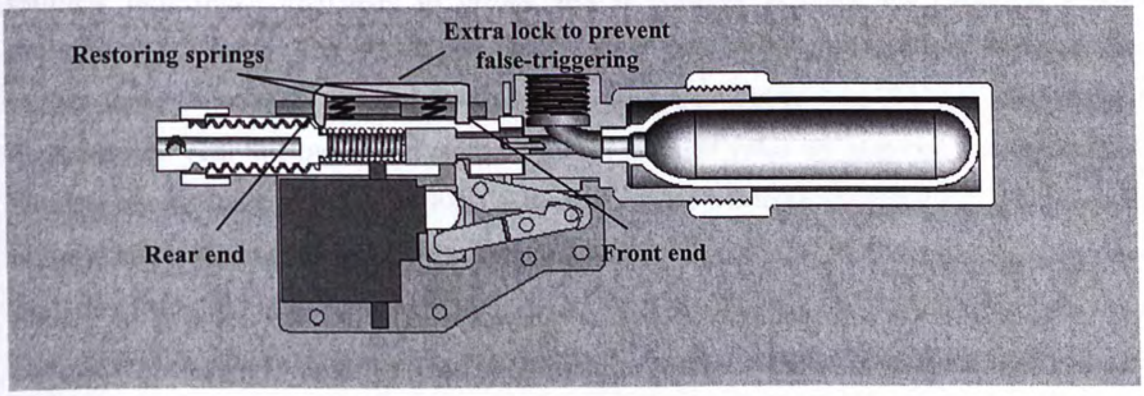

Figure 6-2) A mechanism added to prevent false-triggering of inflator during replacement of cartridge

Chapter 7
Conclusion

An inflator of a simple mechanism is built and tested. The inflator uses one 12g CO_2 cartridge to inflate a 2.5L airbag within 0.3s. By using a larger CO_2 cartridge (38g), two airbags of 2.8L can be inflated within 0.35s. It has also been connected to the sensing device and successfully be triggered by the sensing device in a sideway fall.

A standard linear solid support model is used to predict the pressure and airbag volume required to attenuate the impact force. The target users are 51kg elderly. The mass of 25.5kg, overall stiffness of 71kN/m and damping coefficient of 561N-s/m and impact velocity of 3.6m/s are used in the simulations. Moreover, a simple mathematical model is used to estimate how much increment of orifice size is required to attain the necessary airbag pressure and volume. The simulation results show that 1) the prototype can attenuate the impact force from 4135.78N to 1449.1N; 2) the minimum dimensions of airbags are 18.5cm diameter and 7cm thickness, and pressure just at ambient value are required to attenuate the femoral impact force to below 1900N; 3) the orifice size has to be increased by 1.5-2 times in order to attain the above airbag volume within 0.32s.

Finally, an inverted impact pendulum is proposed to test the force attenuation capacity of the airbags. The design is modified from the settings of previous designs from other researchers.

The current prototype is about 253g which is still too heavy to carry. A more acceptable weight is about that of a mobile phone (around 100g). This can be achieved by reducing the size of the inflator and replacing the copper parts with aluminum alloy. With the reduction in weight and size of the inflator, the airbag system will be small enough to place inside the pocket of the airbag system, just similar to place a mobile phone inside a pocket. Moreover, the airbag system will not need to wear with a tight undergarment. The elderly will feel more convenient and comfortable.

As mentioned in introduction, the nursing home residents are high risk group of hip fracture and they are highly dependent on the nursing home staff. They need the helps from staff to wear protectors. With the ease of wearing of airbag protectors, the staff will be more convenient on caring these elderly. For example, the stuff only needs to hook the airbag protector to the waist of the elderly and check if the location is correct or not. It's much easier to help the elderly wear an undergarment for hip protectors. Eventually, the staff will be more willing to help these elderly wear the airbag protectors. The compliance rate can be also increased in the community. Airbag protectors of belt pocket shape are more acceptable to the younger and easier for them to take care. With the encouragement and help from the younger family members, the elderly will be more likely to wear the airbag protectors.

The recent progress is just the first step of the "real" airbag protectors. The demonstration of human wearing integration system of μIMU and the inflator (Section 3.3.2) just provides evidence that a portable automated airbag system has potential for hip protection. Moreover, many dummy impact tests have been conducted and proven that airbags could reduce impact forces. Under the same principle, the airbag protector can also reduce the impact force. The remaining question is how large of both airbag size and pressure are required. Besides, it is an extremely challenge work to extend the classification power of the μIMU. Huge work on the collection and analysis of motion data from elderly is required. The sizing problem in hardware and the modification of μIMU performance will the next milestone of this research project. After the technology becoming mature, it can be applied to other locations of body such as necks for motorbike riders and knees for beginners of cycling.

Appendix A

Review of Basic Thermodynamics and Fluid Dynamics

A.1 Thermodynamics

First Law of Thermodynamics

The change in specific internal energy (de) equals the sum of the heat added (δq) and work done (δw) on the system [24].

$$de = \delta q + \delta w \qquad \text{(A.1.1)}$$

The value of *de* depends only on the initial and final states of the system. In contrast, δq and δw depend on the process between the initial and final states. This gives rise to inexact differentiation. Thus, the operator δ is used instead of *d*. The processes can be classified as adiabatic, reversible and isentropic processes. This is the first law of thermodynamics. But it cannot tell the direction in which a process takes place.

Second Law of Thermodynamics

The second law states that a process will take place in the direction in which the entropy of the system plus the surroundings always increases or stays the same [24]:

$$ds = \frac{\delta q_{rev}}{T} \geq 0 \qquad \text{(A.1.2)}$$

where s is the entropy of the system, δq_{rev} is the amount of heat reversibly added to the system and T is the temperature.

Internal Energy and Enthalpy

For an equilibrium system of a real gas, the specific internal energy, e (internal energy per unit mass, kJ/kg) is a function of both temperature and volume. The internal energy is due to the molecular motion in the fluid. The specific enthalpy is a function of both temperature and pressure [24]:

$$h = e + pv \qquad \text{(A.1.3)}$$

where h is specific enthalpy (kJ/kg), p is pressure (Pa) and v is specific volume (m^3/kg) (which is equal to the recipical of density). The term pv is called flow energy which equals the energy required to push the fluid into or out of the control volume [26].

If the intermolecular forces are ignored (giving thermally perfect gas), the specific internal energy and enthalpy are functions of temperature only. Besides, the specific heats at constant pressure and volume c_p and c_v are also functions of temperature only:

$$c_p = \frac{dh}{dT} \tag{A.1.4}$$

$$c_v = \frac{de}{dT} \tag{A.1.5}$$

If the specific heats are constant, the system is a calorically perfect gas, where

$$h = c_p T \tag{A.1.6}$$

$$e = c_v T \tag{A.1.7}$$

It is assumed that $h = e = 0$ at $T = 0$.

In most compressible flows, the gas can be considered to be calorically perfect, for example, the atmospheric air at temperature below 1000K [24].

Define $\gamma = c_p / c_v$ as ratio of specific heats. For air at standard condition, $\gamma = 1.4$ and $\gamma = 1.3$ for carbon dioxide.

Other relations for the specific heats hold for a calorically perfect or thermally perfect gas:

$$c_p + c_v = R \tag{A.1.8}$$

$$c_p = \frac{R\gamma}{\gamma - 1} \tag{A.1.9}$$

$$c_v = \frac{R}{\gamma - 1} \tag{A.1.10}$$

For a calorically perfect gas, the change in entropy between two states can be calculated by

$$s_2 - s_1 = c_p \ln\frac{T_2}{T_1} - R \ln\frac{P_2}{P_1} \tag{A.1.11}$$

or $$s_2 - s_1 = c_v \ln\frac{T_2}{T_1} + R\ln\frac{v_2}{v_1} \qquad \text{(A.1.12)}$$

These equations are derived from the definition of entropy and enthalpy.

Isentropic Relations

For isentropic process, the entropy is constant since $\delta q_{rev} = 0$.

$$s_2 - s_1 = c_p \ln\frac{T_2}{T_1} - R\ln\frac{P_2}{P_1} = 0$$

$$\frac{P_2}{P_1} = \left(\frac{T_2}{T_1}\right)^{c_p/R}$$

$$\frac{P_2}{P_1} = \left(\frac{T_2}{T_1}\right)^{\gamma/(\gamma-1)} \qquad \text{(A.1.13)}$$

Similarly,

$$s_2 - s_1 = c_v \ln\frac{T_2}{T_1} + R\ln\frac{v_2}{v_1} = 0$$

$$\frac{v_2}{v_1} = \left(\frac{T_2}{T_1}\right)^{-1/(\gamma-1)}$$

$$\frac{\rho_2}{\rho_1} = \left(\frac{T_2}{T_1}\right)^{1/(\gamma-1)} \qquad \text{(A.1.14)}$$

A boundary layer where dissipative mechanisms of viscosity and thermal conduction are important is formed at the wall of the pipe or fittings. The dissipative mechanisms increase the entropy within the boundary layer. However, the dissipative mechanisms are negligible outside the boundary layer. In addition to no heat addition (adiabatic), the fluid outside the boundary layer is isentropic. Therefore, the isentropic relations can be applied to the calculation of airbag inflation by the compressed CO_2 cylinder.

Adiabatic Expansion of CO_2

The discharge of CO_2 from the cylinder is an endothermic process. Under high pressure, the gas discharges from the cylinder rapidly at sonic speed into a larger volume of lower pressure. The gas has to do work to overcome the intermolecular forces and the atmospheric pressure in order to expand. Since the gas undergoes adiabatic expansion, the only heat source comes from the kinetic energy of the gas molecules themselves. Thus, the internal energy and hence the temperature will drop rapidly.

Moreover, the CO_2 inside the cylinder is initially compressed at high pressure around 70bars and stored at ambient temperature (~20°C). From phase diagram and simple mathematics, it is proved that all the CO_2 inside is liquefied. Since the liquid CO_2 vaporizes rapidly (adiabatically), the only heat absorbed to vaporize comes from the liquid itself and also the cylinder. Therefore, the temperature of the liquid CO_2 drops rapidly before ejected and the cooling process condenses water vapor on the cylinder's surface.

The isentropic relations (A.1.13) and (A.1.14) describe the change of pressure, temperature and specific volume during the adiabatic expansion. It is reminded that the relations are valid for ideal gas. For a real gas, it expands under the Joule-Thompson Expansion. For gases likes neon and helium, they heat up during expansion. But, CO_2 cools down during expansion.

A.2 Fluid Mechanics: Incompressible and Compressible Flow

Bernoulli's Equation

$$P+\frac{1}{2}\rho u^2 = const \qquad \text{(A.2.1)}$$

Bernoulli's equation is applicable for incompressible flows in which density is constant. In the discharge of compressed CO_2, gas velocity is more than 0.3 of speed of sound and the flow is regarded as a compressible flow. The density is no longer constant in compressible flows.

Ideal Gas

In an ideal gas, the intermolecular forces are neglected. In contrast, intermolecular forces are important in real gases. The empirical equation for an ideal gas is

$$P=\rho RT \qquad \text{(A.2.2)}$$

where P is the pressure (N/m^2), ρ is the density (kg/m^2) and R is the specific gas constant (J/(kg • K)) and T is the temperature (K).

Total Pressure and Temperature vs. Static Pressure and Temperature

Recall Bernoulli's equation (A.2.1):

$$P_1 = P_2 + \frac{1}{2}\rho_2 u_2^2$$

For a dynamic system, pressure has two components: static pressure (P_2) and dynamic pressure ($1/2\,\rho_2 u_2^2$). The static pressure is independent of the fluid movement and acts equally in all directions. The dynamic pressure is associated with the fluid's velocity. The sum of these two pressures is the total or stagnation pressure (P_1).

For a dynamic system, static pressure can be measured by tapping perpendicular to the flow. The static pressure can be directly measured by pressure sensors or pressure gauge. The dynamic pressure cannot be measured directly. However, the total pressure can be measured by a Pitot tube which is aligned parallel to the flow and its tip points to the incoming flow [25].

Consider the fluid element at point A with static pressure, static temperature and velocity of P, T and u respectively. If the fluid element is isentropically slowed down to zero velocity, the pressure and temperature change in magnitude. The new pressure P_0 and temperature T_0 are the total pressure and total temperature. The concept can also be applied to two different locations provided that the viscosity effect due to friction is negligible and there is no heat addition.

Appendix B

Derivation of Equations

B.1 Mass Flow Rate Equations

Vena Contracta

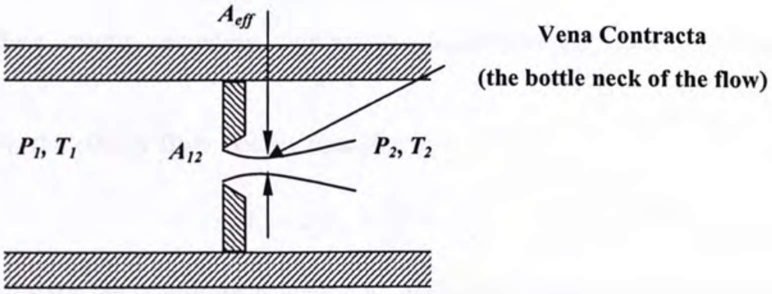

Figure B-1) Flow pattern across an orifice

Imagine a car makes a turn at a corner of road. If the speed of the car is too high, it cannot keep the path along the road. The same phenomenon happens in the fluid flow. When the flow passes through the orifice as shown in Figure B-1, it starts to separate from the wall. It continues to converge until the vena contracta is rearched.

To calculate the mass flow rate at the vena contracta, two assumptions are made. First the flow from upstream to the vena contracta is assumed to be isentropic. As a result, the total pressure, temperature and entropy at the vena contracta equal those at upstream. Second the static pressure at vena contracta is assumed to be equal to the downstream static pressure. Eventually, the total pressure and temperature, and static pressure are known at the vena contracta. [27]

Mass Flow Rate

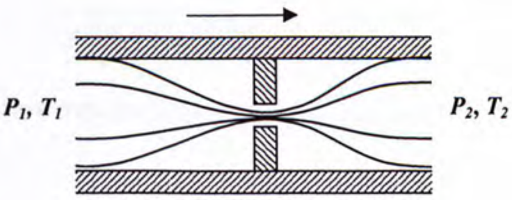

Figure B-2) A flow across an orifice

For incompressible flow, the Bernoulli's equation and conservation of mass can be applied to find the mass flow rate:

$$P_1 = P_2 + \frac{\rho_2}{2} u_2^2 \tag{B.1.3}$$

$$W_{12} = \rho_2 A_{12} u_2 \tag{B.1.4}$$

$$W_{12} = A_{12}\sqrt{2\rho_2 (P_1 - P_2)} \tag{B.1.5}$$

For compressible flow, energy equation, perfect gas equations and isentropic relations are applied:

In an isentropic flow, the steady flow energy equation is

$$c_p T_1 = c_p T_2 + \frac{u_2^2}{2} \tag{B.1.6}$$

Equation (B.1.6) holds for the condition in which no body force and viscous force act on the fluid, and no heat is added to the system (i.e. adiabatic condition).

Rearrange the terms, the velocity of flow is obtained:

$$u_2 = \sqrt{\frac{2\gamma R T_1}{\gamma - 1}\left[1 - \left(\frac{P_2}{P_1}\right)^{(\gamma-1)/\gamma}\right]} \tag{B.1.7}$$

Recall the ideal gas equation $P = \rho R T$ and the isentropic relation between pressure and temperature (A.1.13). By rearranging the density in terms of other parameters, we get

$$\rho_2 = \frac{P_1}{R T_1}\left(\frac{P_2}{P_1}\right)^{1/\gamma} \tag{B.1.8}$$

Substituting Equations (B.1.7) and (B.1.8) into (B.1.4),

$$\begin{aligned} W_{12} &= \rho_2 A_{12} u_2 \\ &= \frac{P_1}{R T_1}\left(\frac{P_2}{P_1}\right)^{1/\gamma} A_{12}\sqrt{\frac{2\gamma R T_1}{\gamma - 1}\left[1 - \left(\frac{P_2}{P_1}\right)^{(\gamma-1)/\gamma}\right]} \end{aligned}$$

Finally, we get the mass flow rate equation for unchoked flow

$$W_{12} = \frac{A_{12}P_1}{\sqrt{T_1}}\left\{\frac{2\gamma}{R(\gamma-1)}\left[\left(\frac{P_2}{P_1}\right)^{2/\gamma} - \left(\frac{P_2}{P_1}\right)^{\gamma+1/\gamma}\right]\right\}^{1/2} \tag{B.1.9}$$

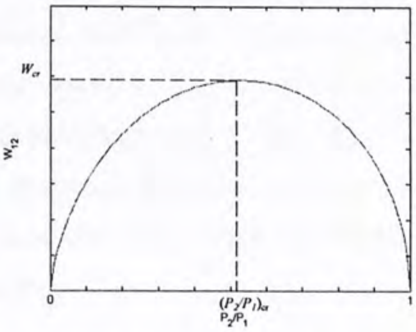

Figure B- 3) A plot of mass flow rate against pressure ratio

As see from Figure B- 3, the compressible mass flow rate equation has a maximum value (maximum mass flow rate) for given values of flow area, total pressure and temperature. Further lowering the downstream pressure (P_2) will not increase the flow rate. The flow is said to be choked. Differentiating the equation with respect to the pressure ratio and setting the derivative to zero, the "critical" pressure ratio which corresponds to the maximum mass flow rate is obtained:

$$\left(\frac{P_2}{P_1}\right)_{cr} = \left(\frac{2}{\gamma+1}\right)^{\gamma/(\gamma-1)} \tag{B.1.10}$$

Substituting the critical pressure ratio into Equation (B.1.7) gives the critical velocity

$$u_{2cr} = \sqrt{\gamma R T_2} \tag{B.1.11}$$

which is the speed of sound at static temperature T_2. This means that the fluid flows at speed of sound under the maximum mass flow rate.

The critical mass flow rate can be obtained by substituting the critical pressure ratio and critical velocity into Equation (B.1.4):

$$W_{cr} = \frac{A_{12}P_1}{\sqrt{T_1}}\left\{\frac{\gamma}{R}\left[\left(\frac{2}{\gamma+1}\right)^{(\gamma+1)/(\gamma-1)}\right]\right\}^{1/2} \tag{B.1.12}$$

Let's summarize the concept of mass flow rate equations: for pressure ratio higher than the critical value, the flow is subsonic and Equation (B.1.9) is used; for pressure ratio lower than and equal to the critical value, the flow is sonic (or choked) and Equation (B.1.12) is used. However, this does not mean that the mass flow rate cannot be further increased for a given flow area. Remember that the mass flow rate is proportional to density, flow area and velocity. Even though the flow area and velocity are fixed, the density can be raised by increasing the total pressure (P_1).

To adopt the convention of the author of [27], two more terms N_{12} and K are introduced. N_{12} is the ratio of the ratios of the current mass flow rates to critical flow rates across the orifice A_{12}. That is

$$N_{12} = \frac{W_{12}}{W_{cr}} = \left[\frac{\left(\frac{P_2}{P_1}\right)^{2/\gamma} - \left(\frac{P_2}{P_1}\right)^{(\gamma+1)/\gamma}}{\frac{\gamma-1}{2}\left(\frac{2}{\gamma+1}\right)^{(\gamma+1)/(\gamma-1)}}\right]^{1/2} \tag{B.1.13}$$

K is the characteristic of the gas and a function of ratio of specific heats and gas constant:

$$K = \left[\frac{\gamma}{R}\left(\frac{2}{\gamma+1}\right)^{(\gamma+1)/(\gamma-1)}\right]^{1/2} \tag{B.1.14}$$

B.2 Relationship between Rate of Changes of Airbag Pressure and Volume

Assuming the gas is ideal, and the pressure and temperature are constant throughout the volume, the mass of the gas in the airbag is given by the perfect gas equation:

$$M_2 = \frac{P_2V_2}{RT_2} \tag{B.2.3}$$

Taking logarithmic differentiation on both sides gives

$$\frac{dm_2}{M_2}=\frac{dp_2}{P_2}+\frac{dv_2}{V_2}-\frac{dt_2}{T_2} \tag{B.2.4}$$

where dm_2, dp_2, dv_2, dt_2 are variables (functions of time) and M_2, P_2, V_2, T_2 are constants.

Assuming that temperature is related to pressure by the polytropic relation $\frac{dt_2}{T_2}=\frac{n-1}{n}\frac{dp_2}{P_2}$, then

$$\frac{dp_2}{nP_2}=-\frac{dv_2}{V_2}+\frac{dm_2}{M_2} \tag{B.2.5}$$

Dividing both sides by *dt*,

$$\frac{M_2}{nP_2}\frac{dP_2}{dt}=-\frac{M_2}{V_2}\frac{dV_2}{dt}+\frac{dM_2}{dt} \tag{B.2.6}$$

where $\frac{dP_2}{dt}$ is the rate of change of airbag pressure, $\frac{dV_2}{dt}$ is the rate of change of airbag volume or the rate of change of gas volume under free expansion, and $\frac{dM_2}{dt}$ is the rate of change of mass of gas inside the airbag. The equation only describes the dynamics of the gas, but not the interaction of the airbag membrane and the gas.

Consider the rate of mass change of gas inside the airbag $\frac{dM_2}{dt}$, it equals the net mass flow rate into the airbag, i.e. the difference between the inlet and outlet mass flow rates:

$$\frac{dM_2}{dt}=W_{12}-W_{23} \tag{B.2.7}$$

Case i) Before the airbag is fully inflated, the airbag pressure is assumed to maintain atmospheric pressure.

$$\frac{dP_2}{dt}=0 \Rightarrow \frac{P_2}{RT_2}\frac{dV_2}{dt}=W_{12}-W_{23} \tag{B.2.8}$$

Case ii) After the airbag is fully inflated, the airbag pressure starts to increase from atmospheric pressure and hence the mass flow rate W_{23} is non-zero.

$$\frac{dV_2}{dt}=0 \Rightarrow \frac{V_2}{nRT_2}\frac{dP_2}{dt}=W_{12}-W_{23} \qquad \text{(B.2.9)}$$

To simply the program, W_{12} is taken as the flow rate at the exit (orifice) of the compressed gas cylinder.

B.3 Pressure Change of Compressed Gas Cylinder

Recall Equation (B.2.6) and set $\frac{dV}{dt}=0$ since the volume of cylinder is fixed.

$$\frac{dP_1}{dt}=\frac{nP_1}{M_1}\frac{dM_1}{dt}$$

$$\frac{dP_1}{dt}=\frac{nRT_1}{V_1}(W_{12}-W_{23})$$

$$\frac{dP_1}{P_1}=-n\sqrt{\frac{T_1}{T_0}}\left[N_{12}-C_{01}\sqrt{\frac{T_1}{T_0}}\frac{A_{01}}{A_{12}}\right]d\left(\frac{KR\sqrt{T_0}A_{12}}{V_1}t\right) \qquad \text{(B.3.2)}$$

For the compressed gas cylinder, take A_{01} be zero (since the cylinder does not have an inlet orifice).

$$\frac{dP_1}{P_1}=-n\sqrt{\frac{T_1}{T_0}}N_{12}d\left(\frac{KR\sqrt{T_0}A_{12}}{V_1}t\right) \qquad \text{(B.3.3)}$$

where T_0 and P_0 are the initial values of temperature and pressure of the cylinder.

Case i) The discharging process is adiabatic. Then $n=\gamma$ and the temperature ratio is related to pressure ratio by isentropic relation, Equation (A.1.13). Therefore,

$$\frac{dP_1}{P_1}=-\gamma\left(\frac{P_1}{P_0}\right)^{(\gamma-1)/2\gamma}N_{12}d\left(\frac{KR\sqrt{T_0}A_{12}}{V_1}t\right) \qquad \text{(B.3.4)}$$

or

$$\frac{d(P_1/P_0)}{(P_1/P_0)^{(3\gamma-1)/2\gamma}}=-\gamma N_{12}d\tau \qquad \text{(B.3.5)}$$

where $\tau = \frac{KR\sqrt{T_0}A_{12}}{V_1}t$

If A_{12} is under sonic flow, N_{12} is 1. Integration gives

$$P_1 = P_0\left(1+\frac{\gamma-1}{2}\tau\right)^{-2\gamma/(\gamma-1)} \tag{B.3.6}$$

Otherwise, N_{12} changes with the pressure ratio (P_1/P_0) and the iteration process should be used.

Case ii) The discharging process is isothermal. Then $n = 1$ and the temperature ratio equals to 1. Therefore,

$$\frac{dP_1}{P_1} = -N_{12}d\left(\frac{KR\sqrt{T_0}A_{12}}{V_1}t\right) = -N_{12}d\tau \tag{B.3.7}$$

If A_{12} is under sonic flow, N_{12} is 1. Integration gives

$$P_1 = P_0e^{-\tau} \tag{B.3.8}$$

Otherwise, N_{12} changes with the pressure ratio (P_1/P_0) and the iteration process should be used.

B.4 Dominating Factors in the Mass Flow Rate Equation

The following is the derivation of partial derivative of mass flow rate equations with respect to orifice area, total pressure and static pressure respectively:

For sonic flow:

$$\frac{\partial W_{12}}{\partial A_{12}} = \frac{P_1}{\sqrt{T_1}}\left\{\frac{\gamma}{R}\left[\left(\frac{2}{\gamma+1}\right)^{(\gamma+1)/(\gamma-1)}\right]\right\}^{1/2}$$

$$\frac{\partial W_{12}}{\partial P_1} = \frac{A_{12}}{\sqrt{T_1}}\left\{\frac{\gamma}{R}\left[\left(\frac{2}{\gamma+1}\right)^{(\gamma+1)/(\gamma-1)}\right]\right\}^{1/2}$$

$$\frac{\partial W_{12}}{\partial P_2} = 0$$

For subsonic flow:

$$\frac{\partial W_{12}}{\partial A_{12}} = \frac{P_1}{\sqrt{T_1}}\left\{\frac{2\gamma}{R(\gamma-1)}\left[\left(\frac{P_2}{P_1}\right)^{2/\gamma} - \left(\frac{P_2}{P_1}\right)^{\gamma+1/\gamma}\right]\right\}^{1/2} = \frac{P_1}{\sqrt{T_1}} f\left(\frac{P_2}{P_1}\right)$$

$$\begin{aligned}\frac{\partial W_{12}}{\partial P_1} &= \frac{A_{12}}{\sqrt{T_1}}\left\{\frac{2\gamma}{R(\gamma-1)}\left[\left(\frac{P_2}{P_1}\right)^{2/\gamma} - \left(\frac{P_2}{P_1}\right)^{\gamma+1/\gamma}\right]\right\}^{1/2} + \frac{A_{12}P_1}{2\sqrt{T_1}}\left\{\frac{2\gamma}{R(\gamma-1)}\left[\left(\frac{P_2}{P_1}\right)^{2/\gamma} - \left(\frac{P_2}{P_1}\right)^{\gamma+1/\gamma}\right]\right\}^{-1/2} \\
&\quad \times \frac{2\gamma}{R(\gamma-1)}\left[-\frac{2}{\gamma}\left(\frac{P_2}{P_1}\right)^{2/\gamma}\frac{1}{P_1} + \frac{\gamma+1}{\gamma}\left(\frac{P_2}{P_1}\right)^{\gamma+1/\gamma}\frac{1}{P_1}\right] \\
&= \frac{A_{12}}{\sqrt{T_1}}\left\{\frac{2\gamma}{R(\gamma-1)}\left[\left(\frac{P_2}{P_1}\right)^{2/\gamma} - \left(\frac{P_2}{P_1}\right)^{\gamma+1/\gamma}\right]\right\}^{1/2} + \frac{A_{12}}{2\sqrt{T_1}}\left(\frac{2\gamma}{R(\gamma-1)}\right)^{1/2}\left[\left(\frac{P_2}{P_1}\right)^{2/\gamma} - \left(\frac{P_2}{P_1}\right)^{\gamma+1/\gamma}\right]^{-1/2} \\
&\quad \times \left[-\frac{2}{\gamma}\left(\frac{P_2}{P_1}\right)^{2/\gamma} + \frac{\gamma+1}{\gamma}\left(\frac{P_2}{P_1}\right)^{\gamma+1/\gamma}\right] \\
&= \frac{A_{12}}{\sqrt{T_1}}\left[f\left(\frac{P_2}{P_1}\right) + g\left(\frac{P_2}{P_1}\right)\right]\end{aligned}$$

$$\frac{\partial W_{12}}{\partial P_2} = \frac{A_{12}P_1}{2\sqrt{T_1}P_2}\left(\frac{2\gamma}{R(\gamma-1)}\right)^{1/2}\left[\left(\frac{P_2}{P_1}\right)^{2/\gamma} - \left(\frac{P_2}{P_1}\right)^{\gamma+1/\gamma}\right]^{-1/2}\left[\frac{2}{\gamma}\left(\frac{P_2}{P_1}\right)^{2/\gamma} - \frac{\gamma+1}{\gamma}\left(\frac{P_2}{P_1}\right)^{\gamma+1/\gamma}\right]$$

$$= -\frac{A_{12}P_1}{\sqrt{T_1}P_2} g\left(\frac{P_2}{P_1}\right)$$

Appendix C

Dimensions of Inflator

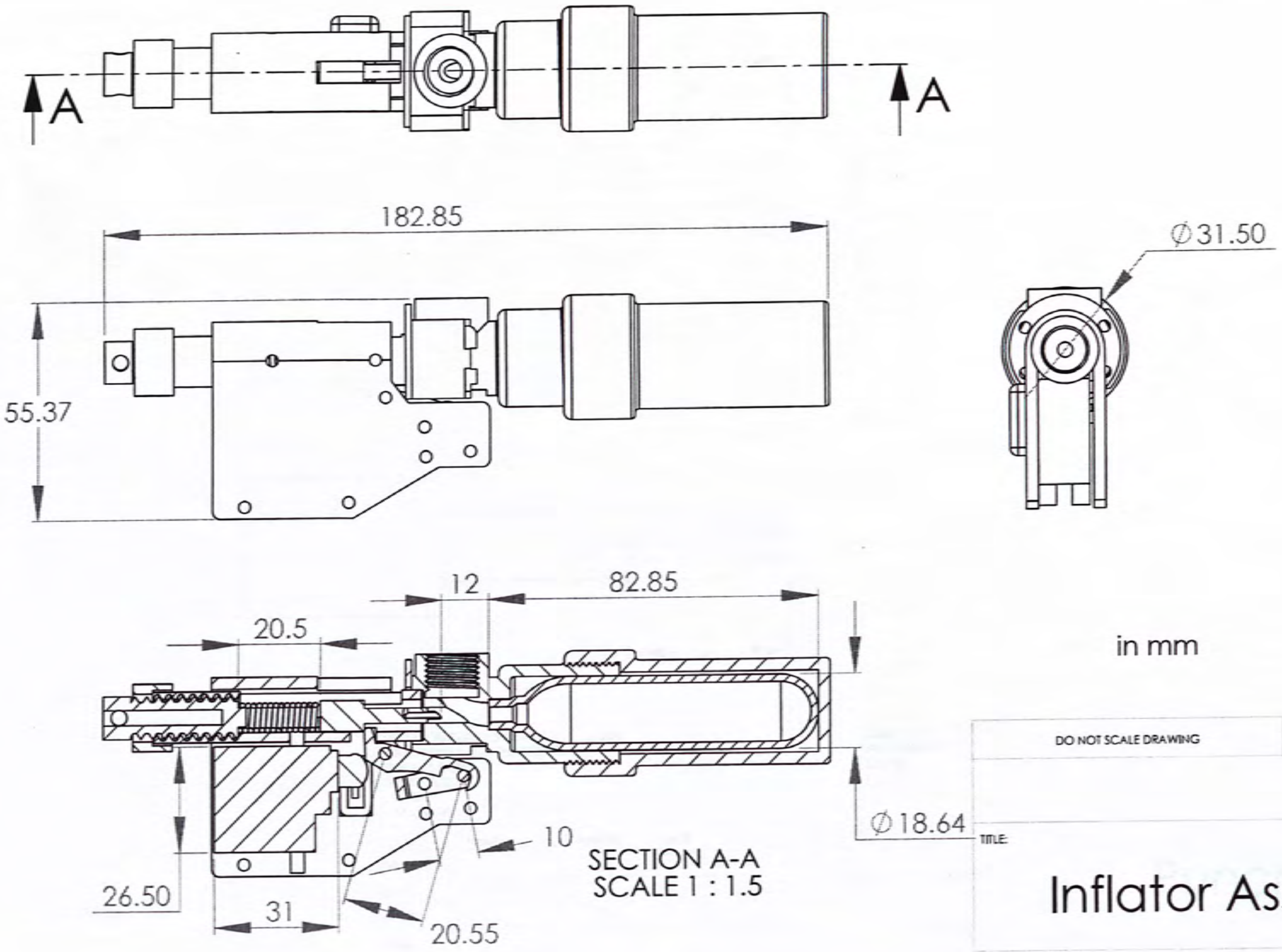

in mm

DO NOT SCALE DRAWING
REVISION

TITLE:

Inflator Assembly

DWG NO.
A4

SCALE:1:2
SHEET 1 OF 1

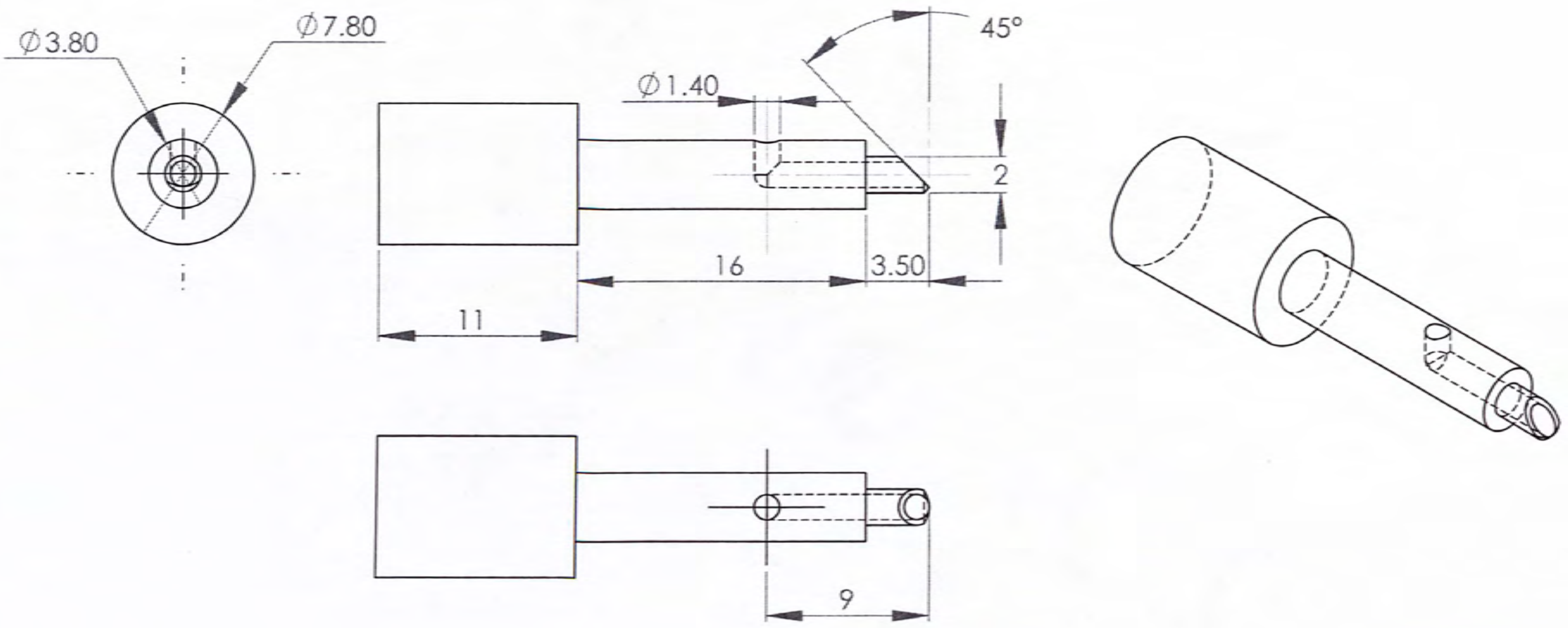

UNLESS OTHERWISE SPECIFIED:
DIMENSIONS ARE IN MILLIMETERS
SURFACE FINISH:
TOLERANCES:
LINEAR:
ANGULAR:

FINISH:

DEBUR AND
BREAK SHARP
EDGES

DO NOT SCALE DRAWING

REVISION

	NAME	SIGNATURE	DATE
DRAWN			
CHK'D			
APPV'D			
MFG			
Q.A			

TITLE:

Punch

MATERIAL:

DWG NO.

A4

WEIGHT:

SCALE:2:1

SHEET 1 OF 1

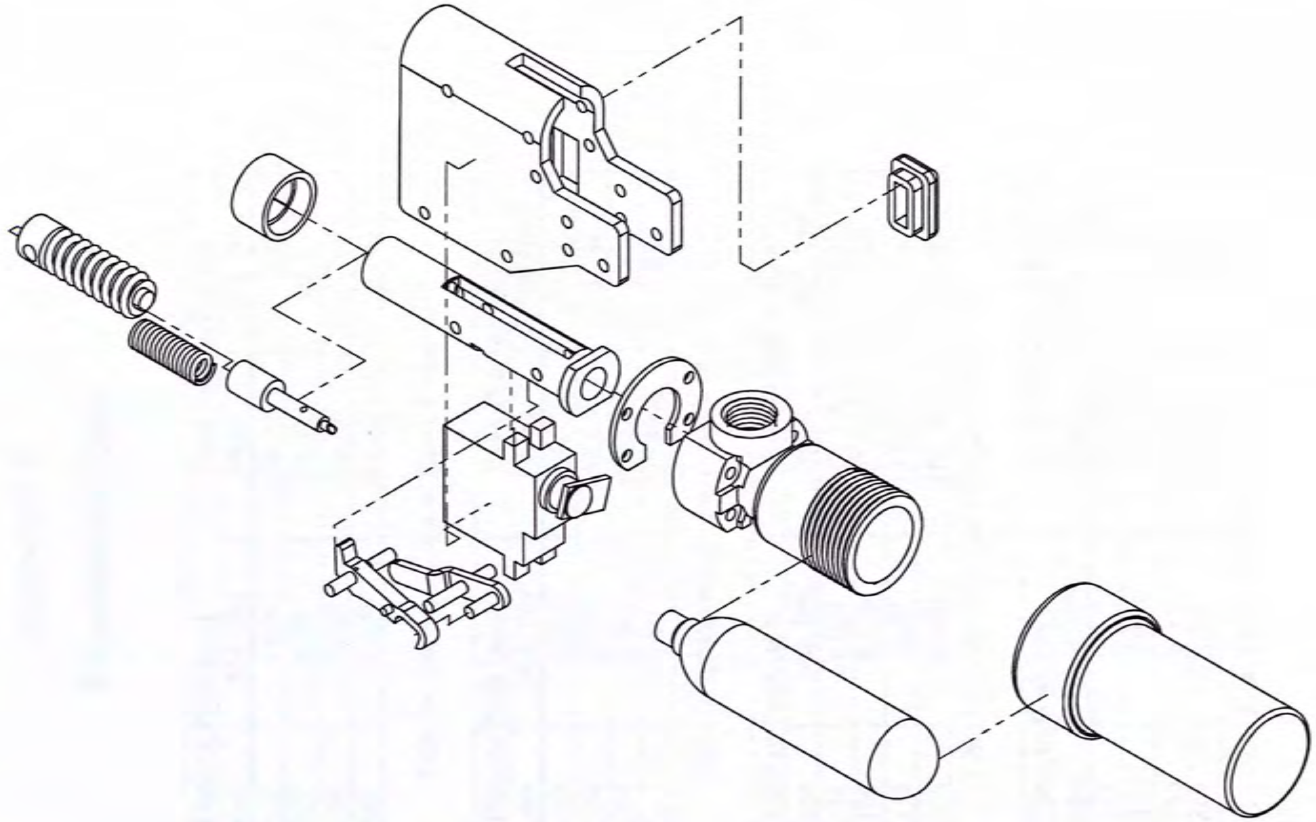

DO NOT SCALE DRAWING

REVISION

TITLE:

Exploded View

DWG NO.

A4

SCALE:1:2

SHEET 1 OF 1

Appendix D

Experimental Data

Time to Peak (sec)		Peak Pressure (kPa)	
Mean	**Std. Div.**	**Mean**	**Std. Div.**
0.333	0.005	156.397	1.822
0.427	0.020	201.323	10.394
0.467	0.026	264.123	5.769
0.487	0.009	306.200	0.198

Table D- 1) Measured data on Figure 4-16 (n =3)

Time to Peak (sec)		Peak Pressure (kPa)	
Mean	**Std. Div.**	**Mean**	**Std. Div.**
0.240	0.034	125.075	0.672
0.324	0.051	152.610	5.388
0.384	0.045	190.395	2.128
0.392	0.017	222.860	0.354

Table D- 2) Measured data on Figure 4-17 (n =3)

Time to Peak (sec)		Peak Pressure (kPa)	
Mean	**Std. Div.**	**Mean**	**Std. Div.**
0.144	0.034	112.210	0.212
0.180	0.028	123.525	2.440
0.212	0.017	143.440	0.339
0.248	0.000	161.000	0.085

Table D- 3) Measured data on Figure 4-18 (n = 3)

Time to Peak (sec)		Peak Pressure (kPa)	
Mean	**Std. Div.**	**Mean**	**Std. Div.**
1.187	0.027	100.800	0.000
0.956	0.028	104.940	0.537
0.788	0.006	111.625	0.318
0.697	0.012	114.896	0.537

Table D- 4) Measured data on Figure 4-26 (n = 3)

Time to Peak (sec)		Peak Pressure (kPa)	
Mean	Std. Div.	Mean	Std. Div.
1.167	0.000	100.800	0.000
0.926	0.020	106.080	0.000
0.832	0.045	114.615	0.247
0.676	0.062	118.468	0.215

Table D- 5) Measured data on Figure 4-27 (n = 3)

Time to Peak (sec)		Peak Pressure (kPa)	
Mean	Std. Div.	Mean	Std. Div.
1.003	0.106	107.580	0.028
0.833	0.024	109.956	0.000
0.788	0.107	113.033	0.052

Table D- 6) Measured data on Figure 4-28 (n = 3)

Pressure (kPa)	Velocity (m/s)	Peak Force (N)	
		Mean	Std. Div.
102.11	1.4	306.757	15.812
	1.98	455.392	22.805
	2.8	742.120	--
102.93	1.4	294.108	9.488
	1.98	404.793	6.325
	2.8	708.387	--
104.15	1.4	252.995	6.325
	1.98	421.659	13.166
	2.8	592.959	--

Table D- 7) Measured data on Figure 5-6 (n = 3)

Bibliography

[1] Drs. Heidi Sveistrup, Donna Lockett, "Hip Protectors and Community-Living Seniors: A Review of the Literature"

[2] Greenspan S.L., Myers E. R., Maitland L.A., Resnick, N.M., and Hayes. W.C., "Fall Severity and Bone Mineral Density as Risk Factors for Hip Fracture in Ambulatory Elderly", *JAMA*, Vol. 271, 1994, pp. 128-133

[3] Chan J, Lam PS, Sze PC, Leung KS., "A study of the epidemiology of falls in Hong Kong. International Society for Fracture Repair", Symposium on Preventing Falls and Fractures in Older Persons, Yokohama, Japan, Jun 29-1 Jul, 2004.

[4] Drs. Heidi Sveistrup, Donna Lockett, "Hip Protectors and Community-Living Seniors: A Review of the Literature", 2003

[5] Peter D. O'Hallorana,_, Liam J. Murrayb, Gordon W. Cranb, Louise Dunlopc, George Kernohand, TimothyR.O. Beringer, "The effect of type of hip protector and resident characteristics on adherence to use of hip protectors in nursing and residential homes—an exploratory study", *International Journal of Nursing Studies*, Vol. 42, 2005, pp. 387–397

[6] Jeffrey B. Burl, James Centola, Alice Bonner and Colleen Burque, "Hip Protector Compliance: A 13-Month Study on Factors and Cost in a Long-Term Care Facility", *JAMDA*, 2003, pp. 245-250

[7] Laurintzen, J.B., "Hip fractures: epidemiology, risk factors, falls, energy absorption, hip protectors and prevention". *Danish Medical Bulletin*, Vol. 44, 1997, pp. 155-168

[8] Daniel K. Chan, Gary Hillier, Michelle Coore, Rosemary Cooke, Rebecca Monk, Janette Mills, Wai T. Hung, "Effectiveness and acceptability of a newly designed hip protector: a pilot study", *Archives of Gerontology and Geriatrics*, Vol. 30, 2000, pp 25-34

[9] Jantti PO, Aho HJ, Maki-Jokela PL, Heikinheimo RJ, "Hip protectors and hip fractures", *Age Ageing*, Vol. 27, 1998, pp. 758-759

[10] Lauritzen J. B., Petersen M. M., and Lund B., "Effect of External Hip Protectors on Hip Fractures", *Loncet*, Vol. 341, 1995, pp. 11-13

[11] P. Kannus, J. Parkkari and J. Poutala, "Comparison of Force Attenuation Properties of Four Different Hip Protectors under Simulated Falling Conditions in the Elderly: An In Vitro Biomechanical Study", *Elsevier*, Bone Vol. 25, No. 2, August 1999, pp. 229-235

[12] Hubacher, M., Huguenin, R.D., "The acceptance of hip protector by senior citizens aged over 70 living at home", *English abstract of German technical report 2000*

[13] Guangyi Shi, C.S. Chan, Yilun Luo, Guanglie Zhang, Wen J. Li, Philip H. W. Leong and Kwok-Sui Leung, "Development of a Human Airbag System for Falling Protection Using MEMS Motion Sensing Technology", *IROS*, 2006

[14] http://www.madehow.com/Volume-1/Air-Bag.html

[15] http://auto.howstuffworks.com

[16] Alan M. Nahum and John W. Melvin, *Accidental Injury – Biomechanics and Prevention*, Springer, Second Edition, Chapter 9

[17] http://www.chemistry.wustl.edu/~edudev/LabTutorials/Airbags/airbags.html

[18] http://www.jobwerx.com/news/ge_launches_exl_resin-newsid=946738.html

[19] http://www.hit-air.com/english/manual/kouzou/kisitu/index.html

[20] "Solenoid Design & Operation", Bicron Electronics Company

[21] www.anpico.com

[22] Qian Weichang, *穿甲力學*, [北京]: 國防工業出版社, 1984, Chapter 1

[23] A.R. Evans and G.D. Sanson, "*The Effect Tooth Shape on the Breakdown of Insects*", *J. Zool.*, Lond., Vol. 246, 1998, pp. 391-400

[24] Anderson, *Modern Compressible Flow with Historical Perspective*, McGraw-Hill Series in Mechanical Engineering, Chapter 1, 2, 3

[25] David Heeley, "Understanding Pressure and Pressure Measurement", Freescale Semiconductor Application Note

[26] Yunus A. Çengel, Robert H. Turner, *Fundamentals of thermal-fluid sciences*, Boston : McGraw-Hill, c2001, Chapter 3 and 4

[27] Blaine W. Andersen, *The Analysis and Design of Pneumatic Systems*, Huntington, N.Y.: R.E. Krieger Pub. Co., 1976, Chapter 4, pp. 147-154

[28] http://en.wikipedia.org/wiki/Supercritical_fluid

[29] http://www.smchk.com.hk/

[30] Aya J. van den Kroonenberg, Wilson C. Hayes and Thomas A. McMahon, "Hip Impact Velocities and Body Configuration for Voluntary Falls from Standing Height", *J Biomech*, 1995, in revision

[31] S. N. Robinovitch, W.C. Hayes, "Predicting the Impact Response of a Nonlinear Single-Degree-of-Freedom Shock-Absorbing System from the Measured Step Response", *Journal of Biomechanical Engineering*, Vol. 119, No. 3, 1997

[32] S.N. Robinovitch, W.C. Hayes, T.A. McMahon, "Prediction of Femoral Impact Forces in Falls on the Hip", *Journal of Biomechanical Engineering*, Vol. 117, pp. 309-318

[33] Siegfried Derler, A.B. Spierings, K.-U. Schmitt, "Anatomical Hip Model for the Mechanical testing of hip protectors", *Medical Engineering & Physics*, Vol. 27, 2005, pp. 475-485

[34] S.N. Robinovitch, W.C. Hayes, "Energy-Shunting Hip Padding System Attenuates Femoral Impact Force in a Simulated Fall", *Journal of Biomechanical Engineering*, Vol. 117, November 1995, pp. 409-413

[35] A.J. van den Kroonenberg, W.C. Hayes, "Dynamic Models for Sideways Falls from Standing Height", *Journal of Biomechanical Engineering*, Vol. 117, 1995, pp.309-318

[36] Balakumar Balachandran, Edward B. Magrab, "*Vibrations*", Thomson 2004, Chapter 4

[37] Vladimir M. Zatsiorsky, *Kinetics of Human Motion*, p.611

[38] Honglu Zhang, Deren Ma and Srini V. Raman, "CAE-Based Side Curtain Airbag Design", *SAE*, 2004

[39] A.J. Buijk and C.J.L. Florie, "Inflation of Folded Driver and Passenger Airbags", The MacNeal-Schwendleer Company B.V

[40] Doris Rieger, “Capability of Simplified Folded Airbag Models in Gasflow Simulations”